

GLORY UNDULATIONS  
IN THE TOTAL CROSS SECTION  
FOR SCATTERING OF  
HEAVY RARE GAS ATOMS

J. W. BREDEWOUT

Diss. Leiden

1973 nr 81

GLORY UNDULATIONS  
IN THE TOTAL CROSS SECTION  
FOR SCATTERING OF  
HEAVY RARE GAS ATOMS

PROEFSCHRIFT

TER VERKRIJGING VAN DE GRAAD VAN DOCTOR IN  
DE WISKUNDE EN NATUURWETENSCHAPPEN AAN DE  
RIJKSUNIVERSITEIT TE LEIDEN, OP GEZAG VAN DE  
RECTOR MAGNIFICUS DR. A. E. COHEN, HOOG-  
LERAAR IN DE FACULTEIT DER LETTEREN, VOLGENS  
BESLUIT VAN HET COLLEGE VAN DEKANEN TE  
VERDEDIGEN OP WOENSDAG 12 SEPTEMBER 1973 TE  
KLOKKE 15.15 UUR.

DOOR

JAN WILLEM BREDEWOUT  
GEBOREN TE WINTERSWIJK IN 1938

1973

DRUKKERIJ J. H. PASMANS. 'S-GRAVENHAGE



Promotoren: Prof. Dr. J.J.M. Beenakker  
Dr. C.J.N. van den Meijdenberg



*Aan mijn moeder*

*Aan Ank*

*Aan Jan Willem en Jochem*

Het in dit proefschrift beschreven onderzoek maakt deel uit van het programma van de werkgemeenschap voor Molecuulfysica van de Stichting voor Fundamenteel Onderzoek der Materie (F.O.M.) en werd financieel gesteund door de Nederlandse Organisatie voor Zuiver Wetenschappelijk Onderzoek (Z.W.O.).

## CONTENTS

CHAPTER I	INTRODUCTION	7
	1. The Molecular Beam Method	7
	2. Theoretical Formalism	11
	3. Experimental Limitations	18
CHAPTER II	DESCRIPTION OF APPARATUS	20
	1. General	20
	2. Primary Beam Source	21
	a. Principle	21
	b. Design	21
	c. Beam Formation	22
	d. Beam Intensities	25
	e. Velocity Distribution	30
	f. Seeded Beams	32
	3. Velocity Selector	34
	a. Design	34
	b. Alignment	36
	c. The Transmission Function	37
	d. Calibration	38
	4. Shutter	41
	5. Chopper	41
	6. Pumping Provisions	44
	a. For the Source Chamber	44
	b. For the Main Chamber	44
	7. Scattering Gas Source	46
	a. General	46
	b. Gas Temperature	47
	c. Pressure Measurement	47
	d. Slit Source	49
	e. Multi Channel Source	49
	8. Detector	53
	a. Construction of the Ionizer	53
	b. Performance of the Ionizer	55
	c. Mass Separation and Amplification	56
	9. Measuring Procedure	57

CHAPTER III	DATA REDUCTION	58
	1. Introduction	58
	2. Velocity Spread Correction	60
	a. The Velocity Distribution $P(g)$	60
	b. The Berkling Factor	63
	c. Damping and Position of the Glories	64
	3. Angular Resolution Correction	66
	a. The Angular Resolution Function	67
	a.1 Circular Collimator	68
	a.2 Rectangular Collimator	68
	a.3 Scattering Length	69
	b. Small Angle Differential Cross Section	71
	c. Shift of the Glory Extrema	73
	4. Analysis of Total Cross Section Data	77
	a. The Absolute Values	77
	b. The Velocity Dependence of $Q_{LL}$	77
	c. The Interpretation of Glory Undulations	78
CHAPTER IV	RESULTS AND DISCUSSION	80
	1. Introduction	80
	2. Results	83
	a. Ar-Ar	85
	b. Kr-Kr	87
	c. Ar-Kr and Kr-Ar	91
	d. Ar-Xe	94
	e. Kr-Xe	96
	3. Conclusions	97
APPENDIX	Table A, B The Angular Resolution Function $W(\rho)$	99
	Table C, D Potentials for the Rare Gases	100
	Table E-K Measured Total Cross Sections	103
	Table L-O Calculated Total Cross Sections	115
REFERENCES		121
SAMENVATTING		125
CURRICULUM VITAE		127

## CHAPTER I

## INTRODUCTION

## 1. THE MOLECULAR BEAM METHOD

In describing the macroscopic properties of the rare gases, the pair-potential of the atoms plays an important role. If this pair-potential is known a number of properties of the dilute gas can be accurately calculated, whereas for some properties of the solid and the liquid good estimations are possible. Ab initio calculations of the pair-potential are very complicated and have to-date only been performed for the simplest case of the He-He interaction. Therefore detailed information on the potential should in general come from experimental data. This inverse procedure of calculating the potential directly from measured rare gas properties, however, is near to impossible.

For this reason potential models are introduced with some parameters, which can be adjusted to obtain the best fit to the experimental data. As an example we mention the frequently used Lennard-Jones (12,6) potential

$$V(r) = \epsilon[(r_m/r)^{12} - 2(r_m/r)^6]$$

in which  $r$  is the interatomic distance and  $r_m$  the distance for which the potential attains its minimum value  $-\epsilon$  (see Fig. 1.1). Assuming such a simple potential it may be possible to fit one set of data (for instance the viscosity) by choosing suitable values for  $\epsilon$  and  $r_m$ . But if one determines  $\epsilon$  and  $r_m$  using data of another property (for instance the second virial coefficient), one finds different values for  $\epsilon$  and  $r_m$ . The simple potential model then has to be refined. As better computer facilities become available, potentials with a larger number of adjustable parameters can be handled and fitted to a variety of bulk properties. Different authors, however, still report different potentials; see for example the work of Munn and Smith [MUN 65], Dymond and Alder [DYM 69], Barker and Pompe [BAR 68], Hanley and Klein [HAN 72b] and the review article of



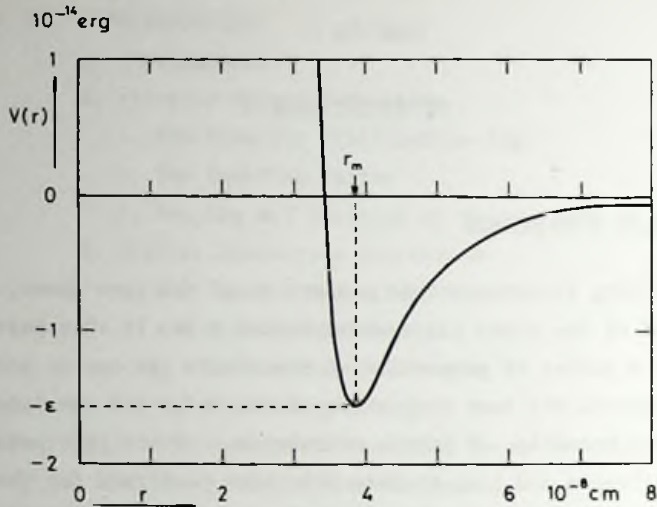


Fig. 1.1 The Lennard-Jones (12,6) pair potential  $V(r)$  for argon as a function of the interatomic separation  $r$ .

Certain and Bruch [CER 71]. Therefore additional information from other experimental fields is not only desired but also necessary for a precise determination of an interaction potential.

A direct method of investigating the intermolecular potential is provided by scattering experiments with molecular beams, where the binary collision of two molecules is studied directly. The averaging over a range of molecular velocities, necessary in the evaluation of bulk properties, can be avoided in a molecular beam experiment, where collisions with well defined initial velocities are studied. The observables of this method are the differential and the total scattering cross section.

An idealized scattering experiment is performed as follows (see Fig. 1.2). In a vacuum chamber a beam of particles moving with uniform velocity  $u$  enters through a collimator of cross section  $A$  into a region where a scattering gas is present. The scatterers are assumed to be at rest. Let the intensity of the incoming beam be  $I_0$  (particles  $s^{-1} cm^{-2}$ ). Some of the beam particles will collide with a scatterer and be deflected, the others will continue their way and constitute the attenuated beam with intensity  $I$ . Let us consider an infinitesimal element of volume  $dV = Adl$  and let  $\dot{N}(\Omega)$  be the number of beam particles that per

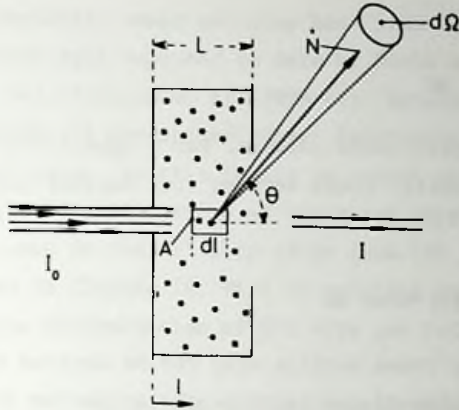


Fig. 1.2 The attenuation of a molecular beam due to collisions with scattering gas molecules.

unit of time is scattered from  $dV$  into the solid angle  $d\Omega$  in the laboratory system.  $\Omega(\theta, \phi)$  is the direction of  $d\Omega$ , with  $\theta$  being the polar angle with respect to the beam direction and  $\phi$  the azimuth angle.  $\dot{N}(\Omega)$  will be proportional to the density  $n(l)$  of the scattering gas, the volume  $dV$ , the solid angle  $d\Omega$  and the local beam intensity  $I(l)$  and is a function of the direction  $\Omega(\theta, \phi)$ . Thus

$$\dot{N}(\Omega) = A n(l) I(l) dl \sigma(\Omega) d\Omega . \quad 1.1$$

The introduced proportionality factor  $\sigma(\Omega)$  is called the *differential cross section* in the laboratory system.

The attenuation  $dI$  of the beam due to the scattering from  $dV$  will be

$$dI = - \int (\dot{N}/A) d\Omega = - n(l) I(l) dl \int \sigma(\Omega) d\Omega . \quad 1.2$$

Integration over the total length  $L$  of the scattering region yields for the observed attenuated beam intensity

$$\begin{aligned} I &= I_0 \exp \left\{ - \int_0^L n(l) dl \cdot \int \sigma(\Omega) d\Omega \right\} \\ &= I_0 \exp \left\{ - Q \int_0^L n(l) dl \right\} , \end{aligned} \quad 1.3$$

The quantity

$$Q = \int \sigma(\Omega) \, d\Omega \quad 1.4$$

is called the *total cross section*. For a spherically symmetric potential  $V(r)$  the differential cross section  $\sigma(\Omega)$  depends only upon  $\theta$  and Eq. 1.4 reduces to

$$Q = 2\pi \int_0^\pi \sigma(\theta) \sin\theta \, d\theta \quad 1.5$$

The differential cross section  $\sigma(\theta)$  can be derived from a measurement of  $I(\theta)$ , the intensity of scattered particles in the direction  $\theta$ . According to Eq. 1.3 the total cross section  $Q$  can be determined from the attenuation of the beam. Both  $\sigma(\theta)$  and  $Q$  and especially their energy dependence provide a large amount of information about the interaction potential of the two colliding particles.

During the last ten years the molecular beam method has yielded excellent results for systems in which the beam particles are alkali atoms and the scatterers inert gas atoms or mercury. The choice of alkali atoms is obvious from the fact that these atoms can be detected with an efficiency one by means of a surface ionisation detector. Furthermore no pumping problems arise, because the alkalis are easily condensable. For these systems, however, no measurements of transport properties are available to check the potentials derived from the scattering data. Therefore scattering experiments with inert gas atoms are of specific interest in view of the possibility of such a comparison. The experimental conditions, however, are much less favourable than for the alkalis. The detection should be performed by ionizing the atoms by means of electron bombardment, which yields a detection efficiency in the order of  $10^{-3}$ . Also the pumping problems increase, i.e. a higher background pressure must be accepted with a much lower signal to noise ratio as a result.

By improving the experimental techniques the aforementioned difficulties have largely been overcome during the last few years, so that scattering experiments with rare gas atoms are now feasible. Quite a few

measurements of differential cross sections have been reported meanwhile\*. The total cross section data reported to date by Rothe et al. [ROT 65], Landorf et al. [LAN 66], Winicur et al. [WIN 69], Baratz et al. [BAR 70a] and Lempert et al. [LEM 71] are either rather inaccurate or cover a somewhat limited velocity range. In this thesis we report measurements of the total cross section for scattering of argon and krypton beams by argon, krypton and xenon in the velocity range from 550 to 4300 ms<sup>-1</sup>. Our results, reported in Chapter IV, fill an existing gap and should lead to a more precise determination of the rare gas interaction potentials.

The way in which we tackled the various experimental problems is described in Chapter II.

## 2. THEORETICAL FORMALISM

In order to introduce a number of equations that will be used afterwards, a very brief summary of the theory is given. For a more detailed description we refer for example to the review articles by Pauly and Toennies [PAU 65] and by Bernstein [BER 66] and the literature quoted by these authors.

The collision problem of two particles with masses  $m_1$  and  $m_2$  and with a spherically symmetric interaction potential  $V(r)$  is simplified by the transformation to a system of coordinates in which the center of mass is at rest (CM-system). Then the problem reduces to that of the scattering of a particle with reduced mass  $\mu = m_1 m_2 / (m_1 + m_2)$  moving with the relative velocity  $g$  in the fixed potential field  $V(r)$ . In the classical treatment the deflection angle  $\theta$  in the CM-system as a function of the impact parameter  $b$  becomes

$$\theta(b) = \pi - 2b \int_{r_0}^{\infty} \frac{dr}{r^2 [1 - 2V(r)/\{\mu g^2\} - b^2/r^2]^{\frac{1}{2}}} \quad 1.6$$

\* All the references up to May 1973 we know concerning the differential cross section of the heavy rare gases are the following: PEN 67, WIL 69, PAR 70a, PAR 70b, PAR 71, CAV 70, SEA 71, SIS 70, SIS 71, CAV 71a, ANL 71, KAL 72, PAR 72, SCH 71a, FAR 73.



where  $r_0$  is the distance of closest approach. For a realistic potential the scattered intensity in the direction  $\theta$  may contain contributions from different impact parameters  $b_j$ . This is illustrated in Fig. 1.3c. The differential cross section  $\sigma(\theta)$  is then given by

$$\sigma(\theta) = \sum_j \frac{b_j}{\sin\theta} \left| \frac{db}{d\theta} \right|_{b_j}, \quad 1.7$$

the total cross section  $Q$  by

$$Q = 2\pi \int_0^\pi \sigma(\theta) \sin\theta \, d\theta \quad 1.7a$$

The classical total cross section is infinite due to the infinite range of the potential  $V(r)$ .

In the quantum mechanical description of the elastic scattering problem one starts from the time independent Schrödinger equation which may be written as

$$(\Delta + k^2)\psi(\vec{r}) = (2\mu/\hbar^2) V(r)\psi(\vec{r}) \quad 1.8$$

where  $k = \mu g/\hbar$  is the wave number of the incoming particles. The solution of Eq. 1.8 has the asymptotic form

$$\psi(\vec{r}) = \exp\{i k z\} + f(\theta)r^{-1} \exp\{i \vec{k} \cdot \vec{r}\} \quad 1.9$$

in which the first term represents the incident plane wave in the  $z$ -direction and the second term the outgoing spherical wave. The quantity  $f(\theta)$  is called the scattering amplitude. The differential cross section now becomes

$$\sigma(\theta) = |f(\theta)|^2. \quad 1.10$$

In solving Eq. 1.8 the incident wave is expanded in a sum of partial waves, each with orbital angular momentum  $\ell$ . The result for  $f(\theta)$  obtained by this *partial wave method* is

$$f(\theta) = k^{-1} \sum_{\ell=0}^{\infty} (2\ell + 1) \exp\{i \eta_\ell\} \sin \eta_\ell P_\ell(\cos\theta). \quad 1.11$$

Each partial wave has a phase shift  $\eta_\ell$  caused by the potential,  $P_\ell(\cos\theta)$

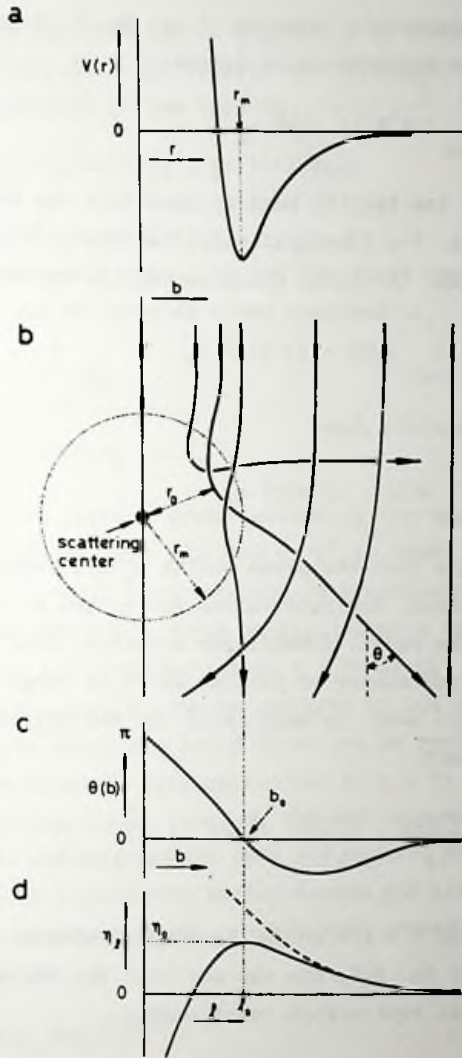


Fig. 1.3 Scattering by a spherically symmetric potential  $V(r)$ .

- The interaction potential.
- Trajectories of monoenergetic particles in the fixed potential field  $V(r)$  for various impact parameters  $b$ .
- The corresponding deflection function  $\theta(b)$ .
- The phase shift  $\eta_l$  as a function of the angular momentum quantum number  $l$ . The solid curve is for a realistic potential with a repulsive and an attractive branch, the dashed curve for a merely attractive potential.

are the Legendre polynomials. From Eq. 1.7a, Eq. 1.10 and the orthogonality of the Legendre polynomials it follows

$$Q = (4\pi/k^2) \sum_{\ell=0}^{\infty} (2\ell + 1) \sin^2 \eta_{\ell} . \quad 1.12$$

In the preceding it has tacitly been assumed that the two colliding particles are different. For identical particles the wave function of Eq. 1.9 should be symmetrized. The total cross section is for the symmetric case:

$$Q = (4\pi/k^2) \sum_{\ell \text{ even}} 2(2\ell + 1) \sin^2 \eta_{\ell} \quad 1.12a$$

and for the antisymmetric case:

$$Q = (4\pi/k^2) \sum_{\ell \text{ odd}} 2(2\ell + 1) \sin^2 \eta_{\ell} \quad 1.12b$$

Eq. 1.12 reveals that the phase shifts  $\eta_{\ell}$  are required to calculate the total cross section. Accurate values for  $\eta_{\ell}$  can be obtained by numerical solution of the radial Schrödinger equation. This method becomes impracticable when the number of partial waves is large. Therefore approximate methods are used. In many cases the WKB approximation is valid, which gives the result

$$\eta_{\ell} = k \left[ \int_{r_0}^{\infty} \left\{ 1 - \frac{2V(r)}{\mu g^2} - \frac{(\ell + \frac{1}{2})^2}{k^2 r^2} \right\}^{\frac{1}{2}} dr - \int_{(\ell + \frac{1}{2})/k}^{\infty} \left\{ 1 - \frac{(\ell + \frac{1}{2})^2}{k^2 r^2} \right\}^{\frac{1}{2}} dr \right] . \quad 1.13$$

By using the relation  $\ell + \frac{1}{2} = kb$  and by comparison with the classical deflection function of Eq. 1.6, one can see that the WKB phase shifts satisfy the semi-classical equivalence relationship

$$\frac{d \eta(b)}{db} = \frac{1}{2} \theta(b) k. \quad 1.14$$

From eq. 1.14 it follows that for a realistic potential the phase shift curve (full curve of Fig. 1.3d) will show a maximum at the value  $\ell_0 = kb_0 - \frac{1}{2}$ , which is determined by the condition  $\theta(b_0) = 0$ . For a merely attractive potential the phase shift is a monotonous decreasing function of  $\ell$  (dashed curve in Fig. 1.3d). For large values of  $\ell$  and hence

small values of  $\eta$  Eq. 1.13 may be simplified by assuming a straight line trajectory (Jeffreys-Born approximation). This approximation yields for an attractive potential of the type  $V(r) = -C_s/r^s$ :

$$\eta_{\ell}^{JB} = (\mu C_s / \hbar^2) k^{(s-2)} (\ell + \frac{1}{2})^{(1-s)} f(s) \quad 1.15$$

where  $f(s) = \frac{1}{4} (\pi)^{\frac{1}{2}} (s-1) / \Gamma(\frac{1}{2}s)$ .

Let us now return to Eq. 1.12 for the total cross section. This may be written as a sum of "partial cross sections"  $q_{\ell}$ :

$$Q = (8 \pi / k^2) \sum_{\ell=0}^{\infty} q_{\ell} \quad 1.16$$

$$\text{with } q_{\ell} = (\ell + \frac{1}{2}) \sin^2 \eta_{\ell} . \quad 1.17$$

An example of these partial cross sections  $q_{\ell}$  versus  $\ell + \frac{1}{2}$  representative for a potential of the type  $V(r) = -C_s/r^s$  is shown in Fig. 1.4 [taken from BER 63a]. The total cross section is graphically represented now by the area under the solid curve multiplied by a factor  $(8 \pi / k^2)$ . In the region of the low  $\ell$ -values (about  $\ell < 70$  in the example), where  $q_{\ell}$  oscillates rapidly,  $\sin^2 \eta_{\ell}$  can be replaced by its average value  $\frac{1}{2}$ . Consequently the area under the solid curve can be replaced by the area under the dashed straight line determined by  $q = (\ell + \frac{1}{2}) \frac{1}{2}$ . In this way and by using for the larger  $\ell$ -values the Jeffreys-Born approximation for the phase shifts Massey and Mohr [MAS 34] derived an expression for  $Q$  in closed form. By a different method Landau and Lifschitz [LAN 59] obtained a more accurate result, as has been proved by Bernstein [BER 63a]. They found

$$Q_{LL} = p(s) [C_s / \hbar g]^2 / (s-1) \quad 1.18$$

where the numerical factor  $p(s)$  becomes 8.083 for  $s = 6$  (van der Waals attraction), to be compared with the value 7.547 for  $p(s)$  in the expression of Massey and Mohr.

When we construct a more realistic potential by adding a repulsive term to the attractive part  $-C_s/r^s$ , the  $q_{\ell}$ 's behave quite different. Because the phase shift attains a maximum value  $\eta_0$  for  $\ell = \ell_0$  there is a region around  $\ell_0$  where  $\sin^2 \eta_{\ell}$  cannot be replaced by its average value  $\frac{1}{2}$ .



Therefore the total cross section will differ from the value given by Eq. 1.18. Depending on the value of  $\eta_0$  the difference can be either positive or negative. This behaviour is illustrated in Fig. 1.5, which shows the  $q_\ell$  we calculated for the PSL-potential for Ar-Ar (see Chapter IV) at a relative velocity of  $1520 \text{ ms}^{-1}$ . Thus the total cross section  $Q$  for this example is smaller than  $Q_{LL}$ . Let us now generally write

$$Q = Q_{LL} + Q_{GL} \quad 1.19$$

The magnitude of the so-called glory contribution  $Q_{GL}$  can be calculated in the semiclassical approximation by assuming a parabolic shape for the phase shift curve near its maximum. Düren and Pauly [DUR 63] give the following expression

$$\begin{aligned} Q_{GL} &= 4\pi b_0 \{ 2\pi/(-\theta_0'k) \}^{\frac{1}{2}} \cos(2\eta_0 + 3\pi/4) \\ &= A_{GL} \cos(2\eta_0 + 3\pi/4) \end{aligned} \quad 1.20$$

where  $\theta_0'$  is the derivative of the deflection function at  $b = b_0$  and  $r_m$  the position of the potential minimum. When the velocity  $g$  is varied over a wide enough range,  $2\eta_0 + 3\pi/4$  runs over several multiples of  $\pi$ , giving rise to undulations in  $Q$  (see Fig. 1.6). The amplitude  $A_{GL}$  is a slowly varying function of  $g$ . The condition for an extremum in  $Q_{GL}$  is therefore

$$(N - 3/8)\pi = \eta_0 \quad 1.21$$

with  $N = 1, 2, 3 \dots$  for the maxima and  $N = 1.5, 2.5 \dots$  for the minima. These undulations in the total cross section are called glory undulations, because of the analogy with the optical phenomenon of the same name [KON 70, MAS 71, KON 72].

To get a physical understanding of the glory undulations we return to the classical deflection function depicted in Fig. 1.3. Let us for example consider the situation at very small angles, where the scattering results from two contributions: a small one from impact parameters in the neighbourhood of  $b_0$  and a large one from very large impact parameters. In

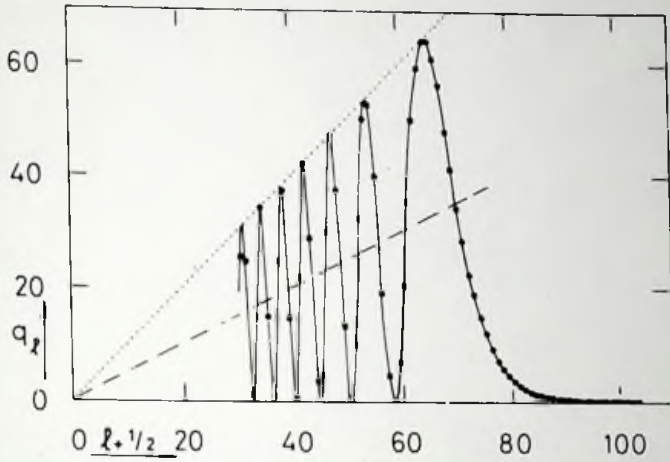


Fig. 1.4 Partial cross sections  $q_l$  for an attractive potential  $V(r) = -C_s/r^5$  versus  $l + \frac{1}{2}$  (solid curve). The dotted line represents  $q_l = (l + \frac{1}{2})$ , the dashed line  $q_l = (l + \frac{1}{2})^2$ .

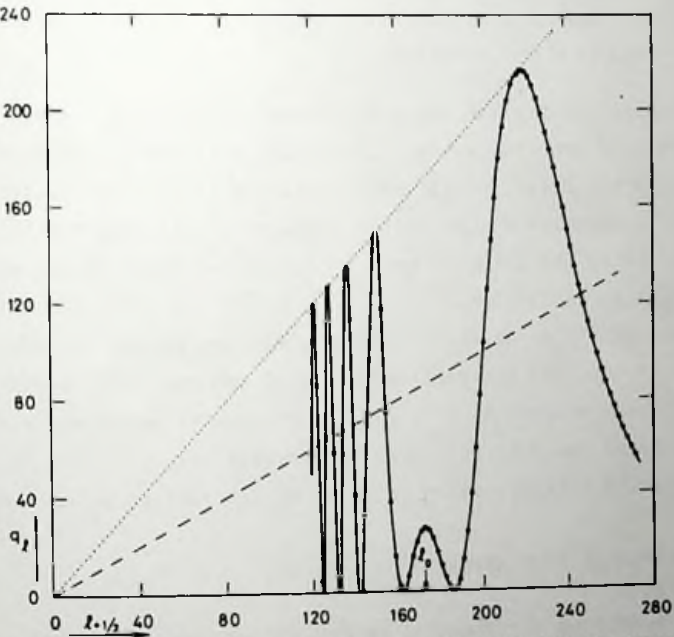


Fig. 1.5 Partial cross sections  $q_l$  for the PSL-potential defined in the Appendix (solid curve).

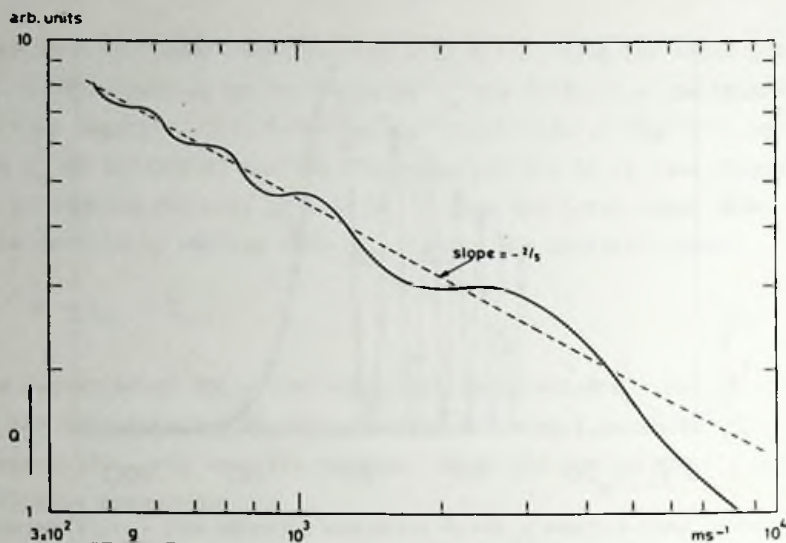


Fig. 1.6 Glory undulations in the total cross section  $Q$  as a function of the relative velocity  $g$ . The solid curve was calculated using a L.J. (12,6) potential for the system K-Kr. The dashed line represents  $Q_{LL}$  resulting from only the attractive part of this potential.

a semi-classical picture these two contributions have a phase difference which depends upon the energy. Due to the interference of these two contributions the differential cross section will show an undulatory behaviour as a function of the energy. As a result of this the total cross section, being the integral over all angles of the differential cross section, also oscillates.

The velocities at which the glory extrema appear provide useful information about the interaction potential and can experimentally be determined very accurately. For all the systems we measured, a number of glory extrema could be resolved. The results are described in Chapter IV, where also an interpretation in terms of interaction potentials is given.

### 3. EXPERIMENTAL LIMITATIONS

An idealized experimental method for measuring the total cross section is as follows. First the full beam intensity  $I_0$  of a *parallel beam* (1) of molecules with *uniform velocity* (2) is measured. Following this

the scattering chamber is filled with a gas consisting of molecules at rest (3) and the attenuated beam intensity  $I$  is measured. The *collimator and detector slit* are *infinitely small* (4), so as to be sure that no deflected molecules are detected. In practice condition (1) and (4) are not obeyed and there is a finite probability  $W(\theta)$  that a molecule which has been deflected over an angle  $\theta$  still reaches the detector. Hence the experimentally observed total cross section will be smaller than the true cross section. Also conditions (2) and (3) are not fulfilled and there exists a spread in the relative velocity  $g$ . If  $P(g)$  is the probability of a collision with relative velocity  $g$ , then the average  $\int Q(g) P(g) dg$  is measured instead of the total cross section  $Q(g)$  for one particular relative velocity  $g$ . In an experiment the ideal situation should be approximated as nearly as possible. This finds expression in the design of the experimental equipment, described in Chapter II. The influence of the remaining deviation from the ideal situation is discussed in Chapter III.



## CHAPTER II

## DESCRIPTION OF APPARATUS

## 1. GENERAL

A schematic drawing of the apparatus is shown in Fig. 2.1. It consists of a horizontal, cylindrical vacuum chamber made of stainless steel, which by means of an aluminium separation flange (A) is divided into a source chamber (B) and a main chamber (C). A horizontal supporting rod (D) connects this flange (A) with the head flange (E). All the equipment inside the vacuum chamber is mounted either upon the supporting rod (D) or on one of the flanges. Nearly all feed throughs are positioned on the head flange (E) which is mounted to a frame with rollers. This construction makes it possible to remove the interior equipment as a whole, so that every part of the machine is easily accessible and the alignment is considerably facilitated.

Onto the left side of the flange (A) the primary beam source (F) has been mounted. The beam enters the main chamber through the skimmer (G). On the supporting rod (D) from left to right are found: the cryopump

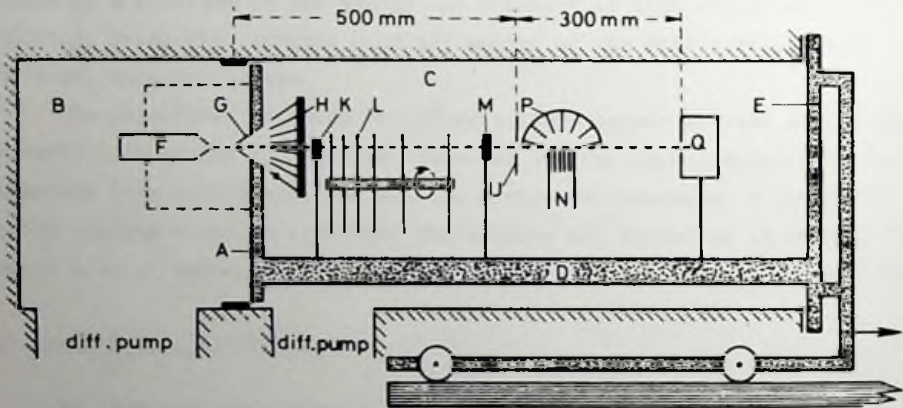


Fig. 2.1 Schematic drawing of the molecular beam apparatus (not to scale). The dotted parts and all the equipment mounted on it can be moved to the right.

with collimator for the primary beam (H), the beam shutter (K), the velocity selector (L), the beam chopper (M), the second collimator (U), the source for the scattering gas (N), the scattering gas cryopump (P), and the beam detector (Q). The design and performance of all these parts will be described in this Chapter. This is done as far as being useful or necessary in one of three respects:

- a. in facilitating the interpretation of the cross section measurements;
- b. for communicating special design features which are of general interest;
- c. for informing subsequent users of this apparatus.

## 2. PRIMARY BEAM SOURCE

In order to obtain a primary beam of high intensity we followed the idea of Kantrowitz and Grey, who in 1951 suggested the production of so-called supersonic molecular beams [KAN 51]. However, at the time we started our investigations the experimental realisation of their idea was still in development. Therefore we performed a rather extensive study of the optimum conditions for this type of beam formation.

### *a. Principle*

The production of supersonic molecular beams is illustrated in Fig. 2.2. A gas is flowing from a source (F) at a pressure of a few hundred torr into vacuum through a small nozzle (R). Beyond the nozzle the gas expands and a supersonic flow into the axial direction arises. A skimmer (G) is placed at a distance  $d$  from the nozzle, where the density of the gas has become sufficiently low, so that a collisionless flow in the main chamber downstream of the skimmer is obtained. By collimation a beam can be formed.

### *b. Design*

The source (F) has been made of brass and can be moved in three perpendicular directions, one of them parallel to the centerline. Provisions are made for gas inlet and pressure measurement by means of a membrane manometer. The nozzle is either from brass or quartz. The dia-

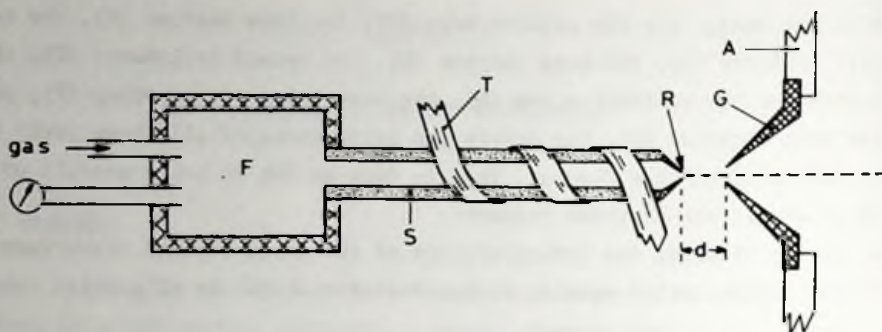


Fig. 2.2 Schematic drawing of the source arrangement for the supersonic molecular beam.

meters of the nozzle opening range from 20 to 250  $\mu$ . Following Cavallini [CAV 71] a quartz nozzle is made from a 5 cm long capillary (S) with outer and inner diameter of 2 mm and 1 mm respectively. The capillary is first closed at one end by melting and then ground until a small hole appears. The quartz nozzle is sealed to a brass holder to be fit to the source. About the tip of the nozzle a Rhenium ribbon (T) of dimensions 50 x 1 x 0.025 mm is wound over a length of 5 mm. By controlling an electric current through this ribbon the temperature of the nozzle can be continuously varied. With 4 A at 8 V the maximum admissible nozzle temperature of about 1300 K is obtained. The velocity of the beam particles can be increased by a factor two in this way. Due to the small heat capacity of the quartz capillary the response time of this system is only a few minutes.

The conical skimmer (G) extends 11 mm from flange (A) and has a very sharp edged hole. The inner and outer top angle of the cone are 50° and 70° respectively. The brass skimmers are made by first machining the inside, filling it with a mould and then machining the outside until a hole of the desired diameter is obtained. The applied diameters range from 100 to 500  $\mu$ .

### c. Beam Formation

For a comprehensive review on this subject we refer to the publications of Knuth [KNU 64] and French [FRE 65]. Here we confine ourselves to a short introduction and an enumeration of the equations required.

The expansion of the source gas between nozzle and skimmer is assumed to be isentropic. The temperature of the gas decreases and the random translational and the internal energy of the molecules is partly converted into the translational energy of a directed gas flow with bulk velocity  $u$  in the axial direction. The properties of this gas flow at a certain distance from the nozzle are determined by the source conditions (temperature  $T_0$ , sound velocity  $a_0$ , number density  $n_0$ ) and the local Mach number  $M$  which is defined as

$$M = u/a \quad 2.1$$

where  $a$  denotes the local sound velocity. The Mach number increases with increasing distance from the nozzle. Numerical calculations of  $M$  have been performed by Owen and Thornhill [OWE 48]. Formula's for temperature, density and flow velocity on the centerline can be found in SHA 53. For a gas with specific heat ratio  $\gamma$  the flow velocity  $u$  becomes:

$$u = a_0 \left[ \frac{2M^2}{2 + (\gamma - 1) M^2} \right]^{\frac{1}{2}} \quad 2.2$$

If the mean free path of the gas molecules at the skimmer entrance is larger than the skimmer diameter and if moreover the skimmer does not disturb the isentropic expansion between nozzle and skimmer, the molecules passing through it into the main chamber will form a beam. The Mach number at the skimmer entrance  $M_s$  is the determining factor for the characteristics of this beam. In particular the beam will be less divergent the larger the Mach number  $M_s$  is. This is because a large Mach number also implies relatively small velocities in the directions perpendicular to the beam. Consequently with a large  $M_s$  value very high beam intensities in the forward direction can be obtained. For comparison, and for later reference, we consider also the situation in which the skimmer opening is used as an effusive source by establishing a uniform pressure  $p_1$  in the source chamber. Then the initial velocity distribution in front of the skimmer is isotropic, which results in a much larger divergence of the beam molecules and consequently in a much smaller intensity in the forward direction.



Forward beam intensities for supersonic and effusive beams can according to Parker et al. [PAR 61] be calculated in  $\text{mol sr}^{-1}\text{s}^{-1}$  from the following equations:

supersonic beam (for  $M_S > 3$ ):

$$I = \frac{n_S a_O A_S M_S (3 + \gamma M_S^2)}{2\pi [1 + \frac{1}{2}(\gamma - 1)M_S^2]^{\frac{1}{2}}} \quad 2.3$$

effusive beam:

$$I = \frac{n_S a_S A_S}{4\pi} \left[ \frac{8}{\pi\gamma} \right]^{\frac{1}{2}} \quad 2.4$$

Here the area of the skimmer hole is denoted with  $A_S$ , while  $n_S$  and  $a_S$  are the number density and the sound velocity at the skimmer entrance.  $\gamma$  is the specific heat ratio. The intensity of both types of beam is limited by the condition that the flow downstream of the skimmer should be collision free. This condition will be fulfilled if the mean free path  $\lambda_S$  at the skimmer entrance is larger than the skimmer opening diameter, which implies a maximum admissible value for  $n_S$ .

Let us now consider the individual velocities  $v$  in the laboratory system of the beam molecules. For the velocity distribution  $F_2(v)$  of beam molecules per unit of time passing a unit of area holds:

supersonic beam:

$$F_2(v) \sim v^3 \exp \left[ \frac{-\gamma M_S^2 (v - u_S)^2}{2 u_S^2} \right] \quad 2.5$$

effusive beam:

$$F_2(v) \sim v^3 \exp \left[ \frac{-\gamma v^2}{2 a_S^2} \right] \quad 2.6$$

Eq. 2.5 reveals that with increasing Mach number the velocity distribution narrows. From eqs. 2.5 and 2.6 the peak velocities  $v_m$  can be derived:

supersonic beam:

$$v_m = u_s \left\{ \frac{1}{2} + \frac{1}{2} [1 + 12/\gamma M_s^2]^{1/2} \right\} \quad 2.7$$

effusive beam:

$$v_m = a_s [3/\gamma]^{1/2} \quad 2.8$$

where  $u_s$  is the flow velocity at the skimmer entrance.

For a calculation of the desirable pumping capacities two formulas are still required. The mass flow  $G$  through the nozzle into the source chamber is [SHA 53]:

$$G = p_o M_o^{1/2} A_o \left[ \frac{2\gamma}{(\gamma + 1) RT_o} \right]^{1/2} \left[ \frac{2}{\gamma + 1} \right]^{1/(\gamma-1)} \quad 2.9$$

where  $p_o$  is the source pressure,  $A_o$  is the area of the nozzle hole,  $M$  the molar mass of the source gas and  $R$  the molar gas constant. The number of molecules  $N$ , which per second flow through the skimmer into the main chamber is [PAR 61]:

supersonic beam:

$$N = n_s a_o A_s M_s \left[ 1 + \frac{1}{2} M_s (\gamma - 1) \right]^{-1/2} \quad (M_s > 3) \quad 2.10$$

effusive beam:

$$N = \frac{1}{4} n_s A_s a_s (8/\pi\gamma)^{1/2}$$

#### d. Beam Intensities

Our first measurements of beam intensities were performed with nitrogen as the source gas. As a detector at that time an ionization manometer provided with a long narrow entrance channel to admit the beam was used. With this detector absolute beam intensities could roughly be determined, so that the results could be compared with theory.

As a first check we measured the intensity of an effusive beam, using the skimmer as a source slit. During these measurements the gas is admitted into the source chamber by an inlet far from the skimmer, so

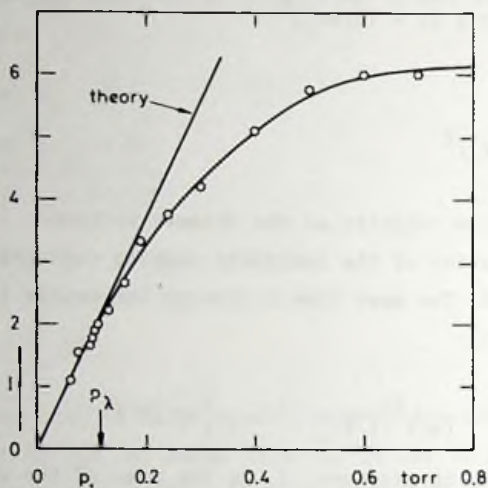
$10^{16} \text{ mol sr}^{-1}\text{s}^{-1}$ 

Fig. 2.3 Intensity  $I$  of an effusive nitrogen beam from the skimmer, as a function of the uniform pressure  $p_1$  in the source chamber. At the pressure  $p_\lambda$  the mean free path  $\lambda$  in the source chamber equals the skimmer diameter  $d_s$ . The theoretical line was calculated from Eq. 2.4.

the density  $n_s$  at the skimmer entrance is proportional to the source chamber pressure  $p_1$ . In Fig. 2.3 is shown the measured beam intensity  $I$  as a function of  $p_1$ , together with the theoretical intensity calculated from Eq. 2.4. At low pressures the agreement is satisfactory. The only deviations occur for pressures above  $p_\lambda$ , for which the mean free path  $\lambda_s$  equals the skimmer diameter  $d_s$ .

Intensities of supersonic nitrogen beams have been measured for two different nozzle diameters  $d_0$ . In Fig. 2.4 the results obtained with  $d_0 = 250 \mu$  for different nozzle skimmer separations  $d$ , together with two theoretical curves calculated from Eq. 2.3 are shown. Similar results with  $d_0 = 50 \mu$  are depicted in Fig. 2.5, where not all the curves reveal a maximum. This is because the source pressure  $p_0$  was restricted to values below 5 atm. Deviations of the observed intensities from theory can be explained as follows:

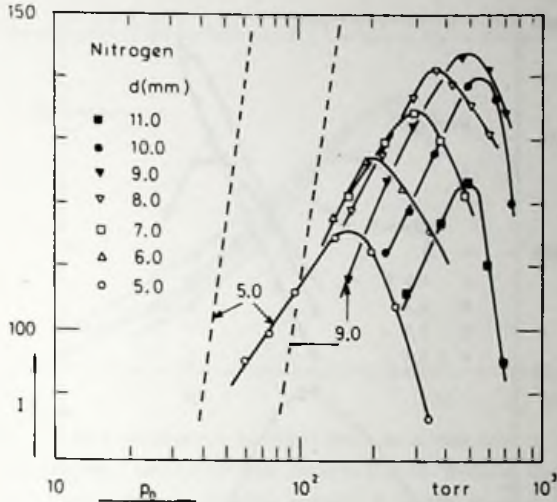
$10^{16} \text{ mol sr}^{-1} \text{ s}^{-1}$ 

Fig. 2.4 Intensity  $I$  of a supersonic nitrogen beam as a function of the source pressure  $p_0$ , for different nozzle-skimmer separations  $d$ . The source chamber pressure is  $2 \times 10^{-2}$  torr at the most; the skimmer diameter  $d_s = 400 \mu$ , the nozzle diameter  $d_0 = 250 \mu$  (large nozzle). The solid lines give experimental results, the dashed lines theoretical intensities calculated from Eq. 2.3 for  $d = 5.0$  mm and  $d = 9.0$  mm.

- $\alpha$ )  $p_0$  large and  $d$  small; this implies a large value for  $n_s$  so that the mean free path  $\lambda_s$  becomes smaller than the skimmer diameter and the intensity will reach a maximum value just as in the case of an effusive beam (Fig. 2.3). Moreover the molecules reflected from the skimmer will disturb the ideal isentropic expansion and can even cause a so-called detached shock in front of the skimmer [FEN 63].
- $\beta$ )  $p_0$  small and  $d$  large;  $n_s$  becomes very small and the expansion ceases to be isentropic at a certain distance from the nozzle due to the insufficient number of collisions. Molecular flow already occurs upstream from the skimmer. The Mach number no longer increases with increasing distance from the nozzle but reaches a final value [AND 66a, FIS 67], which can be considerably smaller than theory predicts.
- $\gamma$ )  $p_0$  large and  $d$  large; the large background pressure  $p_1$  resulting from the large  $p_0$  can in this case attenuate the beam over a long



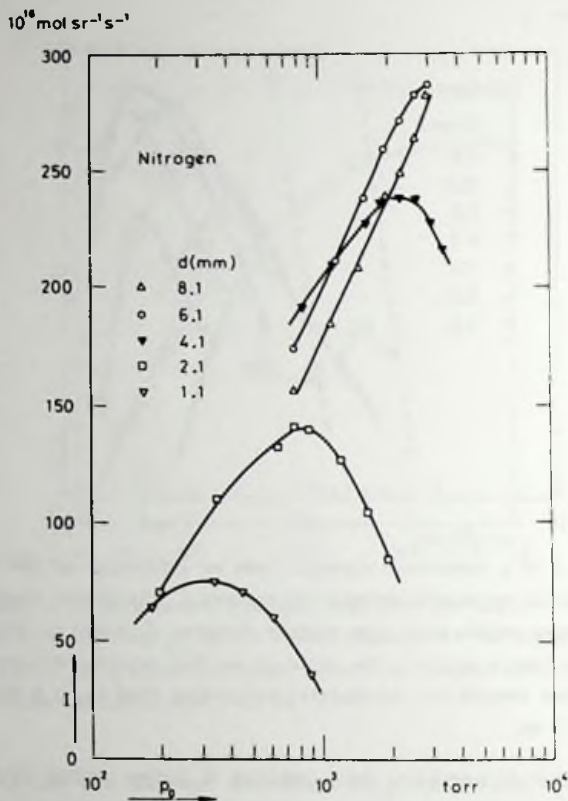


Fig. 2.5 Intensity  $I$  of a supersonic nitrogen beam as a function of the source pressure  $p_0$ , for different nozzle-skimmer separations  $d$ . The largest appearing source chamber pressure  $p_1$  is  $5 \times 10^{-3}$  torr;  $d_s = 400 \mu$  and  $d_o = 50 \mu$  (small nozzle).

distance before it arrives at the skimmer [BIE 66, AND 66b].

The results depicted in Figs. 2.4 and 2.5 confirm the results of other investigators [FEN 63, DEC 63, SCO 68, VAL 64, SCO 63, BIE 66].

For the measurements on supersonic beams described so far, pressures  $p_1$  in the source chamber up to about  $10^{-2}$  torr had to be accepted. By replacing the  $1200 \text{ l s}^{-1}$  diffusion pump by a  $5500 \text{ l s}^{-1}$  type an increase in maximum intensity of 50% and a considerable improvement of beam stability could be obtained. The measurements of Fig. 2.4 were repeated and the results in arbitrary units are shown in Fig. 2.6. Qualitatively the results are similar, but the maximum intensity is now attained at

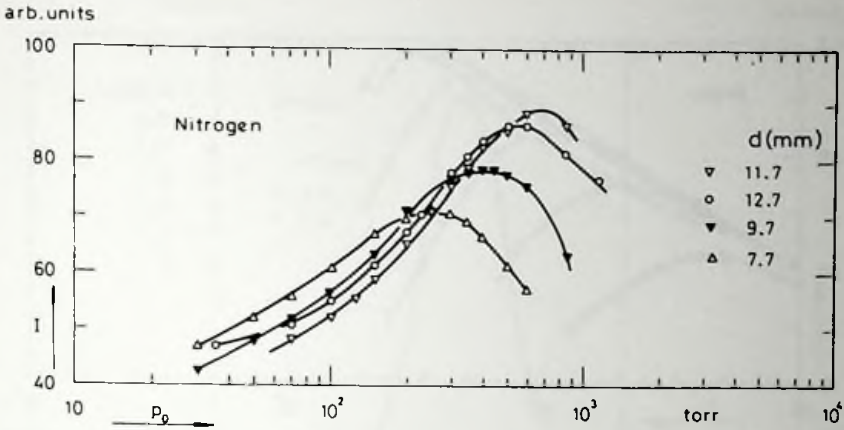


Fig. 2.6 Intensity  $I$  of a supersonic nitrogen beam as a function of the source pressure  $p_0$ , for different nozzle skimmer separations  $d$ . Maximum source chamber pressure  $p_1 = 10^{-3}$  torr (improved pumping speed);  $d_s = 400 \mu$  and  $d_o = 250 \mu$  (large nozzle).

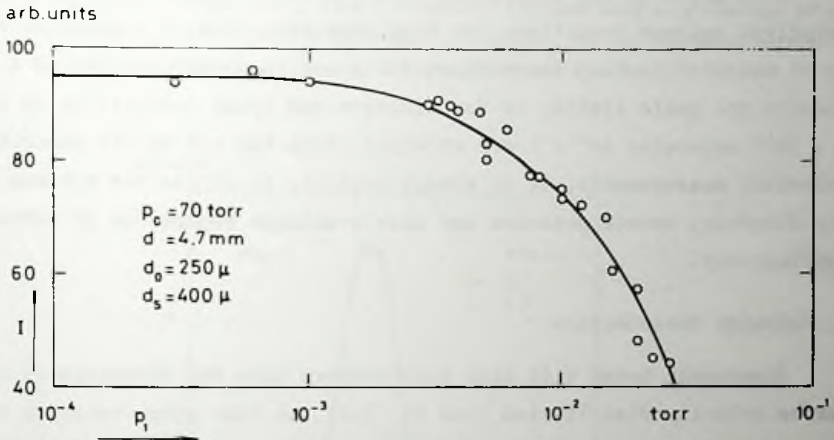


Fig. 2.7 Intensity  $I$  of a supersonic nitrogen beam as a function of the background pressure  $p_1$  in the source chamber.

$d \approx 12.0$  mm and  $p_0 \approx 750$  torr, compared with  $d \approx 9.0$  mm and  $p_0 \approx 500$  torr in the earlier measurements. The effect of  $p_1$  upon the beam intensity is clearly demonstrated in Fig. 2.7. One can see from this representative example that a value of  $10^{-3}$  torr or lower for  $p_1$  is desirable to prevent attenuation of the beam.

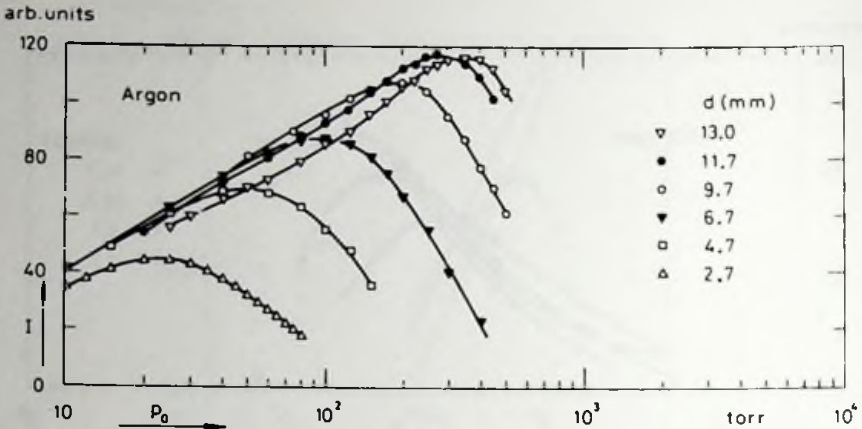


Fig. 2.8 Intensity  $I$  of a supersonic argon beam as a function of the source pressure  $p_0$ , for different nozzle-skimmer separations  $d$ . Maximum source chamber pressure  $p_1 = 10^{-3}$  torr,  $d_s = 400 \mu$  and  $d_o = 250 \mu$ .

With argon as the source gas intensities have also been measured to establish optimum conditions for beam formation. Fig. 2.8 shows an example of measured Ar-beam intensities for a nozzle diameter  $d_o = 250 \mu$ . The results are quite similar as for nitrogen and again intensities up to  $3 \times 10^{18}$  molecules  $\text{sr}^{-1}\text{s}^{-1}$  are attained. With the aid of the described intensity measurements, it is always possible to choose the optimum nozzle diameter, source pressure and nozzle-skimmer separation in subsequent applications.

#### e. Velocity Distribution

Supersonic beams with high Mach numbers have the advantage of a narrow velocity distribution (see Eq. 2.5), so that after velocity selection a larger part of the total intensity remains available. Examples of the observed detector signal  $S$  as a function of the velocity  $v_o$  transmitted by the velocity selector are given in Fig. 2.9 and Fig. 2.10. The velocity distribution  $F_2(v)$  differs only slightly from  $S(v_o)$  (see par. 3c of this Chapter). The expected increase of Mach number (i.e. decrease of half width) with increasing nozzle-skimmer separation  $d$  is clearly demonstrated. Still larger Mach numbers up to 25 have also been observed. Further analysis of velocity distributions is given in the next two sections.

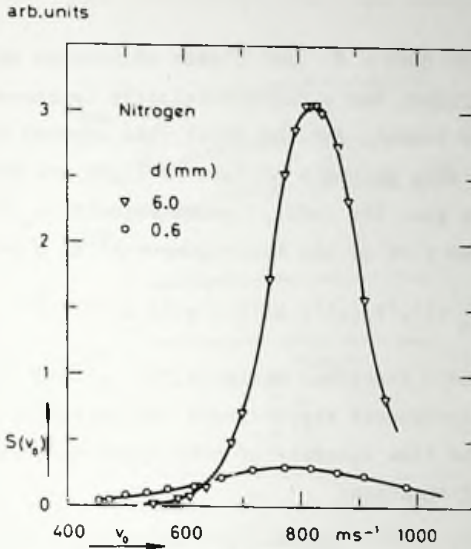


Fig. 2.9 The detector signal  $S(v_0)$  from a supersonic nitrogen beam as a function of the velocity  $v_0$  transmitted by the velocity selector, for two different nozzle-skimmer separations  $d$ .  $T_0 = 295 \text{ K}$ ,  $d_s = 400 \mu$  and  $d_0 = 250 \mu$ .

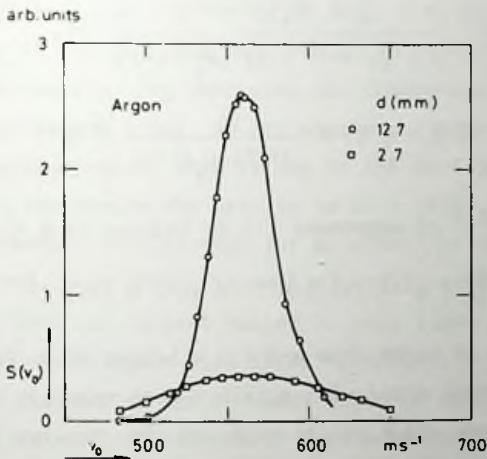


Fig. 2.10 The detector signal  $S(v_0)$  from a supersonic argon beam as a function of  $v_0$ , for two different values of  $d$ .  $T_0 = 295 \text{ K}$ ,  $d_s = 400 \mu$  and  $d_0 = 250 \mu$ .



### f. Seeded Beams

With a supersonic nozzle at 1300 K beam velocities up to  $1100 \text{ m s}^{-1}$  for argon can be realized. For a further velocity increase we used the technique of "seeded beams", for the first time applied by Becker and Henckes [BEC 56]. In this method a mixture of light and heavy molecules is used as the source gas. The initial sound velocity  $a_0^{(1,2)}$  of this mixture is larger than that of the heavy component as a pure gas:

$$a_0^{(1,2)} = [ R T_0 \gamma^{(1,2)} / (x^{(1)} M^{(1)} + x^{(2)} M^{(2)}) ]^{1/2} \quad 2.11$$

Herein  $x$  stands for mole fraction, while (1,2), (1) and (2) refer to the mixture and the two components respectively. Substitution of  $a_0^{(1,2)}$  in Eq. 2.2 yields for the flow velocity of both components after expansion,  $u^{(1,2)}$ , the following equation:

$$u^{(1,2)} = a_0^{(1,2)} \left[ \frac{2\{M^{(1,2)}\}^2}{2 + (\gamma^{(1,2)} - 1) \{M^{(1,2)}\}^2} \right]^{1/2} \quad 2.12$$

By substitution in Eq. 2.7 one finds for the peak velocity of component (1)

$$v_m^{(1)} = a_0^{(1,2)} \left[ \frac{2 \{M_s^{(1,2)}\}^2}{2 + (\gamma^{(1,2)} - 1) \{M_s^{(1,2)}\}^2} \right]^{1/2} \cdot \left[ \frac{1}{2} + \frac{1}{2} \left( 1 + \frac{12}{\gamma^{(1,2)} \{M_s^{(1)}\}^2} \right)^{1/2} \right] \quad 2.13$$

The Mach number  $M_s^{(1)}$  of component (1) is related to  $M_s^{(1,2)}$  by

$$M_s^{(1)} = M_s^{(1,2)} \left[ M^{(1)} / (x^{(1)} M^{(1)} + x^{(2)} M^{(2)}) \right]^{1/2} \quad 2.14$$

Let now (1) denote an argon atom and (2) a helium atom. From eq. 2.13 one can see that the argon atoms will attain a peak velocity  $v_m^{(1)}$  which is larger than when pure argon gas is expanded. The smaller the mole fraction  $x^{(1)}$  of argon in the mixture, the larger  $v_m^{(1)}$  becomes. In the limit of zero argon concentration the peak velocity  $v_m^{(1)}$  will be increased by a factor  $\{M^{(1)}/M^{(2)}\}^{1/2}$  compared to the peak velocity of a 100% argon beam at the same source temperature. For the production of argon beams

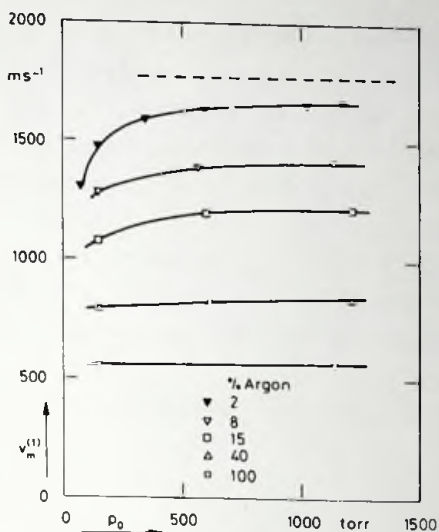


Fig. 2.11 Measured peak velocities  $v_m^{(1)}$  as a function of source pressure  $p_0$ , for argon beams produced by expanding Ar-He mixtures of different compositions (solid curves). The dashed line is the theoretical limit for zero argon concentration.  $T_0 = 293 \text{ K}$ ,  $d = 4.0 \text{ mm}$ ,  $d_s = 120 \mu$  and  $d_o = 50 \mu$ .

with velocities up to  $4300 \text{ m s}^{-1}$  we used the following mixtures: 40%, 15%, 8% and 2% Ar in He; 5% Ar in  $\text{H}_2$ . Fig. 2.11 shows the measured peak velocities  $v_m^{(1)}$  for the four employed Ar-He mixtures as a function of the source pressure  $p_0$  together with the theoretical limit for zero argon concentration (dashed line). At low source pressures  $v_m^{(1)}$  does not yet attain its maximum value. This is due to the fact that already at a short distance from the nozzle the density is at a level where the frequency of collisions becomes insufficient for an effective energy exchange between Ar and He atoms. This effect is most clearly demonstrated by the 2% mixture because then the largest number of collisions is required to accelerate the Ar atoms to their high final velocity.

The Mach numbers of the Ar beams attained values up to 30. A few illustrative velocity distributions have been depicted in Fig. 2.12 and Fig. 2.13, where the normalized detector signal  $S(v_o)/S(v_o)_{\text{max}}$  has been plotted as a function of the velocity  $v_o$  transmitted by the velocity selector. In Fig. 2.12 it is shown that with increasing source pressure  $p_0$  the width of the curves decreases and the peak velocity increases.

This implies that the Mach number increases, although the nozzle skimmer separation  $d$  is the same for all curves. In Fig. 2.13, where  $p_0$  is constant, the differences in the data are small, in spite of the different nozzle skimmer separations. Thus at low pressures the value of the Mach number and consequently the peak velocity is determined by  $p_0$  rather than by  $d$ .

Also Kr beams up to  $4300 \text{ m s}^{-1}$  have been produced using the following mixtures: 30% and 2% Kr in He and 0.3% Kr in  $\text{H}_2$ . For all Ar and Kr mixtures beam intensities in the order of  $10^{18} \text{ mol sr}^{-1}\text{s}^{-1}$  could be obtained.

The above results agree with the findings of other authors [BEC 56, KLI 64, FEN 63].

### 3. VELOCITY SELECTOR

#### *a. Design*

The velocity selector used for the measurements is of the slotted disk type. It is almost identical with the one described by Trujillo et al. [TRU 62] and was manufactured by Werkspoor N.V. Amsterdam according to a design of the F.O.M. Laboratory in Amsterdam [POL 68, POL 70b]. The parameters of the selector are mentioned in Table 2.1, in which the nomenclature of Hostettler and Bernstein [HOS 60] is used and explained. The relation between rotor frequency  $\nu_0$  in Hz and the nominal transmitted velocity  $v_0$  in  $\text{m s}^{-1}$  is:

$$v_0 = 2\pi \nu_0 L/\phi = 9.00 \nu_0 \quad 2.15$$

The apparatus was designed for a maximum rotation frequency of 800 Hz. In our experiments the highest beam velocities employed were  $4500 \text{ m s}^{-1}$ , which corresponds with a rotation frequency of 500 Hz. The selector was originally provided with needle bearings, which had to be cleaned after 5 to 10 hours working. After replacing them by ball bearings manufactured by M(iniature) P(recision) B(earings) Inc. (Keene, New Hampshire) the selector has been working without any trouble for more than 500 hours, with continuous periods up to 60 hours.

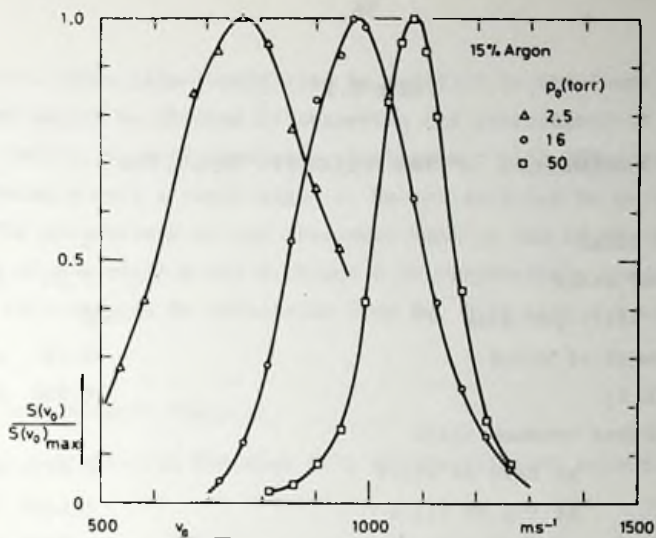


Fig. 2.12 The normalized detector signal  $S(v_0)/S(v_0)_{\max}$  of a supersonic argon beam, produced with a 15% Ar-85% He mixture, as a function of the velocity  $v_0$  transmitted by the velocity selector, for three different source pressures  $p_0$ .  $T_0 = 293$  K,  $d = 5.0$  mm,  $d_s = 450 \mu$  and  $d_0 = 250 \mu$ .

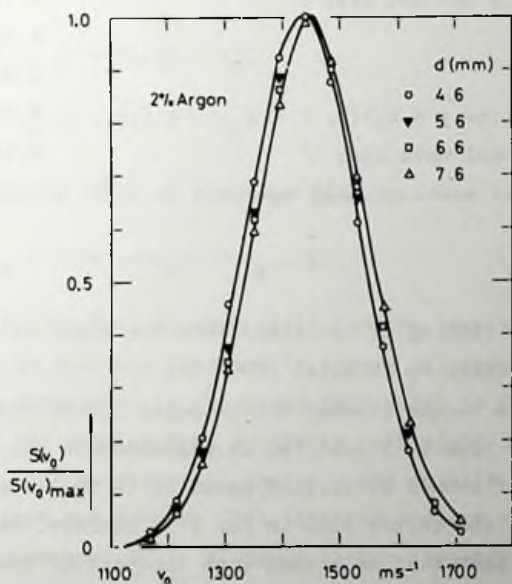


Fig. 2.13 The normalized detector signal  $S(v_0)/S(v_0)_{\max}$  of a supersonic argon beam, produced with a 2% Ar-98% He mixture, as a function of  $v_0$ , for four different nozzle-skimmer separations  $d$ .  $T_0 = 293$  K,  $p_0 = 1140$  torr,  $d_s = 120 \mu$  and  $d_0 = 50 \mu$ .



Table 2.1

## PARAMETERS OF THE VELOCITY SELECTOR

Number of disks	8	
Diameter of disks	15.20	cm
Number of slits per disk	360	
Radial length of slits	0.60	cm
Slit width $\ell_1$	0.050	cm
Wall thickness between slits		
at base of slits	0.0725	cm
at top of slits	0.0825	cm
average value $\ell_2$	0.0775	cm
Average radius $r$	7.3	cm
Disk thickness $d$	0.130	cm
Length of rotor $L$	25.5	cm
Displacement angle of last disk $\phi$	0.1773	rad
$\dot{\gamma}_R = \ell_1/r\phi$	0.039	
$\beta = d/L$	0.005	
Fractional open time $\eta = \ell_1/(\ell_1 + \ell_2)$	0.392	
Effective fractional open time $\eta'$	0.34	
Resolution $R$ (full width at half maximum)	0.034	

*b. Alignment*

The correct positioning of the disks onto the shaft is achieved in the same way as described by Politiek [POL 70b].

From outside the vacuum chamber the selector can be moved into and out of the molecular beam by a parallel displacement of the rotor axis. The rotor axis itself should be aligned parallel to the molecular beam, because only then is the factor 9.00 in Eq. 2.15 correct. For this alignment we use a laser beam that coincides with the path of the molecular beam. With the disks of the selector just out of the beam two small metal sheets (0.2 mm thick) are placed at the circumferences of the first and the last disk, in such a way that the connection line is parallel to the

rotor axis. This line should also be parallel to the laser beam, and this can easily be checked by observing the coincidence of the shadows of the sheets. A small remaining misalignment will effectively increase or decrease  $\phi$  with a small angle  $\delta$ . We estimate  $\delta/\phi$  to be smaller than 0.8%. The uncertainty in the frequency reading and in the mechanical adjusting of the angle  $\phi$  are 0.2% and 0.4% respectively, so that the transmitted velocity can be calculated from Eq. 2.15 with a maximum error of 1.4%.

### c. The Transmission Function

The transmission function  $B(v)$  of the velocity selector is given by [HOS 60]:

$$B(v) = \eta [1 - \{(1 + \beta) v_0/v - 1\}/\gamma_R] \quad \text{for } v_{\min} < v < v_0 ,$$

$$B(v) = \eta [1 + \{(1 - \beta) v_0/v - 1\}/\gamma_R] \quad \text{for } v_0 < v < v_{\max} \quad 2.16$$

$$\text{and } B(v) = 0 \quad \text{for } v < v_{\min} \text{ and } v > v_{\max}$$

$$\text{with } v_{\min} = v_0 (1 + \beta)/(1 + \gamma_R)$$

$$v_{\max} = v_0 (1 - \beta)/(1 - \gamma_R) \quad 2.17$$

The resolution  $R$  (FWHM of  $B(v)$ ) is given by

$$R = (\gamma_R - \beta)/(1 - \gamma_R)^2 \approx \gamma_R - \beta .$$

Eq. 2.16 for  $B(v)$  is only valid for the ideal case of a parallel beam, while in practice the beam is always divergent. For the case that the maximum divergence in the plane tangential to the selector disks is  $\alpha_0$ , so that the angular beam spread in this plane is limited to the range  $-\alpha_0 < \alpha < \alpha_0$  and moreover all angles  $\alpha$  are equally probable (uniform divergence), Dash and Sommers [DAS 53] have studied the influence of the beam divergence upon  $B(v)$ . Although in our geometry not all angles  $\alpha$  are equally probable, because of the circular shape of the beam defining source and detector slits, the results of DAS 53 can still be used to approximately account for this effect. If our actual non-uniform angular

distribution of detected beam particles (with  $\alpha_0 = 5 \times 10^{-4}$ ) is replaced by a uniform distribution of equal total probability, an effective value for  $\alpha_0$  of  $2.5 \times 10^{-4}$  is obtained. According to Fig. 3 of DAS 53 this will increase the full width at half maximum (FWHM) of  $B(v)$  by about 10%. In the calculations of the next section we have accounted for such a divergence effect on  $B(v)$  by using for  $\gamma_R$  the value 0.044 instead of 0.039.

#### d. Calibration

To make sure that the correct alignment of the selector is maintained under operating conditions we performed a calibration with a molecular beam of known velocity. This was done in the following way. A supersonic argon beam was produced. All source conditions were kept constant and the temperature  $T_0$  of the brass nozzle was measured with a thermocouple. The detector signal  $S(v_0)$  was measured as a function of the nominal transmitted velocity  $v_0$ , as defined by Eq. 2.15. The velocity  $v_m$  at which  $S(v_0)$  shows a maximum should be compared now with the peak velocity calculated from Eq. 2.7. For this calculation one needs to know besides the source temperature  $T_0$  the Mach number  $M_s$ . The theoretical value of the Mach number, belonging to the actual nozzle skimmer separation cannot be used, because it is not sure that the expansion remains isentropic up to the skimmer entrance. Consequently another approach is necessary. According to Eq. 2.5 the Mach number  $M_s$  uniquely determines the ratio of the peak velocity and the half width of the velocity distribution  $F_2(v)$ . Since this ratio  $v_m/\Delta v$  is not affected by the numerical factor in Eq. 2.15 the value of  $M_s$  can in principle also be derived from the observed distribution  $S(v_0)$ . In order to see how this can be done, we must first analyse the relation between  $S(v_0)$  and  $F_2(v)$ . Due to the finite resolution of the velocity selector and to the velocity dependent detector efficiency,  $S(v_0)$  is not identical with the velocity distribution  $F_2(v)$ , but

$$S(v_0) \sim \int v^{-1} B(v) F_2(v) dv . \quad 2.18$$

The factor  $v^{-1}$  accounts for the velocity dependent efficiency of our flow through ionization detector.

For Mach numbers up to 31 we have numerically calculated  $F_2(v)$  from

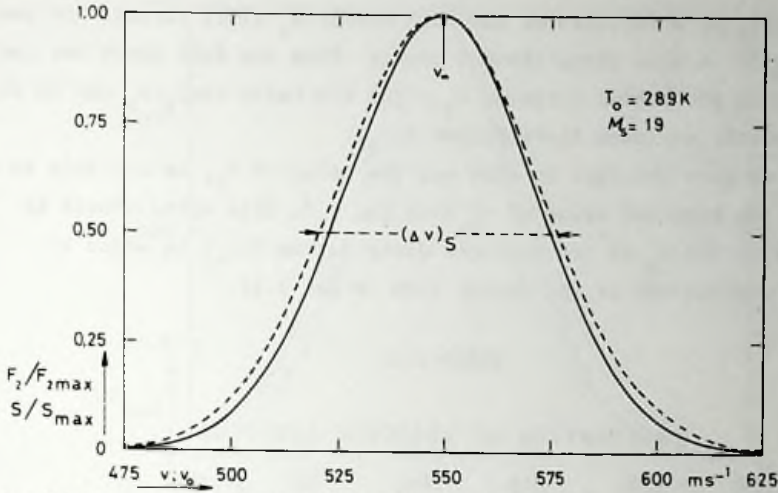


Fig. 2.14 The normalized velocity distribution  $F_2(v)/F_2(v)_{\max}$  (full curve) and the normalized detector signal  $S(v_0)/S(v_0)_{\max}$  (dashed curve) for a supersonic argon beam with Mach number  $M_S = 19$ .

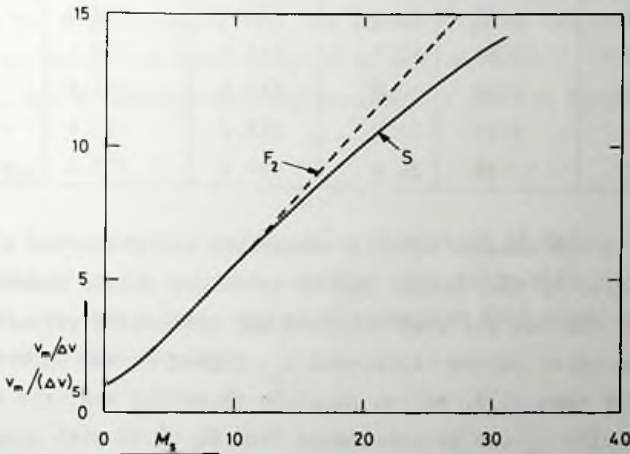


Fig. 2.15 The inverse relative halfwidth  $v_m/\Delta v$  of  $F_2(v)$  and  $v_m/(\Delta v)_S$  of  $S(v_0)$  as a function of Mach number  $M_S$ .

Eq. 2.5 and  $S(v_0)$  from Eq. 2.18. Apart from differences smaller than  $1^\circ/\infty$ , the maxima of  $F_2(v)$  and  $S(v_0)$  appear to be situated at the same peak velocity  $v_m$ . The FWHM  $(\Delta v)_S$  of  $S(v_0)$ , however, is significantly larger than the FWHM  $\Delta v$  of  $F_2(v)$  for the larger values of  $M_S$ . An example, for  $M_S = 19$  is shown in Fig. 2.14. In Fig. 2.15 we have plotted the quan-



tity  $v_m/(\Delta v)_S$  as a function of the Mach number  $M_S$  (full curve). For comparison  $v_m/\Delta v$  is also given (dashed curve). From the full curve one can now determine the actual value of  $M_S$  since the ratio  $(\Delta v)_S/v_m$  can be obtained from the measured distribution  $S(v_o)$ .

Once we have obtained in this way the value of  $M_S$ , we are able to calculate the expected value of  $v_m$  from Eq. 2.7. This value should be compared with the  $v_m$  of the measured distribution  $S(v_o)$  in order to check the correctness of the factor 9.00 in Eq. 2.15.

Table 2.2

## CALIBRATION OF VELOCITY SELECTOR

Date	$T_o$ (K)	$v_m/(\Delta v)_S$	$M$	$v_m$		deviation (%)
				observed (m s <sup>-1</sup> )	calculated (m s <sup>-1</sup> )	
3-2-70	289.8	8.27	15.9	543.5	549.6	- 1.1
	289.6	6.67	12.4	546.3	550.1	- 0.7
14-4-70	294.5	5.92	10.8	554.4	554.5	0.0
	293.7	9.23	17.9	558.2	552.6	+ 1.0
18-5-71	293.7	12.38	25.6	557.5	553.0	+ 0.8

In Table 2.2 the results of this comparison are given for a few beams, which differ by Mach number due to different nozzle diameter or source pressure. One can see that observed and calculated velocity agree within 1.1%. The error in the calculated  $v_m$ , caused by the uncertainty in  $T_o$ , is smaller than 0.2%. We can conclude therefore that the nominal transmitted velocity  $v_o$  can be calculated from Eq. 2.15 with a maximum uncertainty of about 1.5%, a result that agrees satisfactory with the a priori estimated accuracy of 1.4% (see par. 3b).

Fig. 2.16 shows as an example the measurements of the second run on 18-5-71. The full curve has been calculated from Eq. 2.18 for Mach number 25.6. By shifting this curve +0.8% along the  $v_o$  axis in order to fit the observed peak velocity, we obtained the dashed curve. The shape of the curve can now be seen to be in excellent agreement with the data.

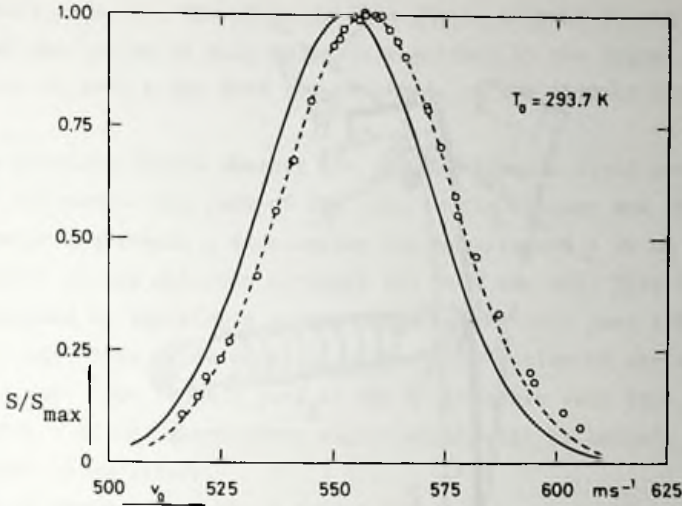


Fig. 2.16. Example of a measurement of  $S(v_0)$  (circles). The full curve has been calculated for  $T_0 = 293.7$  K and  $M_s = 25.6$ . The dashed curve is obtained by shifting the theoretical curve 0.8% to the right.

Only in the high velocity tail the curve slightly departs from the data. Such a deviation has been observed by various authors [CAN 71, SCO 67, ABU 67], but a satisfactory explanation has not yet been given.

#### 4. SHUTTER

The beam shutter consists of a dismantled mA meter. In series with a dry battery and a suitable resistor this meter will show full scale deflection, so that a small piece of aluminium foil glued on top of the pointer will stop the beam.

#### 5. CHOPPER

To improve the signal to noise ratio of the detector output the primary beam is modulated at a fixed frequency of 30 Hz and phase sensitive detection is utilized. For this purpose we designed a beam chopper as depicted in Fig. 2.17, which consists of a metal flag (1) soldered on a vibrating reed (2). The reed is an 0.5 mm thick, 8 mm wide and 12 cm long leaf spring, to which about half way a small piece of

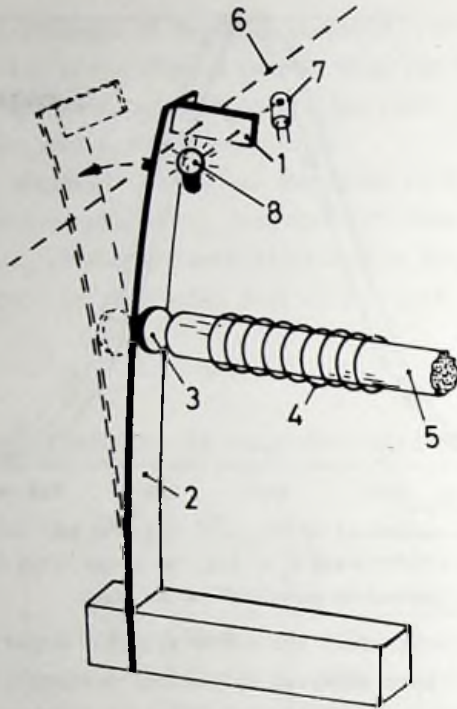


Fig. 2.17 The beam chopper. 1 = chopper flag, 2 = leaf spring, 3 = soft iron, 4 = coil, 5 = core, 6 = primary beam, 7 = photodiode and 8 = lamp.

soft iron (3) has been fixed. A fixed coil (4) opposite to this iron piece electromagnetically drives the chopper. The dimensions of the leaf spring have been chosen such that its resonance frequency equals the fixed 30 Hz of the lock-in amplifier as nearly as possible. Further tuning of the chopper frequency is achieved by changing the weight of the flag (adding or removing excess solder). The coil was made from 0.5 mm thick insulated copper wire, wound in six layers around a ferrocube rod (5) with a length of 8 cm and a diameter of 0.97 cm. A power supply generates a starting current of about 30 Hz in it to start the vibration of the chopper. The amplitude of the vibration is allowed to increase until the flag intercepts the light from a small lamp (7), which illuminates a photodiode (8). At that moment the starting current is automatically stopped and the chopper will start to vibrate at its resonance frequency. To compensate for losses a pulse is now generated

in the coil each time the piece of iron (3) is nearest to the coil. The width and the timing of this pulse is regulated by the signal from the photodiode in such a way that the amplitude of the chopper remains constant.

The question arises whether the electromagnetic field produced by the coil influences the path of the ions in the ionizer and in the mass spectrometer and causes a fluctuating ion beam. Indeed a 30 Hz signal was observed at the detector although the beam was off. This interference was eliminated by applying a second pulse to the coil just 1/60 s after the first one. This pulse does not disturb the motion of the chopper because the soft iron is then just as far as possible away from the coil. We now have a 60 Hz interference signal which will be largely suppressed by the lock-in amplifier.

For an amplitude of about 1.5 cm the necessary starting current is 1A, while only 0.15 A is required to maintain the resonance vibration.

The advantages of this type of chopper are its small dimensions in the beam direction, the absence of bearings, the small power consumption, the extremely good stability (better than 1 in  $10^5$ ) and its reliability.

One historical note may still be of interest. In the beginning our chopper was placed between the primary beam cryopump and the shutter. We then observed an a.c. signal at the detector, even when the shutter stopped the beam. Because this signal had a phase difference with the chopper vibration we were led to the following explanation. When the chopper is in the beam path, the beam molecules are reflected against it and have next a large probability of being directly pumped by the cryopump, which is very near and therefore covers a large angle of space. When the chopper is out of the beam the molecules are reflected against the shutter which is further away from the cryopump so that direct pumping is less probable. A larger number of molecules is now only pumped (by the cryopumps or diffusionpumps) after many collisions with the walls. Thus one can expect the pressure to fluctuate with a frequency of 30 Hz and an amplitude of about  $5 \times 10^{-10}$  torr and this background fluctuation will be observed at the detector. Indeed this spurious effect disappeared when the chopper was placed between selector and scattering chamber, far away from the cryopump.



## 6. PUMPING PROVISIONS

### a. For the Source Chamber

To produce an intensive molecular beam a high source pressure  $p_0$  is required and thus a large amount of gas is exhausted into the source chamber. In the beginning we pumped this gas load with only a  $1200 \text{ l s}^{-1}$  oil diffusion pump. This turned out to be insufficient and caused the source chamber pressure  $p_1$  to be too high and unstable. In par. 2c we remarked already that  $p_1$  should possibly be smaller than  $10^{-3}$  torr. With  $p_0 = 1500$  torr and a  $100 \mu$  nozzle the gas flow will be about  $2 \text{ torr l s}^{-1}$  for argon (Eq. 2.9). Thus  $10^{-3}$  torr can be obtained when the pumping speed amounts  $2000 \text{ l s}^{-1}$ . For this reason we decided to install a  $5500 \text{ l s}^{-1}$  Leybojet diffusion pump, which still has its nominal pumping speed and a good stability at relatively high pressures. The pump has been provided with a water cooled baffle and a valve. Now during our experiments  $p_1$  never exceeded  $2 \times 10^{-3}$  torr.

### b. For the Main Chamber

The gas flow from the source chamber into the main chamber can be calculated with Eq. 2.10 and in our experiments amounts to  $5 \times 10^{-3}$  torr  $\text{l s}^{-1}$  at the most. The partial pressure of the beam gas, however, should be as low as possible (preferably  $<10^{-9}$  torr) because the beam detector is in the main chamber without separate pumping. Thus a high background pressure will result in a poor signal to noise ratio. The main chamber has only been provided with two  $1200 \text{ l s}^{-1}$  oil diffusion pumps with baffles and valves, which yield an effective pumping speed of about  $1000 \text{ l s}^{-1}$ . This is far from being sufficient to realize the desired partial pressure of  $10^{-9}$  torr. We therefore constructed a specially shaped cryopump to capture the off-center beam molecules before they can spoil the vacuum. Our design has been described in detail in a letter with Scoles et al. [SCO 65]. With this cryopump the observed background pressure caused by the primary beam gas was lower than  $2 \times 10^{-9}$  torr, which implies an effective pumping speed of this cryopump in the order of  $10^6 \text{ l s}^{-1}$ .

The scattering gas which is brought into the main chamber by the

secondary beam source is also pumped by means of a cryopump. It turned out to be necessary to improve the design as described in SCO 65. The cold surface of the pump (P) was extended to completely enclose the scattering region except for an entrance and exit hole (2 mm in diameter) for the primary beam (see Fig. 2.18). With this extension (W) the background pressure only increases by about  $1 \times 10^{-9}$  torr when the scattering gas (at the most  $4 \times 10^{-3}$  torr  $\text{g s}^{-1}$ ) is admitted.

When argon is the beam gas it is important to prevent backstreaming of oil, because the mass spectrum of hydrocarbons shows peaks in the vicinity of the argon peak. The diffusion pumps have therefore been provided with nitrogen cooled baffles.

The two cryopumps originally were in thermal contact with a 5 l liquid hydrogen container inside the vacuum chamber. Apart from the question whether the location of a  $\text{H}_2$  container close to a fast rotating velocity selector is safe, this design had two other disadvantages. Firstly it occupied much space inside the vacuum chamber. Secondly it had to be filled every hour and always at the beginning of the filling one unavoidably blows an amount of room temperature  $\text{H}_2$  gas through the tubing and the container. The resulting rise in temperature causes some desorption. This in turn causes a large increase in background pressure which can strongly influence the detector efficiency. We therefore constructed an indirect cooling system for the cryopumps. Helium gas at 21 K and 25 atm is circulated through a closed circuit of tubing, which is in good thermal contact with the cryopumps. Outside the vacuum the helium is cooled in a hydrogen cryostat. The helium is circulated by means of a commercial fast rotating fan. Unfortunately this fan when working has a heat leak of more than 35 W, which should be compared with the 8 W leak of the cryostat and a 3 W heat load of the cryopumps and tubing. Under these circumstances the 10 l cryostat has to be refilled every two hours. Probably this large  $\text{H}_2$  consumption can be decreased by improving the fan. This may be possible because from the 35 W leak only 8 W can be attributed to the conductance of the housing and the fan shaft, the remainder being due to heat transport by the turbulent gas inside the fan.

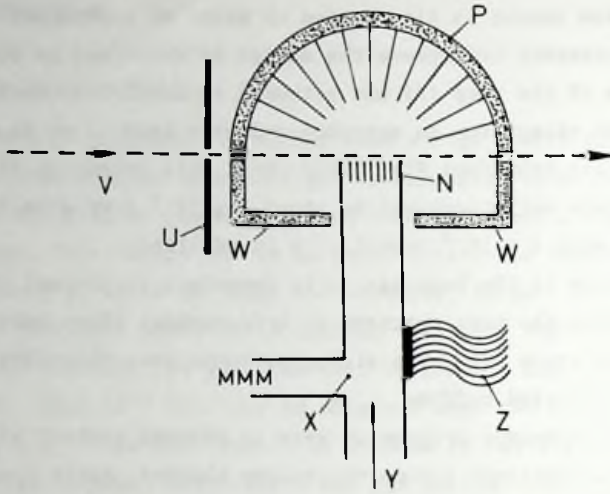


Fig. 2.18 Schematic picture of the scattering gas source. V = primary beam, U = collimator, N = multi channel source, Y = scattering gas inlet, MMM = manometer, P = cryopump, W = cryopump extension and Z = thermal connection with cryovessel.

## 7. SCATTERING GAS SOURCE

### a. General

In designing our scattering gas source the following requirements were considered. First the velocities of the scatterers must be as small as possible, secondly the scattering length should be short and in the third place the amount of admitted scattering gas required to attain 40% attenuation of the primary beam must be small in view of the vacuum requirements.

The scattering gas was originally admitted by effusion through a thin walled slit. Afterwards we have replaced this source by a multi channel source (MCS) in order to decrease the spread of relative velocities. After being collimated the primary beam (V) just skims the slit or the MCS (N), as shown in Fig. 2.18. In the horizontal plane the source can be moved perpendicularly to the primary beam, while together with the collimator it can be moved vertically. The scattering gas (Y) is supplied from a 10 l container at room temperature.

### b. Gas Temperature

In order to decrease the velocity spread the scattering gas is maintained at a low temperature. The argon and krypton gas is cooled down to 83 K, a temperature at which the vapour pressure of krypton still is 6 torr and of argon even higher. The xenon gas is maintained at a temperature of 96 K where the vapour pressure is 0.4 torr. Much lower temperatures cannot be applied because the required scattering gas pressure is about 0.06 torr. The source is maintained at the desired temperature by means of a flexible copper wire connection (Z) to a l & cryovessel inside the vacuum chamber filled with liquid  $N_2$  or  $O_2$ .

### c. Pressure Measurement

The gas density in the scattering region is proportional to the pressure of the gas in the source just before it flows through the slit or the MCS. This pressure should be accurately known in order to obtain precise relative values for the cross section from the beam attenuation data. As a manometer we used an Atlas micro membrane manometer (MMM). By comparison with a carefully designed McLeod manometer we established that the indication of the MMM is linear within 1% (See Fig. 2.19). Two corrections to the measured pressure were required. First one has to account for the thermomolecular pressure difference between room temperature and the cryovessel temperature, which gives a correction of 10% at

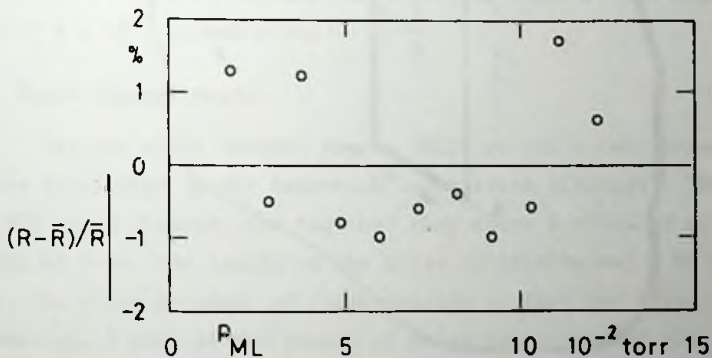


Fig. 2.19 Deviation plot showing the linearity of the MMM.  $R$  is the ratio of the MMM reading and the pressure  $p_{ML}$  as measured with a McLeod manometer,  $\bar{R}$  is the average value of this ratio.



the most. This correction was calculated with a formula given by Dushman [DUS 61]. Secondly the flow through the last 5 cm of the 9 mm wide tubing, from the point where the pressure is measured (X) onto the slit or the MCS (N), is not quite molecular but already of the transition type (see Fig. 2.18). For this slightly viscous flow the conductance of the tubing between X and N is pressure dependent and the measured pressure will no longer be proportional to the gas flow. We therefore performed a calibration to determine the necessary correction to the MMM reading. For this purpose we mounted a calibrated glass capillary in the inlet system. The gas pressure and the pressure drop across the capillary were measured and from this data the gasflow was determined. The simultaneous MMM readings required a correction of at the most 3% in the relevant pressure range 0.03-0.06 torr.

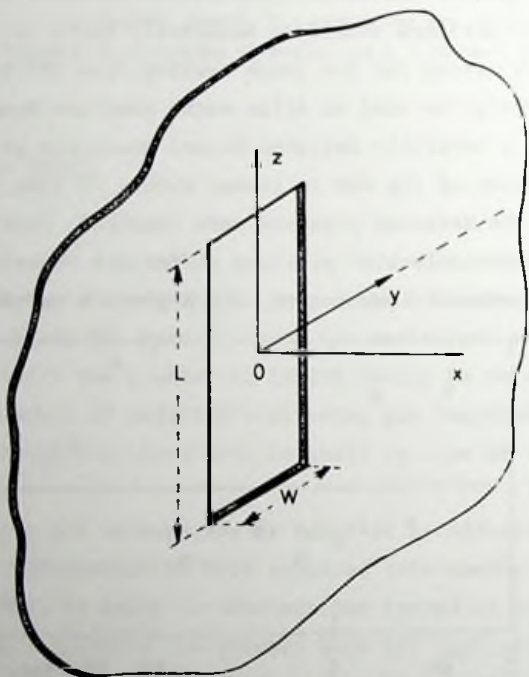


Fig. 2.20 Geometry of the slit source and coordinates used. The primary beam is parallel to the y-axis.

#### d. Slit Source

The slit we used was a  $0.1 \times 3 \text{ mm}^2$  rectangular hole in a  $0.070 \text{ mm}$  thick brass foil. Let us introduce coordinates as indicated in Fig. 2.20. The slit with sides  $W$  and  $L$  is situated in the vertical  $y$ - $z$ -plane, the primary beam is in the  $y$  direction. The origin  $O$  is in the middle of the slit. In considering the density field of the scattering gas after it has passed the slit, we made use of the results of Howard [HOW 61]. He gives a formula for the ratio  $n/n_r$  as a function of  $x$ ,  $y$ ,  $z$ ,  $L$  and  $W$ , with  $n$  being the scattering gas density outside and  $n_r$  the gas density inside the source. Because we wanted to know the total number of scatterers that the primary beam finds on its path, we integrated his equation (9) over  $y$  and found:

$$\int_{-\infty}^{+\infty} n/n_r dy = \frac{1}{2} (W/L)^{\frac{1}{2}} \cdot \pi^{-1} \left\{ \arctg \frac{z/L + 1}{x/L} - \arctg \frac{z/L - 1}{x/L} \right\}$$

$$\equiv \frac{1}{2} (W/L)^{\frac{1}{2}} \cdot F(x/L, z/L) \quad 2.19$$

The function  $F(x/L, z/L)$  is depicted in the Figs. 2.21 and 2.22 as a function of  $x/L$  and  $z/L$  respectively. One can see that the integrated density does not vary more than 20% over the cross section of the primary beam, whose extension in the  $x$ - and  $z$ -direction is indicated by PB in the figures. For a 40% attenuation of the primary beam a source pressure of 0.1 torr at the most is required, which yields a gas flow of about  $4 \times 10^{-3} \text{ torr } \& \text{ s}^{-1}$ .

#### e. Multi Channel Source

For our multi channel source (MCS) we use a collimated holes structure fabricated by the Brunswick Corporation (Chicago). The holes are  $0.050 \text{ mm}$  in diameter and together they cover a circular area with a radius of  $3 \text{ mm}$ . The length of the holes originally was  $3 \text{ mm}$  but we have cut the slice by means of spark erosion so that two slices of  $0.7 \text{ mm}$  each remained. A part of the number of holes was closed up with varnish to be left with a rectangular open area of  $6 \times 1.5 \text{ mm}^2$ . This source is mounted with its long side parallel to the primary beam and its short side in the vertical direction. Here a maximum gas flow of  $2 \times 10^{-3} \text{ torr } \& \text{ s}^{-1}$  at a source pressure of  $5 \times 10^{-2} \text{ torr}$  is required to give 40% attenuation.

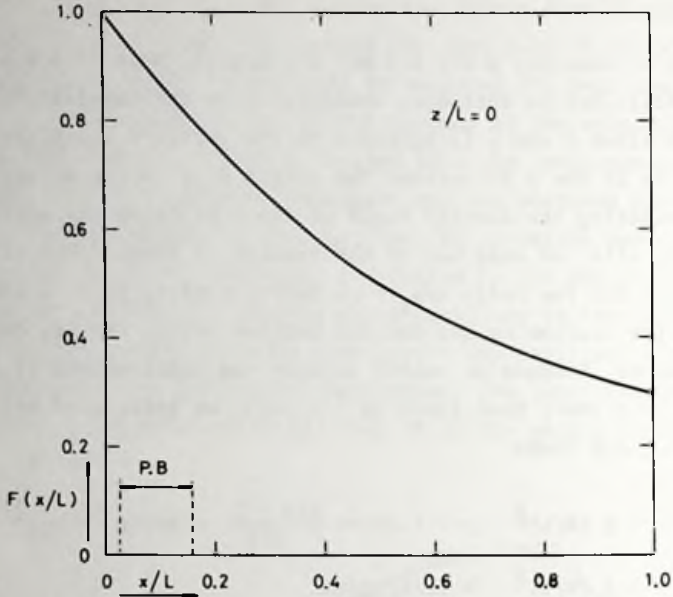


Fig. 2.21 The function  $F(x/L, z/L)$  for  $z/L = 0$ . The position of the primary beam is indicated by P.B.

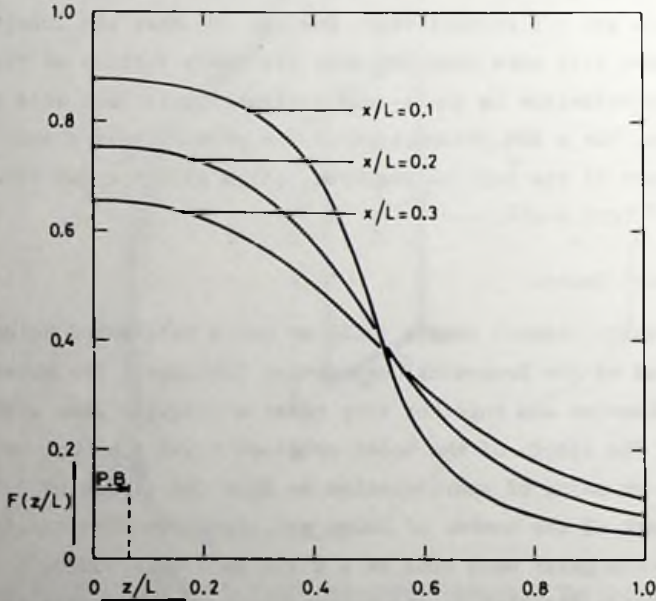


Fig. 2.22 The function  $F(x/L, z/L)$  for three values of  $x/L$ . P.B. is the position of the primary beam.

For the evaluation of total cross section measurements it is important to know the distribution of the relative velocities, with which beam and target particles collide. Therefore one should know the angular distribution of the molecules leaving the MCS. Zugenmaier [ZUG 66] has calculated the intensity  $I(\delta)$  as a function of the total gas flow  $G$  and the angle  $\delta$  between the channel axis and the velocity direction of the molecule. His results are in good agreement with experimental observations (see ZUG 66 and FEL 70). Quantatively we cannot use the results of Zugenmaier, because our channels do not have a circular cross section, the diameter of 0.05 mm being only an average. Therefore we performed measurements of  $I(\delta)$  for different source pressures  $p_{SG}$ , an example of which has been depicted in Fig. 2.23. From these measurements we derived

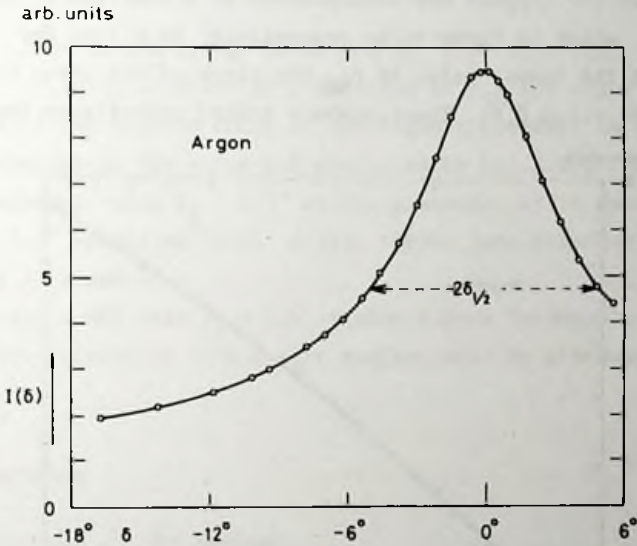


Fig. 2.23 Example of the observed angular distribution  $I(\delta)$  of argon molecules leaving the multi channel source.

the forward intensity  $I(0)$  and the angle  $\delta_{1/2}$  for which  $I(\delta_{1/2}) = \frac{1}{2} I(0)$ . A qualitative comparison of the values of  $\delta_{1/2}$  and  $I(0)$  with the Zugenmaier results is possible. When the mean free path  $\lambda$  in the source is much smaller than the channel length  $L$ , the following proportionalities hold [ZUG 66]:



$$\delta_{\frac{1}{2}} \sim G^{\frac{1}{2}} \quad 2.20a$$

$$I(o) \sim G^{\frac{1}{2}} \quad 2.20b$$

When, however,  $\lambda \gg L$  then

$$\delta_{\frac{1}{2}} = 1.68 a/L \quad 2.21a$$

$$I(o) \sim G \quad 2.21b$$

in which  $2a$  is the diameter of the channels. Our measurements were performed in the transition region where  $\lambda \approx L$ . In Fig. 2.24 the forward intensity  $I(0)$  for krypton has been plotted as a function of the source pressure  $p_{SG}$ , which is known to be proportional to  $G$  (see for instance [JOH 66]). At the lowest value of  $p_{SG}$  the slope of the curve is 0.91, at the highest value 0.61. These numbers indeed approximate the values

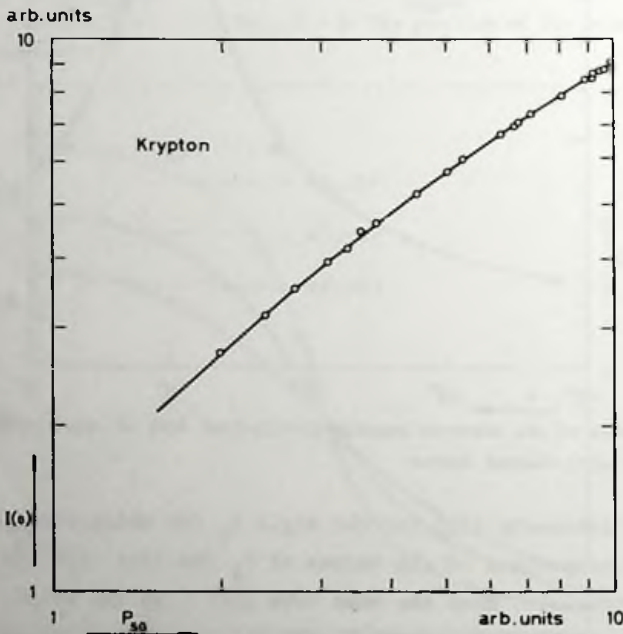


Fig. 2.24 The forward intensity  $I(0)$  of the multi channel source as a function of the pressure  $p_{SG}$  of the Kr gas in the source.

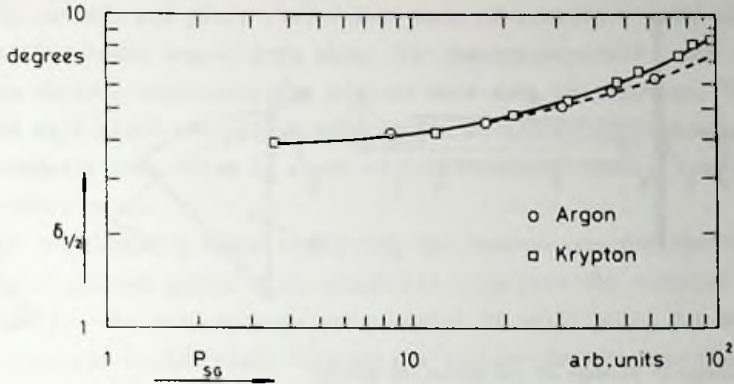


Fig. 2.25 The half-intensity angle  $\delta_{\frac{1}{2}}$  of the angular distribution of Ar and Kr molecules as a function of the pressure  $p_{SG}$  in the multi channel source.

1.0 and 0.5 predicted by Eq. 2.20b and Eq. 2.21b. In Fig. 2.25 the half intensity angle  $\delta_{\frac{1}{2}}$  is shown as a function of  $p_{SG}$  for argon and krypton. The slope of the krypton curve at the highest pressure is 0.45, which again approximates the value 0.5 predicted by Eq. 2.20a. The observed nearly constant value  $\delta_{\frac{1}{2}} = 4.0^\circ$  at low pressures is in fair agreement with the  $3.4^\circ$  predicted by Eq. 2.21a, taking into consideration the uncertainty in  $a$  and  $L$ .

How far a MCS with  $\delta_{\frac{1}{2}} = 4.0^\circ$  yields a more favourable distribution of relative velocities than a slit source, will be discussed in Chapter III par. 3c.

## 8. THE DETECTOR

### a. Construction of the Ionizer

In Chapter I we mentioned already that the detection of neutral non-alkali atoms is performed by ionizing them by means of electron bombardment. For that purpose we decided to build an ionizer according to the design of Weiss. A schematic diagram is shown in Fig. 2.26. In the region enclosed by the anode plate (5), the grid (4), the entrance grid (6) and the exit grid (7) the electron current builds a 5 cm long space charge which is traversed by the primary beam. The voltage in this space charge is forged to decrease along the beam path so as to drive the ions,

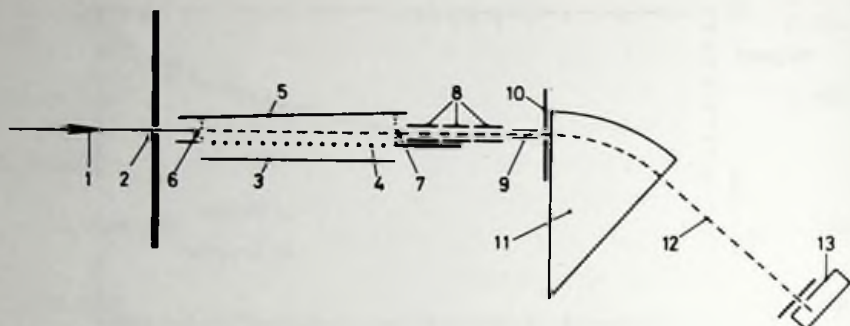


Fig. 2.26 Schematic picture of the detection system.

1 = molecular beam, 2 = detector slit, 3 = cathode, 4 = grid, 5 = anode,  
 6, 7 = entrance and exit grid, 8 = electrostatic lenses, 9 = deflection plates,  
 10 = mass spectrometer slit, 11 = mass spectrometer magnet, 12 = ion beam,  
 13 = particle multiplier.

that are formed, to the end of the space charge, where they are extracted. For a detailed description we refer to Weiss' publication [WEI 61]. Our final version, however, differs from his design in the following respects:

- The total length of the ionizing region was reduced from 5 to 2 cm. This was done because we had difficulties in extracting all ions that are formed along the total length of 5 cm. The grid-anode separation increases from 2.90 mm at the entrance to 3.15 mm at the exit.
- The entrance slit is a small circular hole, 0.4 mm in diameter, in order to meet the requirements of angular resolution.
- As a cathode is used one 2 mm wide ribbon instead of three 1 mm wide ribbons; the slot in the grid sheet is also 2 mm wide (was 4 mm). In this way the volume of the ionizing region for background molecules is reduced and by that the signal to noise ratio for the employed narrow beams is improved.
- The cathode is not made of thoriated but of pure tungsten, because at the high temperatures required for the activation of the thorium the wires of the neighbouring grid were often damaged. These 0.05 mm thick molybdenum wires have been spot welded across the slot in the grid sheet with separations of 0.5 mm. The grid sheet itself was made of tantalum to ensure a good heat transport from the middle to the edges.

The cathode and plate sheets were made of stainless steel with water-cooling leads brased onto them. The spacers separating the sheets and the rollers supporting the cathode were made of sapphire. The entrance and exit grids consist of a few 0.025 mm thick tungsten wires. The electrostatic lens sytem is a set of 4 cylindrical tubes, 3 mm in diameter, without grids.

- The watercooling leads supporting the ionizer are fed through a vertically mounted quartz disk, which also contains the circular entrance hole for the primary beam and a number of small holes for all the electrical connections. Because the ionizer is not separately pumped, its background pressure equals the pressure in the main chamber.

#### *b. Performance of the Ionizer*

Before operation the ionizer is outgassed. This is performed by first emptying the water leads and then heating the cathode with a current of 10.5 A at 3.2 V while there is no water cooling. All parts of the ionizer reach a temperature of at least 400°C in this way. During operation the water cooling is on and an electric current of about 12 A at 6 V through the cathode is required to obtain an electron current of 40 mA in the ionizing region between grid and plate. A feedback system stabilizes this electron current by adjusting the current through the cathode. Under these circumstances the temperature of the grid sheet becomes 280°C. The applied voltages are:

cathode	: +1000 V
grid	: +1085 V
plate	: +1085 V
entrance grid	: +1080 V
exit grid	: +1040 V

The magnitude of the ion output is not very sensitive to the voltage on the entrance grid, but more so to that of the exit grid. We also found that it is very important to have the exist grid positioned exactly at the end of the grid slot and not further back.

We have determined the efficiency of our detector by collecting the ions right behind the ionizer. By admitting a partial pressure of  $2.3 \times 10^{-7}$  torr of nitrogen the ion current was increased by  $2.8 \times 10^{-8}$  A,



which implies an efficiency of  $0.13 \text{ A torr}^{-1}$ . This is more than a factor 2.5 better than the result of Weiss:  $0.25 \text{ A torr}^{-1}$  for argon while the volume of his ionization region is 5 times larger. Next we made an effusive  $\text{N}_2$  beam at room temperature of  $1.2 \times 10^{16}$  molecules  $\text{sr}^{-1}\text{s}^{-1}$ , giving rise to  $3.5 \times 10^{10}$  molecules  $\text{s}^{-1}$  entering the detector (this time the diameter of the slit was 1.5 mm). We found an ion yield of  $2.8 \times 10^8$  ions per second. This means that 1 in every 120 beam particles is ionized, which is an extremely high efficiency. The efficiency Weiss found for argon is 1 in 250 (the number 1 in 40 mentioned in his publication is a factor  $2\pi$  erroneous), while his ionization region is a factor 2.5 longer. Taking into account the different velocities and ionization cross sections of Ar and  $\text{N}_2$  our result is about a factor 4 better and it also agrees rather good with the expected ionization cross section of about  $2.5 \times 10^{-16} \text{ cm}^2$ . By comparing the ion currents that we observed for the background gas and for the beam, we found a factor 5 for the ratio of the total ionization volume to the ionization volume covered by the beam. The actual value of this geometric factor is 3.8. The agreement is satisfactory in view of the uncertainties of the various quantities involved in this comparison.

### *c. Mass Separation and Amplification*

After leaving the ionizer the ions go through a set of cylindrical tubes, the voltages of which are adjusted to yield a parallel ion beam entering the mass spectrometer entrance slit ( $1 \times 3 \text{ mm}^2$ ), which is at ground potential. The electromagnet used for the mass separation is single focussing and has a sector field of  $45^\circ$  with a radius of 100 mm. The gap between the poles is 3 mm. Before entering the magnetic field, the ion beam passes two deflection plates in order to be directed onto the mass spectrometer exit slit ( $1 \times 3 \text{ mm}^2$ ). The resolution of the mass spectrometer is 30, with the half width at half height of the peaks as a criterium. The transmission is about 15%. Behind the mass spectrometer is a particle multiplier (Bendix, model 310B), which is normally used at the maximum allowed d.c. output current, yielding in our case an amplification of about 400.

The signal-to-noise ratio we finally obtain with the above described detection system is about  $10^5$  for a room temperature supersonic  $N_2$  beam with an intensity of  $5 \times 10^{11}$  molecules  $s^{-1}$  entering the ionizer, when the integration time of the lock-in amplifier is 30 seconds. For Ar beams about the same signal-to-noise ratio is obtained.

## 9. MEASURING PROCEDURE

According to Eq. 1.3 the total collision cross section  $Q$  can be determined by measuring the attenuation of a beam by a scattering gas. For that purpose first the unattenuated intensity  $I_0$  of the velocity selected beam is recorded during four minutes. Then the scattering gas is admitted and the attenuated intensity  $I$  is observed during four minutes. Next the scattering gas is pumped away and the procedure is repeated once or twice depending on the quality of the signal. The cycle for one velocity is then completed by checking the zero point of the recorder. The time constant of the lock-in-amplifier is 10 or 30 seconds. The attenuation of the beam amounts to 40% at the most.

A complete run for one system covering the entire velocity range from 500 to 4300  $m s^{-1}$  requires a continuous measuring period of about 48 hours.

## CHAPTER III

## DATA REDUCTION

## 1. INTRODUCTION

For a beam velocity  $v_1$  the measured ratio  $I/I_0$  together with the simultaneously measured scattering gas pressure  $p_{SG}$  yields a relative value for the experimental cross section  $Q_{exp}$

$$Q_{exp} \sim p_{SG}^{-1} \ln(I/I_0) \quad 3.1$$

Due to the finite angular resolution of the apparatus and to the motion of the scattering gas atoms,  $Q_{exp}$  is not equal to the true cross section  $Q(v_1)$ , which would be measured in an idealized situation. In order to arrive at a proper evaluation of  $Q_{exp}$  measured in the real situation, we consider again the attenuation of the beam  $dI$  by an element of length  $d\ell$  of the scattering region. In the ideal case  $dI$  can be written as (Eq. 1.2):

$$dI = -2\pi n(\ell) I(\ell) d\ell \int_0^\pi \sigma(\theta) \sin \theta d\theta$$

The finite angular resolution and the motion of the scattering gas can be taken into account after introducing two probability distributions  $W(\theta)$  and  $P(g)$ . The angular resolution function  $W(\theta)$  gives the probability that a particle scattered over an angle  $\theta$  in the LAB-system is still detected, while  $P(g)$  is the probability for a relative velocity  $g$  of two colliding particles. In this way we obtain:

$$dI = -2\pi n(\ell) I(\ell) d\ell \int_0^\infty \int_0^\pi \{1 - W(\theta)\} P(g) \sigma(\theta, g) \sin \theta d\theta dg, \quad 3.2$$

with  $\sigma(\theta, g)$  being the velocity dependent differential cross section. The functions  $W(\theta)$  and  $P(g)$  are taken to be independent of the coordinate  $\ell$ , but this is in general not true. However, the simplification is justified under the usual experimental conditions. We will return to this point later. When  $W(\theta)$  and  $P(g)$  are indeed independent of  $\ell$ , the integration

over the scattering region yields:

$$\ln(I/I_0) = - \int n(\lambda) d\lambda \cdot 2\pi \int_0^{\infty} \int_0^{\pi} \{1 - W(\theta)\} P(g) \sigma(\theta, g) \sin \theta d\theta dg . \quad 3.3$$

From Eq. 3.3 now follows for the experimental cross section:

$$Q_{\text{exp}} = 2\pi \int_0^{\infty} \int_0^{\pi} \{1 - W(\theta)\} P(g) \sigma(\theta, g) \sin \theta d\theta dg . \quad 3.4$$

Strictly speaking  $Q_{\text{exp}}$  as given by Eq. 3.4 is no longer a total cross section. Through the factor  $1 - W(\theta)$  in the integrand, which is zero at very small angles, part of the total cross section is lacking. One should therefore rather say that experimentally an "incomplete" cross section is determined. Through the factor  $P(g)$  the experimental cross section is moreover an average over a finite velocity range.

Eq. 3.4 also reveals that the problem of interpreting the information contained in the experimental data in terms of the interaction potential is in general quite complicated. In order to verify whether a given potential is consistent with the experimental results,  $Q_{\text{exp}}$  must be calculated according to Eq. 3.4 and the result of this calculation should be compared with the experimental data. This implies that for every trial potential, the differential cross section as a function of energy has to be numerically calculated. The procedure to arrive at the potential which yields the best fit to the experimental data is therefore very elaborate. Such a rigorous analysis is beyond the scope of this thesis, but will be performed at a later time.

For a provisional analysis of our data we will treat the experimental cross sections as experimental *total* cross sections and apply corrections for the angular resolution and the velocity spread. For this purpose we rewrite Eq. 3.4 by using the definition

$$Q(g) = 2\pi \int_0^{\pi} \sigma(\theta, g) \sin \theta d\theta \quad 3.5$$

and by introducing the angular resolution correction  $\Delta Q(g)$ :

$$\Delta Q(g) = 2\pi \int_0^{\pi} W(\theta) \sigma(\theta, g) \sin \theta d\theta . \quad 3.6$$

This yields for the experimental cross section:



$$Q_{\text{exp}} = \int_0^{\infty} \{ Q(g) - \Delta Q(g) \} P(g) dg . \quad 3.7$$

Subsequently we define the effective total cross section  $Q_{\text{eff}}$  as

$$Q_{\text{eff}} = \int_0^{\infty} Q(g) P(g) dg \quad 3.8$$

and the effective angular resolution correction  $\Delta Q_{\text{eff}}$  as

$$\Delta Q_{\text{eff}} = \int_0^{\infty} \Delta Q(g) P(g) dg , \quad 3.9$$

so that  $Q_{\text{exp}}$  may be written:

$$Q_{\text{exp}} = Q_{\text{eff}} - \Delta Q_{\text{eff}} . \quad 3.10$$

As will be shown in the next sections of this Chapter, the effective angular resolution correction  $\Delta Q_{\text{eff}}$  can be determined in an approximate way starting from the experimental data. If this correction is applied to the data according to Eq. 3.10, the value of  $Q_{\text{eff}}$  is obtained. Since a rigorous deconvolution of  $Q_{\text{eff}}$  to obtain  $Q(g)$  from Eq. 3.8 is impossible, an approximate correction for the velocity spread is applied yielding corrected cross sections  $Q_{\text{corr}}(\bar{g})$  from which the positions of the glory extrema can be accurately determined. These extrema positions will subsequently be used as a test on the validity of a number of proposed potentials (Chapter IV).

Although the angular resolution correction is applied prior to the velocity spread correction, we will for convenience of presentation discuss the latter first.

## 2. VELOCITY SPREAD CORRECTION

### a. The Velocity Distribution $P(g)$

Two different scattering arrangements have been used in our experiments.

In the first arrangement the primary beam particles of approximately uniform velocity  $v_1$  pass the region in front of the ideal slit (Chapter II par. 7d), from which the scattering gas effuses with a cosine

angular distribution and a Maxwellian velocity distribution. In this case the conditions are clearly non-uniform over the beam path. It has been pointed out by Berkling et al. [BER 62], however, that the effective cross section obtained in this situation is identical to the effective cross section obtained with a primary beam passing through a scattering chamber with a homogeneous gas density. For a scattering chamber the distribution of relative velocities  $P(g)$  is given by:

$$P(g) \sim g^2 v_1^{-2} [\exp \{ -(g-v_1)^2 v_1^2 x^{-2} \} - \exp \{ -(g+v_1)^2 v_1^2 x^2 \}] \quad 3.11$$

where  $x = v_1/v_{2m}$ , with  $v_{2m}$  the most probable velocity of the scattering gas particles. The average relative velocity  $\bar{g}$  and the most probable relative velocity  $g_m$  are:

$$\bar{g} = v_1 \left( 1 + \frac{2}{2x^2 + 1} \right) \quad 3.12$$

$$g_m \approx v_1 \frac{1 + (1 + 4/x^2)^{1/2}}{2} \quad 3.13$$

An example of this distribution is shown in Fig. 3.1. For this example the most unfavourable conditions in our experiments have been chosen, i.e. an argon beam with  $v_1 = 540 \text{ m s}^{-1}$  scattered by argon gas at a temperature of 80 K ( $v_{2m} = 180 \text{ m s}^{-1}$ ), so that  $x = 3$ .

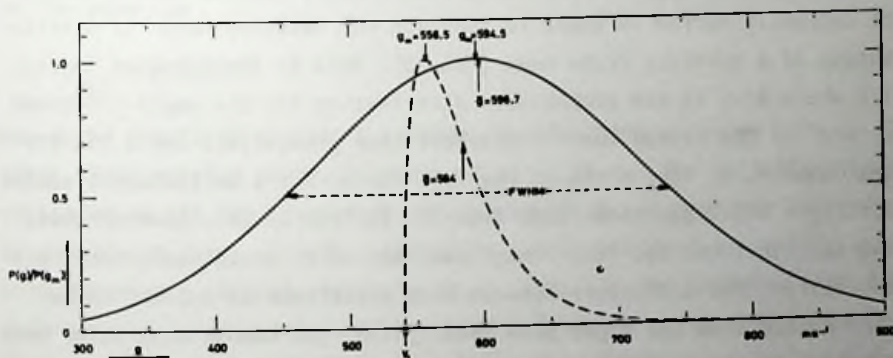


Fig. 3.1 The normalized distribution  $P(g)/P(g_m)$  of relative velocities.  $g_m$  is the most probable velocity,  $\bar{g}$  the average velocity, FWHM the full width at half maximum. The solid curve is for a scattering chamber, the dashed curve for parallel cross beam.

In the second scattering arrangement the primary beam passes the region in front of a multi channel source (Chapter II par. 7e) from which the scattering gas effuses with a narrow angular distribution and a Maxwellian velocity distribution. Since here the length of the scattering region is large compared to the channel diameter and to the primary beam dimensions, the conditions of the scattering gas may be considered to be homogeneous over the scattering length. The multi channel source produced a cross beam with an angular spread of  $\delta_{\frac{1}{2}} = 4^\circ$ . At first sight one expects from this source a distribution of relative velocities close to that for a cross beam with zero angular spread and a Maxwellian velocity distribution, which is given by

$$P(g) \sim g^2 v_1^{-1} (g^2 - v_1^2)^{\frac{1}{2}} \exp -(g^2 - v_1^2) v_1^{-2} x^2 \quad 3.14$$

$$\bar{g} = v_1 \left( 1 + \frac{24x^2 + 15}{32x^4 + 24x^2 - 15} \right) \quad 3.15$$

$$g_m = v_1 \left( \frac{x^2 + 3/2 + (x^4 - x^2 + 9/4)^{\frac{1}{2}}}{2x^2} \right)^{\frac{1}{2}} \quad 3.16$$

The difference between the distributions of Eq. 3.11 and Eq. 3.14 are apparent from the examples in Fig. 3.1. Feltgen shows that the angular distribution of particles effusing from a multi channel source should be extremely narrow in order to approach the relative-velocity distribution of a parallel cross beam [FEL 70]. This is demonstrated by Fig. 3.2 where  $R(\alpha)$  is the probability distribution for the angle  $\alpha$  between  $\vec{v}_1$  and  $\vec{v}_2$ . The dashed curve represents this probability for a scattering chamber, so  $R(\alpha) \sim \sin \alpha$ . The full curve, for a multichannel source with  $\delta_{\frac{1}{2}} = 0.51^\circ$  has been taken from FEL 70. For a comparison of these two distributions the curves have been scaled to yield equal total probabilities. The difference between both distributions appears to be less marked than one might have anticipated: the common area under both curves amounts to 80% of the total area under one curve. This implies that for our source - with the much larger value of  $\delta_{\frac{1}{2}} = 4^\circ$  - the distribution  $R(\alpha)$  is even nearer to  $\sin \alpha$  and consequently  $P(g)$  more nearly equal to the distribution function for a scattering chamber. An advan-

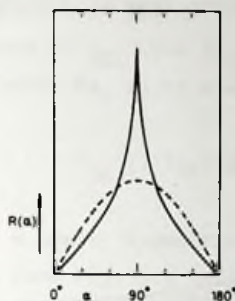


Fig. 3.2 The probability distribution  $R(\alpha)$  for the angle  $\alpha$  between  $\vec{v}_2$  and the primary beam velocity  $\vec{v}_1$ . The dashed curve holds for a scattering chamber, the full curve for a multi channel source with  $\delta_2 = 0.51^\circ$ .

tage of the distribution for a scattering chamber over that for a parallel cross beam is that it is nearly symmetric around  $\bar{g}$ .

#### b. The Berkling Factor

The effective cross section corresponding to a beam velocity  $v_1$  is given by Eq. 3.8:

$$Q_{\text{eff}} = \int_0^{\infty} P(g) Q(g) dg .$$

Following Berkling et al. [BER 62] we now define the quantity  $F$  according to the equation

$$Q_{\text{eff}} = F Q(v_1) . \quad 3.17$$

Hence the "Berkling factor"  $F$  relates the effective cross section to the total cross section at the "reference" velocity  $v_1$ . The factor  $F$  depends of course on all the parameters determining  $P(g)$  and  $Q(g)$  and can only be calculated for a specific scattering arrangement and a specific velocity dependence of  $Q(g)$ . Berkling et al. [BER 62] and Toennies [PAU 65] made numerical calculations of  $F$  starting from the attractive potential  $V(r) = -C_s/r^s$ , for which  $Q(g) \sim g^{-2/(s-1)}$ . They denoted the factor  $F$  for a scattering chamber by  $Fa_0$  and for a cross parallel beam by  $Fb_0$ . In Fig. 3.3 the Berkling factors  $Fa_0$  and  $Fb_0$  are shown as a function of  $x = v_1/v_{2m}$  for  $s = 6$ . At  $x = 3$ , the most unfavourable value of  $x$  occur-



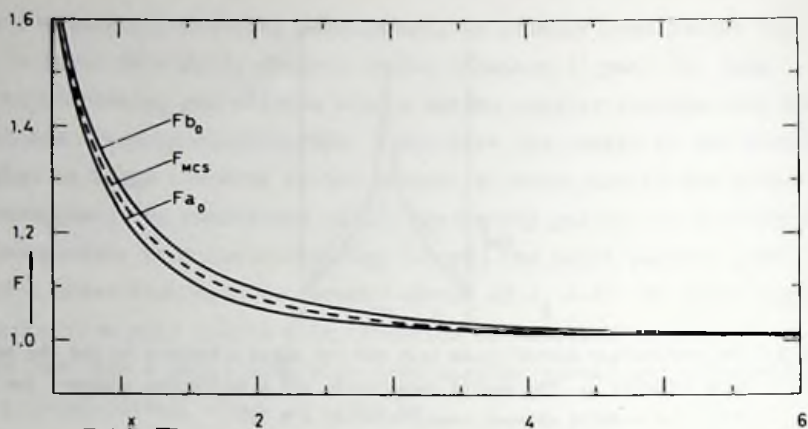


Fig. 3.3 The Berkling factor  $F$  for  $s = 6$  as a function of  $x = v_1/v_2$ .  $F_{a_0}$  holds for a scattering chamber,  $F_{b_0}$  for a parallel cross beam,  $F_{MCS}$  for a multi channel source with  $\delta_{\frac{1}{2}} = 0.24^\circ$ .

ring in our experiments,  $F_{a_0}$  is 1.027 and  $F_{b_0}$  is 1.046. Fig. 3.3 also shows the Berkling factor  $F_{MCS}$  for a multi channel source with  $\delta_{\frac{1}{2}} = 0.24^\circ$ , calculated by Ragas [RAG 72] for  $s = 6$ . Although  $\delta_{\frac{1}{2}}$  has a very small value in this case,  $F_{MCS}$  is closer to  $F_{a_0}$  than to  $F_{b_0}$  ( $F_{MCS} = 1.035$  at  $x = 3$ ). This is again in agreement with the earlier findings on the distribution functions for the multi channel source and the scattering chamber and we may therefore conclude that for both scattering arrangements used in our experiments the Berkling factor  $F_{a_0}$  applies.

#### *6. Damping and Position of the Glories*

The foregoing discussion only applies for the potential  $V(r) = -C_5/r^5$  for which  $Q(g) \sim g^{-2/(s-1)}$ . For a realistic potential, also containing a repulsive term, glory undulations will be present. According to Eqs. 1.19 and 1.20 we then have:

$$Q(g) = Q_{LL}(g) + Q_{GL}(g) = Q_{LL}(g) + A_{GL}(g) \cos(2\eta_0 + 3\pi/4) \quad 3.18$$

where  $Q_{LL}(g) \sim g^{-2/(s-1)}$ . The effective total cross section is now:

$$Q_{\text{eff}} = \int_0^{\infty} Q_{LL}(g) P(g) dg + \int_0^{\infty} Q_{GL}(g) P(g) dg \quad 3.18a$$

Unfortunately a deconvolution of the second term is not possible due to the complicated dependence of  $Q_{GL}$  upon  $g$ . The first term can be reduced by using the Berkling factor  $Fa_o(s, x)$  yielding

$$Q_{eff} = Fa_o Q_{LL}(v_1) + \int_0^{\infty} Q_{GL}(g) P(g) dg . \quad 3.18b$$

Since, however,  $P(g)$  is a nearly symmetric distribution around the average relative velocity  $\bar{g}$  (see Fig. 3.1 full curve), it is preferable to choose  $\bar{g}$  as the reference velocity instead of  $v_1$ . This is easily realized in the first term because  $Q_{LL}(v_1) \sim v_1^{-2/(s-1)}$  and thus

$$Q_{eff}(\bar{g}) = Fa_o (\bar{g}/v_1)^{2/(s-1)} Q_{LL}(\bar{g}) + \int_0^{\infty} Q_{GL}(g) P(g) dg . \quad 3.18c$$

The factor  $Fa_o (\bar{g}/v_1)^{2/(s-1)}$  may be looked upon as a Berkling factor for  $Q_{LL}$  with respect to the reference velocity  $\bar{g}$ . If we now apply this Berkling factor to the complete  $Q_{eff}(\bar{g})$ , a corrected cross section  $Q_{corr}(\bar{g})$  is obtained given by

$$\begin{aligned} Q_{corr}(\bar{g}) &= Q_{eff}(\bar{g}) \{Fa_o (\bar{g}/v_1)^{2/(s-1)}\}^{-1} \\ &= Q_{LL}(\bar{g}) + \left\{ \int_0^{\infty} Q_{GL}(g) P(g) dg \right\} \{Fa_o (\bar{g}/v_1)^{2/(s-1)}\}^{-1} \end{aligned} \quad 3.19$$

From Eq. 3.19 it is clear that in  $Q_{corr}(\bar{g})$  the "average" total cross section  $Q_{LL}(\bar{g})$  is properly represented but the glory undulations are damped through the velocity distribution  $P(g)$  and through the Berkling factor. Due to the damping caused by  $P(g)$  the true glory amplitudes cannot be determined from  $Q_{corr}(\bar{g})$ , but the glory extrema still appear at the velocities where they would be observed with an infinitely narrow velocity spread. This becomes plausible when it is realized that  $P(g)$  is nearly symmetric around  $\bar{g}$  and  $Q_{GL}(g)$  is practically symmetric around an extremum velocity, within the velocity range covered by the width of  $P(g)$ . Moreover the very weak dependence of the Berkling factor upon  $\bar{g}$  has a negligible influence on the extrema positions. Therefore the positions of the glory extrema can accurately be derived from  $Q_{corr}(\bar{g})$ .

On the basis of the foregoing considerations we will give the numerical results of our measurements in the form of corrected cross sections  $Q_{\text{corr}}(\bar{g})$  as a function of  $\bar{g}$ , calculated according to Eq. 3.19. Since from our measurements only relative numbers for the total cross section can be obtained, we used the results of J.E. Scott Jr. and coworkers [SWE 70, PHI 71] to transform our data into absolute values (see par. 4a of this Chapter).

For a graphical representation of the glory structure one preferably tries to compensate for the velocity dependence of  $Q_{\text{LL}}$ . This is largely achieved by plotting the quantity  $Q_{\text{corr}} \cdot \bar{g}^{2/5}$  as a function of  $\bar{g}$ , since for the attractive part of the potential  $s = 6$  is a good approximation yielding  $Q_{\text{LL}} \sim (\bar{g})^{-2/5}$ . It should be realized, however, that the extrema positions in such a graph are different from the true glory positions (see par. 4c of this Chapter).

In our set up, with the scattering gas effusing from a slit source, the damping of the glories can be serious. This becomes evident if one compares the FWHM of the distribution  $P(g)$  for Ar-Ar in Fig. 3.1 ( $296 \text{ m s}^{-1}$ ) with the "wavelength" of the glory undulations for Ar-Ar in Fig. 4.3 (about  $320 \text{ m s}^{-1}$  at the lowest velocities). Since the velocity distribution for the MCS is nearly equal to that for the slit source, it follows that the damping will practically be the same in both cases. A better resolution of the glory undulations could only be obtained by using a supersonic secondary beam.

### 3. ANGULAR RESOLUTION CORRECTION

Due to the finite angular resolution, the measured cross section  $Q_{\text{exp}}$  is according to Eq. 3.10 smaller than  $Q_{\text{eff}}$  by an amount  $\Delta Q_{\text{eff}}$ . For simplicity we will omit from now on the subscript in  $\Delta Q_{\text{eff}}$ . Combining Eqs. 3.6 and 3.9 we then have

$$\Delta Q = \int_0^{\infty} \int_0^{\pi} W(\theta) 2\pi \sigma(\theta, g) \sin \theta P(g) d\theta dg . \quad 3.20$$

Because the relative correction  $\Delta Q/Q_{\text{eff}}$  becomes rather large in some of our measurements, it is necessary to calculate  $\Delta Q$  very precisely. This

requires an accurate knowledge of the angular resolution function  $W(\theta)$  and the small angle differential cross section  $\sigma(\theta, g)$ .

a. *The Angular Resolution Function*

The angular resolution function  $W(\theta)$  is completely determined by the geometry of the beam defining elements. In Fig. 3.4 our configuration with circular slits has been depicted. To calculate  $W(\theta)$  it is convenient to transform from  $\theta$  to the corresponding displacement  $\rho$  of the scattered particle in the plane of the detector:  $\rho = \theta/\lambda_3$ . For the case that the centers of the three slits are in line  $W(\rho)$  is found to be [BUS 66]

$$W(\rho) = \left\{ \int_0^{\max(\rho, r_d)} i(r) r dr + \pi^{-1} \frac{\rho + r_d}{|\rho - r_d|} \int_{r_d}^{\rho + r_d} i(r) \arccos\left(\frac{r^2 + \rho^2 - r_d^2}{2\rho r}\right) r dr \right\} \cdot \left\{ \int_0^{r_d} i(r) r dr \right\}^{-1} \quad 3.22$$

where  $i(r)$  is the intensity distribution of the unscattered beam in the detector plane with  $r$  the distance from the center of the detector slit. This distribution is given by

$$i(r) = \frac{1}{\pi(r_s - r_k)^2} \left[ (r_s + r_k)^2 \arccos \frac{r^2 + r_s r_k}{r(r_s + r_k)} + (r_s - r_k)^2 \arccos \frac{r^2 - r_s r_k}{r(r_s - r_k)} + 2 \{ r^2 (r_s + r_k)^2 - (r^2 + r_s r_k)^2 \}^{\frac{1}{2}} \right] \quad 3.23$$

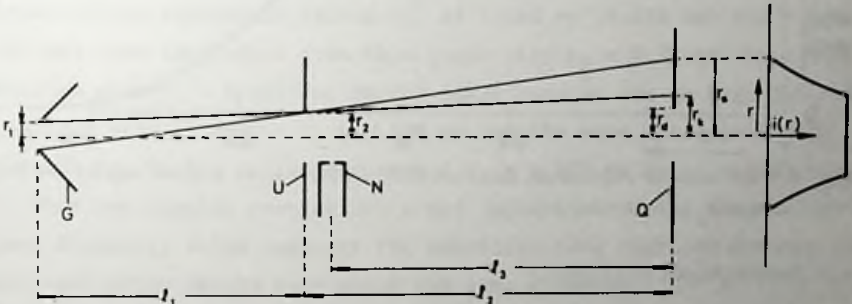


Fig. 3.4 Geometry of beam defining elements. G = skimmer, U = collimator, N = scattering gas source and Q = detector slit. At the right the distribution of unscattered beam particles in the detector plane  $i(r)$  as a function of the distance  $r$  from the center of the detector slit.





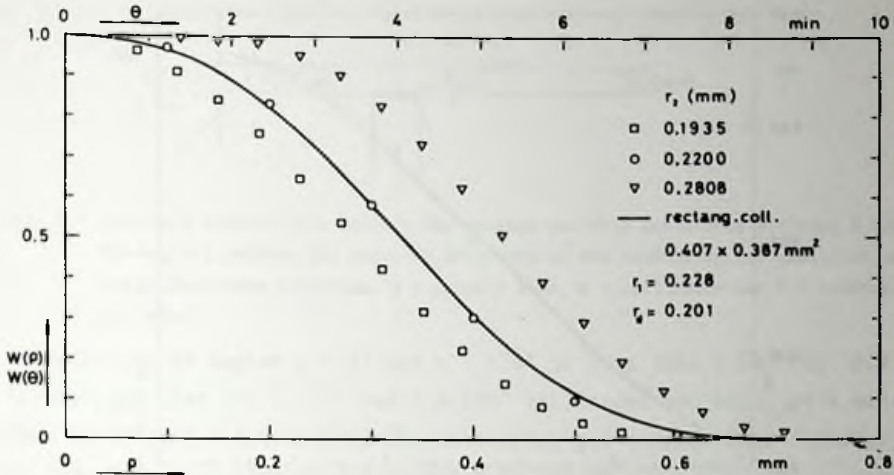


Fig. 3.6 The angular resolution function  $W(\rho) = W(\theta)$  for the configuration with the rectangular collimator (solid curve) and for three circular collimators of different radii  $r_2$ . In all cases  $r_1 = 0.228$  mm and  $r_d = 0.201$  mm.

radii and is depicted in Fig. 3.6. For comparison we also show the resolution functions for three circular collimators of different radii. The resolution function for the circular collimator with  $r_2 = 0.220$  mm can be seen to be nearly the same as that for the rectangular collimator. It is not surprising that the area of this circular collimator is approximately equal to that of the rectangle. In Fig. 3.7 we have plotted for a number of circular collimators the values of  $\rho_{\frac{1}{2}}$ , defined by  $W(\rho_{\frac{1}{2}}) = \frac{1}{2}$ , as a function of the collimator radius  $r_2$ , at fixed  $r_1$  (0.228 mm) and  $r_d$  (0.201 mm). One can deduce from this graph that  $\rho_{\frac{1}{2}} = 0.27$  mm for a configuration with  $r_2 = 0.185$  mm. On the other hand we see in Fig. 3.5, with the smaller skimmer radius  $r_1 = 0.107$  mm and the same detector radius  $r_d = 0.201$  mm, that a collimator radius  $r_2 = 0.185$  mm again yields  $\rho_{\frac{1}{2}} = 0.27$ . Thus the angular resolution is not improved by using the smaller skimmer diameter, which supports the intuitive idea that for optimum conditions all slits should have about the same diameter.

### a.3 Scattering Length

Strictly speaking Eq. 3.22 for  $W(\rho)$  only holds in the hypothetical case of zero scattering length. Only then can the initial unscattered

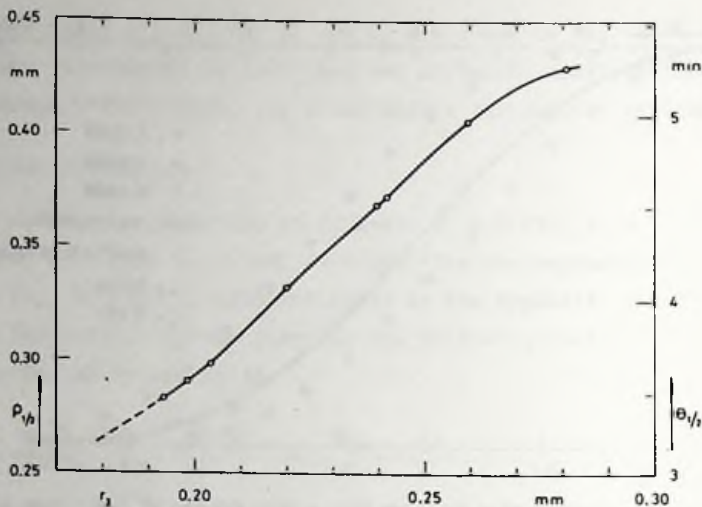


Fig. 3.7 The value of  $\rho_{1/2}$ , defined by  $W(\rho_{1/2}) = \frac{1}{2}$ , and of the corresponding  $\theta_{1/2}$ , as a function of  $r_2$ , the radius of the collimator.  $r_1 = 0.228$  mm and  $r_d = 0.201$  mm.

beam distribution  $i(r)$  of Eq. 3.23 be used in the calculation of  $W(\rho)$ . For a finite scattering length, however, in the contribution of an element  $d\ell$  to the attenuation,  $W(\rho)$  is not determined by the initial unscattered beam distribution  $i(r)$ , but by a local  $i(r)_\ell$ . This is the distribution of particles prevailing in the detector plane if behind the element  $d\ell$  no further scattering occurs. Thus  $i(r)_\ell$  contains not only the unscattered particles, but also the particles that have been scattered in the region before the element  $d\ell$ . By using the initial distribution  $i(r)$  throughout the whole scattering length, the effect of multiple scattering and of the scattering gas density variation over a cross cut of the primary beam is neglected.

Another result of the finite scattering length is that scattering occurs at different distances from the detector. Use of Eq. 3.22 for  $W(\rho)$ , however, is still permitted if the extent of the scattering region in the beam direction is smaller than  $\frac{1}{2} \ell_3$  [BUS 66]. To show that this condition is satisfied in spite of the seemingly large scattering region, we return to Fig. 3.3, where  $R(\alpha)$  is the probability distribution for the angle  $\alpha$  between the velocity vector of the scatterer and that of the primary beam particle. In the worst case, when  $R(\alpha) = \sin \alpha$ , the

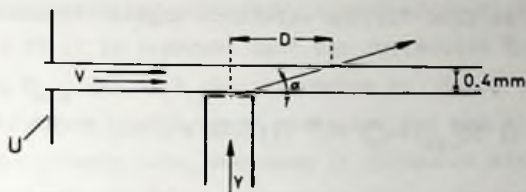


Fig. 3.8 Geometric relationship between the maximum possible scattering distance  $D$  and the angle  $\alpha$  between the velocity direction of the scattering gas particles and the primary beam direction.  $V$  = primary beam,  $U$  = collimator and  $Y$  = scattering gas inlet.

contribution of angles  $\alpha < 5^\circ$  and  $\alpha > 175^\circ$  is less than 1.5%. Fig. 3.8 illustrates that for  $\alpha = 5^\circ$  and  $\alpha = 175^\circ$  collisions may occur at a maximum distance  $D = 4.8$  mm from the scattering gas source. This distance is indeed much smaller than  $\frac{1}{2} \lambda_3$  which is 140 mm.

#### b. Small Angle Differential Cross Section

The small angle differential cross section is mainly determined by the attractive part of the potential. For a potential of the type  $V(r) = -C_5/r^5$  Helbing and Pauly [HEL 64] and Mason et al. [MAS 64] derived an expression for the small angle differential cross section which was modified by Von Busch et al. [BUS 67] to yield a slightly different and more accurate expression:

$$\sigma(\theta)_{\text{attr}} = [(k^2 Q^2)/(16\pi^2)] [1 + \text{tg}^2 \{\pi/(s-1)\}] \exp \{-0.7(\theta/\theta^*)^2\} \quad 3.24$$

Here  $\theta$  is the deflection angle in the CM system and  $k = \mu g/\hbar$ , while

$$(\theta^*)^{-2} = f(s) Q k^2/(8\pi) \quad 3.25$$

with

$$f(s) = [\Gamma\{2/(s-1)\}]^2 [2\pi \Gamma\{4/(s-1)\}]^{-1} [\text{tg} \{2\pi/(s-1)\}] . \quad 3.26$$

On account of total cross section calculations for realistic noble gas potentials, which are described in the next Chapter, we will use for the exponent of the attractive part of the potential  $s = 6.7$  (see par. 4b of this Chapter). The factors in the expressions given by Von Busch [BUS 66] are changed slightly by this and after transforming



to the LAB-system we find for the effective angular resolution correction:

$$\Delta Q = \int W(\theta) \left( .175/\pi \right) \left( Q_{\text{eff}}^2 / F a_0^2 \right) k_1^2 \left( 1 + 0.56/x^2 \right) \exp \left\{ -0.7 (\theta/\theta^*)^2 \right\} \theta \, d\theta \quad 3.27$$

where

$$(\theta^*)^{-2} = \left( .193/\pi \right) \left( Q_{\text{eff}} / F a_0 \right) k_1^2 \left( 1 + 0.40/x^2 \right) . \quad 3.28$$

Here  $\sin \theta$  has been replaced by  $\theta$  and  $k_1 = m_1 v_1 / \hbar$  is the wavenumber of the primary beam particles.

Before calculating the correction we first discuss the validity range of Eq. 3.24 for the small angle differential cross section. This validity range extends up to the critical angle

$$\theta_c = \left\{ \pi \hbar / (\mu g) \right\}^{1/2} \quad 3.29$$

beyond which angle the classical expression for the differential cross section holds [MAS 34, SMI 65]. Let us now for example consider one of our worst cases: Kr-Kr at  $4000 \text{ m s}^{-1}$ . The value of the critical angle in the LAB-system ( $\theta_c$ ) becomes in this case  $11 \times 10^{-4}$  radians. At the angle  $\theta = \theta_c$  the resolution function  $W(\theta)$  [ $\equiv W(\rho)$ ] has not attained zero but has the value 0.38 (see Fig. 3.5 for  $\rho = 0.31$ ). The quantity  $\sigma(\theta) \sin \theta$ , however, is at this angle only 20% of its maximum value and decreases rapidly. Hence the contribution to  $\Delta Q$  from angles  $\theta > \theta_c$  is relatively small. Therefore only a small error in  $\Delta Q$  results if for angles  $\theta > \theta_c$  we continue to use Eq. 3.24.

The way in which we apply the angular resolution correction to our data is as follows. First the relative values of our measured total cross sections are transformed into absolute values (see par. 4a of this Chapter). Next the correction  $\Delta Q$  according to Eq. 3.27 should be calculated. In this calculation, however, the unknown value of  $Q_{\text{eff}}$  is required. Therefore we proceed in an iterative manner: the calculation is started by first inserting in Eq. 3.27 the measured  $Q_{\text{exp}}$  instead of the unknown  $Q_{\text{eff}}$ . The first obtained approximation of  $Q_{\text{eff}}$  is used in the next iteration step and after at the most 6 iterations, the desired accuracy is attained. On the resulting value of  $Q_{\text{eff}}$  the velocity spread

correction of the preceding paragraph is applied to yield  $Q_{\text{corr}}$ .

From Eq. 3.27 it is apparent that the correction  $Q/Q_{\text{eff}}$  increases with increasing  $Q_{\text{eff}}$  and with the wavenumber  $k_1$ . Hence the correction is largest for systems with a large cross section and with the heavier atom used in the primary beam. Moreover it increases with increasing velocity. The magnitude of  $\Delta Q/Q_{\text{eff}}$  increases for Ar-Ar scattering from 1.2% at the lowest velocity to 24% at the highest velocity, for Ar-Kr from 1.7% to 29%, for Ar-Xe from 1.5% to 33%, for Kr-Ar from 7% to 52%, for Kr-Kr from 7.7% to 55%, for Kr-Xe from 8.5% to 56%.

### c. Shift of the Glory Extrema

In the previous paragraph the angular resolution correction  $\Delta Q$  was calculated assuming a purely attractive potential of the form  $V = -C_s/r^5$ . For a realistic potential with an attractive and a repulsive branch, the expression for the small angle differential cross section given in Eq. 3.24 should be modified. Assuming that for small angles the contribution to the scattering amplitude  $f(\theta)$  due to the repulsive part of the potential has the same angular dependence as the contribution due to the attractive part, Helbing derived the following expression for the small angle differential cross section [HEL 66]:<sup>†</sup>

$$\begin{aligned} \sigma(\theta)^* = \sigma(\theta)_{\text{attr}} [1 + 2(A_{\text{GL}}/Q_{\text{LL}}) \cos \{\pi/(s-1)\} \cos \{2\eta_0 + (3\pi/4) + \pi/(s-1)\} + \\ + (A_{\text{GL}}/Q_{\text{LL}})^2 \cos^2 \{\pi/(s-1)\}] . \end{aligned} \quad 3.30$$

The quadratic term in the brackets can generally be neglected. The second term represents glory undulations as a function of the energy, quite similar to the glory undulations in the total cross section [BUC 68]. The undulations in the differential and in the total cross section, however, have a phase difference  $\pi/(s-1)$  and differ in amplitude by a factor  $2 \cos \{\pi/(s-1)\}$ . This can be seen by comparing Eq. 3.30 and Eq. 1.20.

The angular resolution correction  $(\Delta Q)^*$  which also accounts for

<sup>†</sup> Eq. 3.30 was also mentioned by Muller [MUL 67], however, with a sign error in the third term of the argument of the second cos in Eq. 3.30. For the same reason an error appears in Eq. (4) of a paper by Helbing et al. [HEL 68].

this undulatory behaviour of the differential cross section now becomes

$$\{\Delta Q\}^* = \Delta Q [1 + 2(A_{GL}/Q_{LL}) \cos\{\pi(s-1)\} \cos\{2\eta_0 + (3\pi/4) + \pi(s-1)\}] \quad 3.31$$

For our case  $s = 6.7$ , and Eq. 3.31 becomes

$$\{\Delta Q\}^* = \Delta Q [1 + 1.70 (A_{GL}/Q_{LL}) \cos (2\eta_0 + 0.92\pi)] . \quad 3.32$$

From this equation it is clear that the correction  $\{\Delta Q\}^*$  shows undulations as a function of the energy, which are not in phase with the glory undulations in the total cross section. Consequently in the measured cross sections the extrema are shifted in position with respect to the true extremum velocities of the glories, and they will remain shifted when only the angular resolution correction  $\Delta Q$  is applied. The correction  $\{\Delta Q\}^*$ , however, cannot be applied by starting simply from the measured cross sections, because the true glory amplitude  $A_{GL}$  and the value of  $\eta_0$  cannot be derived from the measurements. We therefore had to estimate the magnitude of this shift and the procedure requires starting from theoretically calculated cross sections. Let us illustrate this approach with the example of Kr-Kr scattering shown in Fig. 3.9. The full curve in this Figure represents the total cross section  $Q(g)$  as a function of the relative velocity  $g$ , calculated for the BB-potential which Barker proposes for Kr-Kr (see Chapter IV). The true positions of the glory extrema in this plot are denoted by  $g_{GL}$ . We also calculated the values of  $Q_{LL}$  (dotted curve) so that we were able to determine the correction  $\{\Delta Q\}^*(g)$  according to Eq. 3.32. By subtracting these  $\{\Delta Q\}^*(g)$  from  $Q(g)$  we obtained pseudo experimental cross sections  $Q'_{exp}(g) = Q(g) - \{\Delta Q\}^*(g)$ , which would be measured in our apparatus if  $Q(g)$  were the true total cross section. (For simplicity an infinitely narrow velocity distribution  $P(g)$  was assumed and in the Figs. 3.9 and 3.10 the primes denoting the pseudo quantities have been omitted). Next we treated these pseudo experimental data in the same way as our measured data. Thus we added the corresponding correction  $\{\Delta Q\}'$  of Eq. 3.27 to  $Q'_{exp}(g)$  yielding pseudo corrected cross sections  $Q'_{corr}(g) = Q'_{exp} + \{\Delta Q\}'$  (dashed curve). We see that the extrema of  $Q'_{corr}$  appear at velocities  $g'_m$ , which are lower than the velocities  $g_{GL}$  where the extrema of the calculated cross section

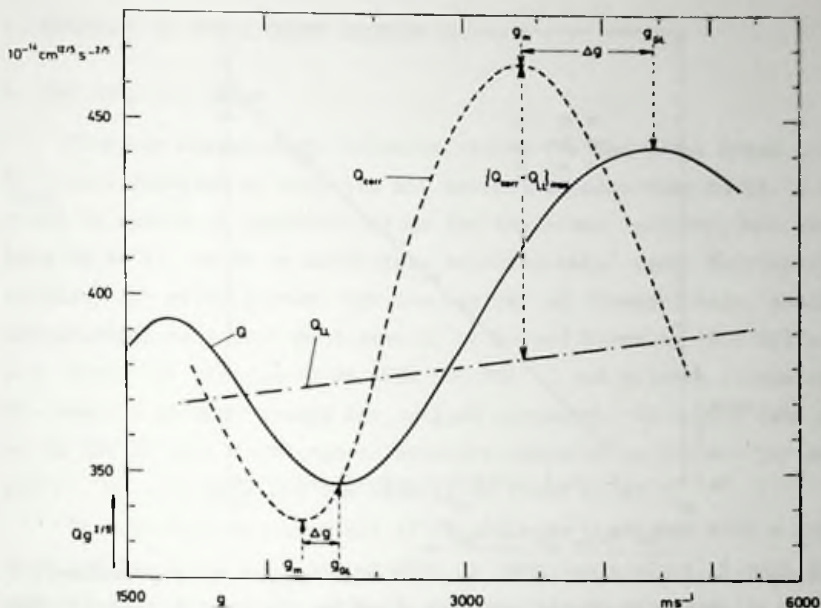


Fig. 3.9 Total cross section  $Q$  times  $g^{2/5}$  as a function of the relative velocity  $g$ . The full curve ( $Q$ ) was calculated for the BB-potential for Kr-Kr, the dash-dot line ( $Q_{LL}$ ) for only the attractive part of this potential. The dashed curve represents  $Q_{CORR} = Q - \{\Delta Q\}' + \Delta Q$  according to Eq. 3.32 and Eq. 3.27.

$Q$  occur. The extremum shift  $\{\Delta g\}' = g_{GL} - g_m'$  is expected to increase when the relative correction  $\{\Delta Q\}'/Q'_{CORR}$  and when the observed glory amplitude  $|Q'_{CORR} - Q_{LL}|_{max}$  increases. In order to get a quantitative picture of the dependence of  $\{\Delta g\}'$  on  $\{\Delta Q\}'/Q'_{CORR}$  and  $|Q'_{CORR} - Q_{LL}|_{max}$ , we determined the quantity  $\{\Delta g\}'/g_m'$  for a few maxima and minima of different systems and different potentials. The results are shown in Fig. 3.10 where the relative extremum shift  $\{\Delta g\}'/g_m'$  has been plotted as a function of the quantity  $\{|Q'_{CORR} - Q_{LL}|_{max}/Q_{LL}\} \{ \{\Delta Q\}'/Q'_{CORR} \}^2$ . In this way we obtain a representation which seems to be unique, so that for all measured extrema the shift can be estimated from this graph. When for instance for an extremum the relative glory amplitude  $|Q'_{CORR} - Q_{LL}|_{max}/Q_{LL}$  is 0.18 and the relative correction  $\Delta Q/Q_{CORR}$  is 0.50 then the extremum shift will be 26%. This is in fact the largest shift we had to apply. It is clear that we cannot claim a high accuracy for the resulting true extremum velocity  $\bar{g}_{GL}$  in this case, because our tentative procedure lacks sufficient theo-



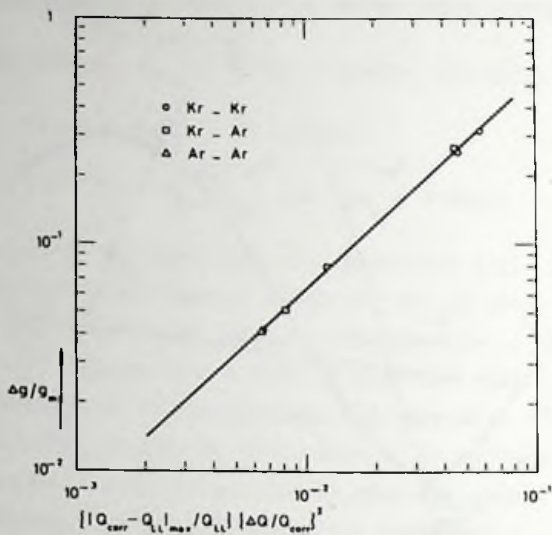


Fig. 3.10 Empirical relation between the relative shift  $\Delta g/g_m$  of the glory extrema due to the angular resolution correction  $\Delta Q$  and the quantity  $(|Q_{\text{corr}} - Q_{\text{LL}}|_{\text{max}} / Q_{\text{LL}})^2$ . For an explanation of the symbols see Fig. 3.9.

retical foundation. However, a check on the reliability of this method is obtained when the same system is measured with different angular resolutions. We can use for this purpose our measurements on Ar-Kr and Kr-Ar (see Chapter IV par. 2c), upon which a quite different angular resolution correction had to be applied due to the difference in kinematics. The shift of the first extremum is only 5.6% for Ar-Kr, but 25% for Kr-Ar. After adding these shifts to the two observed extremum velocities  $g_m$ , it is found that the values of the resulting corrected velocities  $g_{\text{GL}}$  differ by only 4.5%, which is within the estimated accuracy. While a more rigorous analysis of our data will be performed in the near future, we will for the moment confine ourselves to a determination of the measured velocity extrema  $g_m$ , correct these if necessary for the above mentioned shift  $\Delta g$  and compare the resulting  $g_{\text{GL}}$ 's with values calculated for various potentials.

#### 4. ANALYSIS OF TOTAL CROSS SECTION DATA

##### a. The Absolute Value

From our measurements relative values for the total cross section  $Q_{\text{exp}}$  as a function of velocity are determined according to Eq. 3.1. In order to arrive at absolute values for the cross sections, our results have to be fitted to an absolutely measured total cross section at one velocity for every system. For the systems of interest here, absolute measurements have been performed by Rothe and Neynaber [ROT 65] and by J.E. Scott Jr. and coworkers [SWE 70, PHI 71 and private communication]. The results of both groups are in good agreement. Since the data reported in SWE 70 show an increased accuracy compared to the earlier data of ROT 65, we will only use the results of Scott et al.

The absolute measurements of SWE 70 were performed with a supersonic beam and the scattering gas chamber at room temperature. Always the average relative velocity  $\bar{g}_{\text{abs}}$  is at the low side of our velocity range. Considering in our experiments, with the scattering gas at 80 K, that the glories are very strongly damped at low velocities (observed amplitude smaller than 2% of  $Q_{\text{LL}}$ ) it is evident that, in Scott's experiments, where the velocity spread is at least two times larger, the glory contribution is averaged out completely. The measured quantity in their experiments is therefore  $Q_{\text{LL}}$  at the velocity  $\bar{g}_{\text{abs}}$ . Our data are now fitted in such a way, that our final values for  $Q_{\text{corr}}(\bar{g})$  yield a  $Q_{\text{LL}}$  which at the velocity  $\bar{g}_{\text{abs}}$  equals the absolute  $Q_{\text{LL}}$  value of SWE 70.

The absolute cross section data may also be used as an additional test on the validity of various proposed potentials. From the graphs of  $Q g^{2/5}$  versus  $g$ , calculated for the potentials tested (see Chapter IV), theoretical values of  $Q_{\text{LL}} g^{2/5}$  at the velocity  $\bar{g}_{\text{abs}}$  are determined. These values are then compared with the experimental value of  $Q_{\text{LL}} \bar{g}_{\text{abs}}^{2/5}$  from SWE 70.

##### b. The Velocity Dependence of $Q_{\text{LL}}$

When the attractive branch of the potential can accurately be described by  $V(r) = -C_6/r^6$  over a wide enough range (about  $1.2 < r/r_m < 3$ ) then  $Q_{\text{LL}} \sim g^{-2/5}$  and hence  $Q_{\text{LL}} g^{2/5}$  is velocity independent. In that case

the true total cross section  $Q = Q_{LL} + Q_{GL}$  plotted as  $Q g^{2/5}$  as a function of  $g$  undulates about a horizontal line. In the Figs. 4.3, 4.5, 4.9 and 4.12, where calculated cross sections have been plotted, one can see that for all potentials,  $Q_{LL} g^{2/5}$  increases slightly with increasing velocity, instead of being constant. This behaviour is even more explicitly revealed in Fig. 3.9 in which, among others,  $Q_{LL} g^{2/5}$  calculated from only the attractive branch of the BB-potential for Kr-Kr has been presented. The calculated  $Q_{LL}$  in this example turns out to be proportional to  $g^{-0.352}$ , corresponding with  $s = 6.7$  in the potential  $V(r) = -C_s/r^s$ . The BB-potential can indeed be reproduced within 1% by such a potential in the region  $1.3 < r/r_m < 2.2$ . Because this behaviour of  $Q_{LL}$  is representative for all rare gas potentials, we have used the value  $s = 6.7$  in our calculations of the angular resolution correction.

### c. The Interpretation of Glory Undulations

For the earlier reported preliminary analysis of our Ar-Kr data [BRE 71] we used the method developed by Bernstein and O'Brien [BER 62b, BER 63, BER 65, BER 67]. In this method Eq. 1.21 is used, which gives the relation between the extremum number  $N$  and the maximum phase shift  $\eta_0$  at the velocity  $g_N$  where  $Q_{GL}$  shows an extremum:

$$(N - 3/8) \pi = \eta_0 . \quad 3.33$$

By using the expansion

$$\eta_0 = 2a_1 \epsilon r_m / (\hbar g) + 4a_2 \epsilon^2 r_m / (\hbar \mu g^3) + \dots , \quad 3.34$$

in which the coefficients,  $a_1, a_2 \dots$  depend only on the shape of the potential, the product  $a_1 \epsilon r_m$  can be determined from the initial slope of the curve which results when  $(N - 3/8)$  is plotted as a function of  $g_N^{-1}$ . For every potential model for which  $a_1$  is known, one finds the value of the product  $\epsilon r_m$ . In this thesis, however, we no longer apply this method for three reasons. The first is that only for simple two-parameter potentials are the constants  $a_1, a_2 \dots$  known. They are not known for the complicated potentials we test. Secondly we have some doubt about the general validity of Eq. 3.33. This equation was derived under the assumption that the phase shift curve can be approximated by a parabola in the neighbourhood of  $\eta_0$ . This assumption is justified for L.J.

(n, 6), Exp (n, 6) and Kihara ( $\alpha$ , 6) potentials, but certainly not for realistic noble gas potentials, as our numerical calculations reveal. To the same conclusion came Düren et al. [DUR 68] for alkali-noble gas potentials. Therefore the validity of Eq. 3.33 is, at the least, questionable. Our third reason originates from the difficulty to separate the glory contribution  $Q_{GL}$  from the total cross section  $Q = Q_{LL} + Q_{GL}$ . For this separation one needs to know  $Q_{LL}$ . When  $Q_{LL} \sim g^{-2/5}$  the separation is usually accomplished by plotting  $Q g^{2/5}$  versus  $g$ , since  $Q g^{2/5} = \text{const} + Q_{GL} g^{2/5}$ . Generally  $g^{2/5}$  varies slowly enough with  $g$ , so that the extrema in  $Q g^{2/5}$  appear at the extrema velocities  $g_N$  of  $Q_{GL}$ . If, however, as in the case of rare gas scattering,  $Q_{LL}$  is not proportional to  $g^{-2/5}$  ( $s \neq 6$ ) and moreover the influence of the factor  $g^{2/5}$  is important for the position of the extrema velocities it is hardly possible to devise a unique method to determine the  $g_N$ . We therefore abandoned this aim and continued the analysis on the basis of the extrema velocities in  $Q g^{2/5}$  which we denoted by  $g_{GL}$ . The difference between  $g_N$  and  $g_{GL}$  can indeed be significant. This is clear from calculations we performed for the BFW-potential for Ar-Ar which yield the following result:

$$N = 1 : g_N = 2855, g_{GL} = 2970 ;$$

$$N = 1.5 : g_N = 1561, g_{GL} = 1540 ;$$

$$N = 2 : g_N = 1058, g_{GL} = 1070 .$$

For this third reason we disagree with the method used by Fitts and Low in analysing our data on Ar-Ar [FIT 73]. They first calculated the expansion coefficients of Eq. 3.34 for a number of potentials and next determined the product  $\epsilon r_m$  using our values of  $g_{GL}$ . Due to the difference between  $g_{GL}$  and the proper extrema velocity  $g_N$ , they arrived at values for the product  $\epsilon r_m$  which are too large. The agreement of the BFW-potential with our data is better than they assert, as is clear from Table 4.1.

We also point out that in the direct inversion method of Buck [BUC 71a] in which Eq. 3.33 is used to determine the maximum phase shift  $\eta_0$  at the velocity  $g_N$ , an error occurs by using the extrema velocities  $g_{GL}$  instead of the proper  $g_N$ .



## CHAPTER IV

## RESULTS AND DISCUSSION

## 1. INTRODUCTION

The development of rare gas potentials during the last three decades is to a large extent determined by the increasing availability of computer facilities. Before 1950, the precomputer era, mathematical methods were used to derive expressions in closed form for the macroscopic properties from an assumed interaction. These calculations were therefore limited to the simplest potential models, such as the hard sphere model or a potential of the type  $V(r) \sim r^{-5}$ .

In the subsequent period numerical calculations with electronic computers became more and more common. Up to about 1965 calculations were confined to simple but more realistic potentials, such as the Lennard-Jones (12,6) and the Exponent, 6 potential. In this context we mention the work of Hirschfelder et al. [HIR 67]. As an example we have plotted in Fig. 4.1 the L.J. (12, 6) potential Hirschfelder proposes for the Ar-Ar interaction. A historical review of this period is given by Brush [BRU 70].

As pointed out in Chapter I, even for these rather realistic potentials one cannot find a unique set of parameters which yields good agreement with a large number of macroscopic properties. Therefore it appeared necessary to introduce a more flexible potential model and fit this simultaneously to all existing experimental data on the various properties. As computer facilities increased, such an approach became feasible. The most rigorous procedure is to work with a numerically tabulated potential, assuming a priori very little about its functional form. This method was adopted by Alder and coworkers [DYM 69], who determined in this way a potential for Ar-Ar from the macroscopic properties of the dilute gas. The fact that this potential is quite inadequate in describing the differential cross section and spectroscopic data, indicates that in determining a potential a large body of experimental data must be invoked.

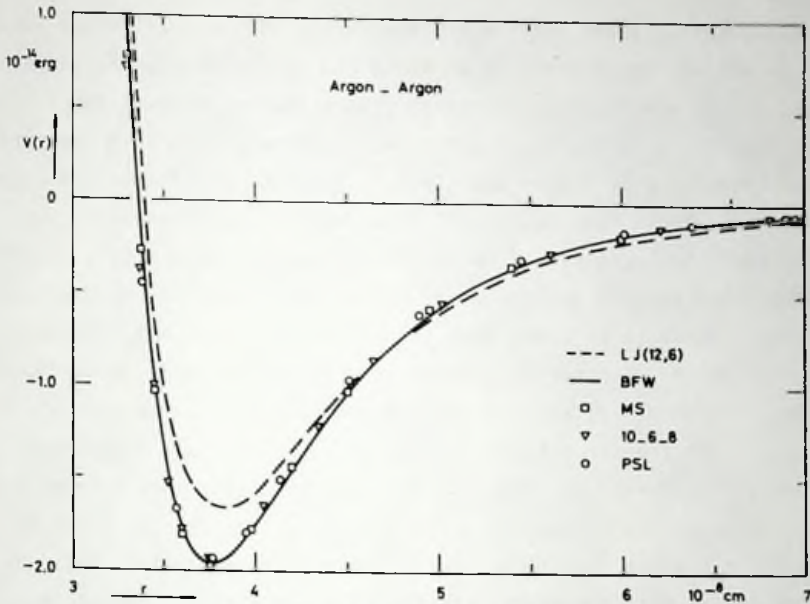


Fig. 4.1 Potentials for Ar-Ar.

Barker and coworkers have chosen an approach in which potential models are assumed with many, eight or more, adjustable parameters. Based on the earlier work of Barker and Pompe [BAR 68] and of Bobetic and Barker [BOB 70], Barker, Fisher and Watts arrived at a potential for the Ar-Ar interaction which is consistent with a large number of solid, liquid and gaseous properties, as well as with differential cross section and spectroscopic data [BAR 71a]. This potential (the BFW-potential) differs significantly from the L.J. (12, 6) potential for argon (see Fig. 4.1) and seems to be a very good approximation to the "true" argon pair potential.

Apart from the BFW-potential we have also plotted in Fig. 4.1 three other argon potentials recently proposed. The four new potentials are defined in the Appendix where they are presented in reduced form

$$V^*(x) = V(r)/\epsilon \quad , \quad \text{with } x = r/r_m \quad 4.1$$

along with the numerical values of the parameters and constants. The PSL-potential was introduced by Parson, Siska and Lee [PAR 72] to describe

their differential cross section and the second virial coefficient data. The MS-potential was obtained by Maitland and Smith [MAI 71] by slightly changing the Barker-Pompe potential to give a better description of spectroscopic data on the Ar<sub>2</sub> Van der Waals molecule. The 10-6-8 potential was introduced by Hanley and Klein to describe the dilute gas properties of argon. These four potentials show only small differences considering that they originate from different sources, were fitted to different data and were determined starting from rather different algebraic expressions. Hence it is clear that at the present stage only very small corrections to the obtained Ar-potentials remain to be made, when fitting new data. Unfortunately, these small changes result in variations in the observables that are far outside experimental errors. This experience indicates that whenever new experimental data are taken into account requiring a change in the potential, the ability of the new potential to account for all other properties should again be investigated. This always requires a large computational effort. Fortunately the development of the BFW-potential shows that this approach is convergent.

One might hope that the computational work involved in removing these last remaining uncertainties in the Ar pair potential can be limited by choosing a potential model with a small number of parameters. The possibility of such a simplification is suggested by the success of the 10-6-8 potential, a member of the family of m-6-8 potentials of Klein and Hanley [KLE 70] which requires only three parameters.

For the other rare gas combinations the development of the pair potential is not yet as advanced as for Ar-Ar. We feel that the law of corresponding states provides a successful approach. The validity of this law for the rare gases has recently been most convincingly demonstrated by the work of Kestin and Wakeham [KES 72]. It implies that for all rare gas combinations (or at least for the symmetric pairs) the same reduced pair potential may be used. Moreover, within the group of alkali-rare gas systems the law of corresponding states is valid [DUR 68] and the same is true for the alkali-mercury systems as shown by Buck et al. [BUC 71b].

For a more precise determination of the rare gas potentials the information contained in the total cross section data described in this

Chapter, is shown to be indispensable. Although the present potentials are unsuitable in describing our data, we do not attempt to change the potentials to obtain a better fit, because it is beyond the scope of this thesis to investigate the influence of such changes upon the predictions for all the other properties. We will confine ourselves to evaluating a number of potentials which are available at present.

## 2. RESULTS

The values of  $Q_{\text{exp}}$  and  $Q_{\text{corr}}$  for the measured systems have been tabulated in the Appendix. We present our results graphically in plots of the quantity  $Q_{\text{corr}}(\bar{g})^{2/5}$  as a function of  $\bar{g}$ . In this common way of presenting total cross section data, the monotonic velocity dependence of  $Q_{\text{LL}}$  is approximately compensated so that the glory contribution appears as an undulation about a nearly horizontal line. The velocities  $g_m$  at which in such a graph the extrema appear, can in most cases be determined with a maximum uncertainty of 3.0%, including the possible error in the velocity determination. If necessary the extremum shift  $\Delta g$  (Chapter III, par. 3c) is added to the value of  $g_m$ , yielding finally the corrected extrema velocity  $g_{\text{GL}} = g_m + \Delta g$ .

During the last three years, a number of potentials have been developed for the noble gases, which have proven their reliability in the description of many different properties. In order to investigate whether a particular potential describes our data, numerical calculations of the total cross section have been performed. For our calculations we have chosen those potentials which seemed to us most promising. Some of them have been published while others were obtained by private communication. They are all defined in the Appendix.

The numerical calculations of the total cross sections were performed according to Eq. 1.12. The required phase shifts  $\eta_l$  were calculated in the WKB approximation according to Eq. 1.13 with an absolute accuracy of at least 0.005. The classical turning points were determined by Muellers iteration method, the integrations were performed by the method of 32-point Gaussian quadrature. When for large  $l$ -values  $\eta_l$  became smal-



ler than 0.15, the Jeffreys-Born phases (Eq. 1.15) were used until  $\eta_g < 0.005$ . The contribution from still larger  $l$ -values was neglected. Within these approximations the calculated cross sections  $Q$  are accurate to at least  $1^0/\infty$ . The values of  $Q$  have been tabulated in the Appendix.

From a graph of the quantity  $Qg^{2/5}$  as a function of the relative velocity  $g$  the extrema velocities  $g_{GL}$  are determined. By comparing with the experimentally obtained values of  $g_{GL}$ , conclusions are drawn about the applicability of the potential tested. We also compare the absolute values of the calculated cross sections with the data of Phips et al. [PHI 71, SWE 70] (see Chapter III par. 4a).

In the next sections the aforementioned analysis is discussed for all the systems we investigated.

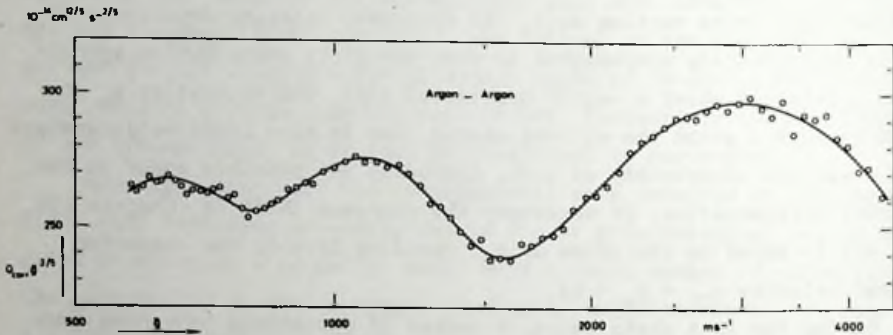


Fig. 4.2 Measured total cross sections  $Q_{\text{corr}}$  for Ar-Ar presented as  $Q_{\text{corr}} \bar{g}^{2/5}$  versus the average relative velocity  $\bar{g}$ .

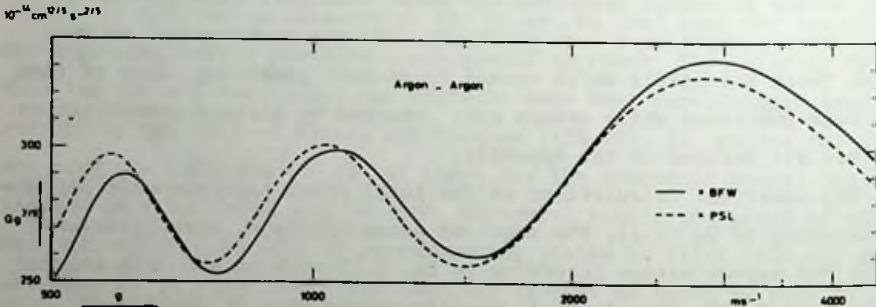


Fig. 4.3 Calculated total cross sections  $Q$  for Ar-Ar presented as  $Q g^{2/5}$  versus the relative velocity  $g$ , for the potentials indicated in the Figure.

## a. Ar-Ar

Early measurements of the velocity dependence of the total cross section for Ar-Ar scattering were performed by Baratz and Andres [BAR 70a]. The quality of their data, however, does not permit an accurate determination of the positions of the glory extrema. Our results are shown in Fig. 4.2 where  $Q_{\text{corr}} \bar{g}^{2/5}$  has been plotted as a function of the mean relative velocity  $\bar{g}$ . The observed extrema positions  $g_m$  and the corrected values  $g_{\text{GL}}$  have been tabulated in Table 4.1, together with values calculated for four recently proposed potentials depicted in Fig. 4.1.

Table 4.1

## RESULTS FOR Ar-Ar

N	Experimental		Calculated			
	$g_m$ (m s <sup>-1</sup> )	$g_{\text{GL}}$ (m s <sup>-1</sup> )	$g_{\text{GL}}$ (m s <sup>-1</sup> )			
			BFW	MS	10-6-8	PSL
1	3030 ± 90	3130 ± 120	2950	2910	2900	2880
1.5	1575 ± 45	1575 ± 45	1540	1550	1515	1510
2	1090 ± 30	1090 ± 30	1065	1065	1055	1030
2.5	802 ± 25	802 ± 25	775	770	768	755
3	642 ± 25	642 ± 25	608	605	600	585
$Q_{\text{LL}} g^{2/5}$ (10 <sup>-14</sup> cm <sup>12/5</sup> s <sup>-2/5</sup> )						
263 ± 5 [SWE 70]			BFW	MS	10-6-8	PSL
			268	275	269	277

Consider first the BFW-potential of Barker, Fisher and Watts [BAR 71a]. This potential is a refinement of two earlier potentials of Barker [BAR 69, BOB 70] and is consistent with high energy molecular beam scattering data, with some liquid and solid properties, with viscosity of the dilute gas, differential cross section data and with spectroscopic data on the  $\text{Ar}_2$  molecule. As can be seen from Table 4.1 the BFW-potential gives the best fit not only to our data on  $g_{\text{GL}}$ , but also to the absolute cross section data of SWE 70. Yet the predicted extrema, especially the first one, appear at velocities which are slightly too low. In the discussion we suggest a possible change of this potential to improve the agreement.

The MS-potential of Maitland and Smith [MAI 71] is a revised version of the Bobetic-Barker potential [BOB 70] and is very similar to the BFW-potential. It gives slightly worse agreement with our data and poor agreement with absolute cross section data of SWE 70.

The 10-6-8 is an unpublished potential of Klein and Hanley from the family of m-6-8 potentials [KLE 70, HAN 72b], which are consistent with the transport and equilibrium properties of the dilute gas. We investigated this potential because of its appealing simple reduced form and because of its ability to fit the differential cross section data of Parson et al. [PAR 72]. Also the 10-6-8 potential is very similar to the BFW-potential. It gives a good absolute value for the total cross section but its prediction of the extrema velocities is worse than that of the BFW- and the MS-potential.

The PSL-potential of Parson et al. [PAR 72], derived from differential cross section data and consistent with high energy molecular beam scattering data, viscosity data of the dilute gas and spectroscopic data, has been considered to be nearly equivalent to the BFW-potential in describing the interaction [HAN 72a]. It can be seen, however, to be in very poor agreement with our data, and the absolute value of the cross section is too large by 5%. In Fig. 4.3 the total cross sections calculated with the PSL- and the BFW-potential are compared.

For completeness we mention other recent references on the argon potential although no further use is made of this work: COL 69, BAR 70, BAR 71, CAL 72, DAV 72, DOC 72, FAU 72, FIS 72, JOH 72, SMI 72, KLE 73, FAR 73a.

b. Kr-Kr

The results of our measurements on Kr-Kr are depicted in Fig. 4.4. The increased scatter of the data points compared to the Ar-Ar results reflects the difficulty of accelerating the heavy and slow Kr atoms to obtain an intensive, fast beam. The relative glory amplitudes are smaller than for Ar-Ar due to the larger reduced mass of the Kr-Kr system. Calculated cross sections are shown in Fig. 4.5, while the potentials used can be found in Fig. 4.6. In Table 4.2 observed and calculated extrema velocities are listed.

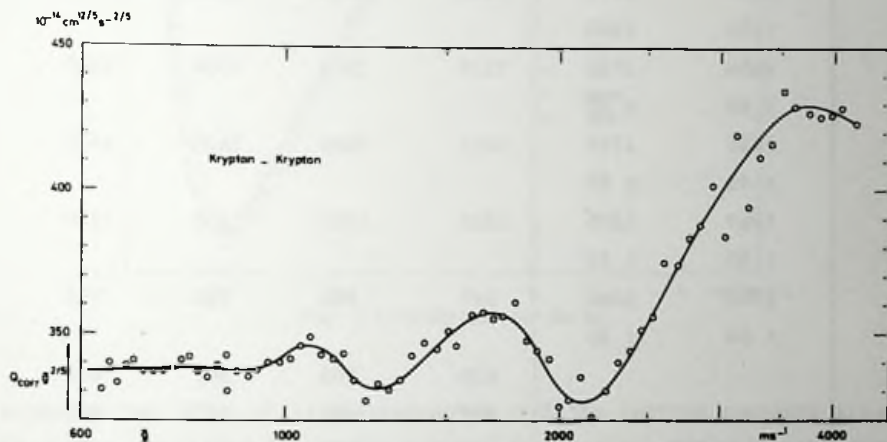


Fig. 4.4 Measured total cross sections  $Q_{\text{CORR}}$  for Kr-Kr presented as  $Q_{\text{CORR}} \bar{g}^{-2/5}$  versus the average relative velocity  $\bar{g}$ .

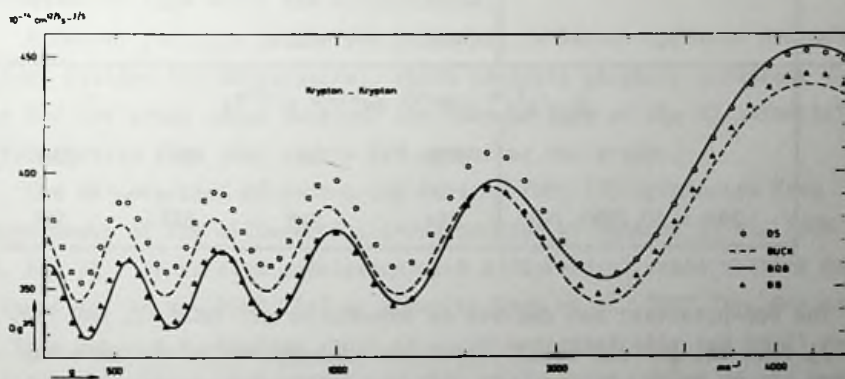


Fig. 4.5 Calculated total cross sections  $Q$  for Kr-Kr presented as  $Q \bar{g}^{-2/5}$  versus the relative velocity  $\bar{g}$ , for the potentials indicated in the Figure.



Table 4.2

## RESULTS FOR Kr-Kr

	Experimental		Calculated			
	$g_m$ (m s <sup>-1</sup> )	$g_{GL}$ (m s <sup>-1</sup> )	BOB	BB	DS	BUCK
1	3750 ±150	4875 ±300	4460	4450	4450	4440
1.5	2150 ± 60	2270 ± 90	2330	2320	2330	2320
2	1690 ± 45	1724 ± 60	1655	1640	1620	1610
2.5	1260 ± 35	1265 ± 35	1225	1217	1225	1220
3	1060 ± 30	1060 ± 30	997	985	985	975
3.5			820	808	807	803
4			698	690	687	683
4.5			600	590	590	585
5			524	517	513	510
5.5			458	453	453	448
6			406	402		
$Q_{LL} g^{2/5}$ (10 <sup>-14</sup> cm <sup>12/5</sup> s <sup>-2/5</sup> )			BOB	BB	DS	BUCK
340 ± 10 [SWE 70]			344	346	371	361

The BOB-potential was derived by Bobetic et al. [BOB 71, BAR 71b, BOB 72] from the gas and solid properties of krypton, in the same way as the BFW-potential for argon. Cavallini et al. [CAV 71a], however, showed that the BOB-potential inadequately describes their differential

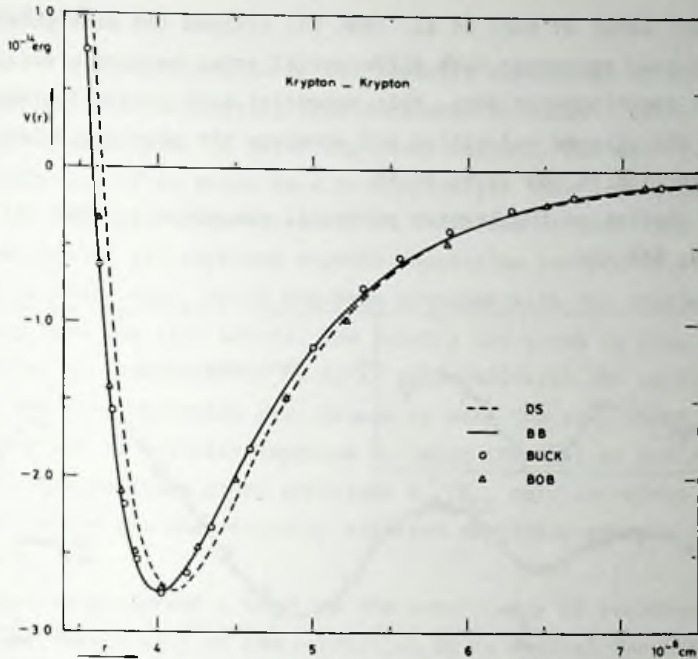


Fig. 4.6 Potentials for Kr-Kr.

cross section data, while discrepancies with the lattice constant also became apparent [KLE 73]. Table 4.2 reveals that the BOB-potential gives the correct absolute value of the total cross section while it predicts extrema velocities which are slightly low.

A recent revision of the BOB-potential by Barker (private communication) yielded the BB-potential, which predicts slightly different values for the total cross section. The reduced form of the BB-potential differs little from that of the BFW-potential for argon.

The DS-potential of Docken and Schafer [DOC 73] originates from measurements of the differential cross section by Schafer et al. [SCH 71a, SCH 73]. It is also consistent with differential cross section data of Cavallini et al. [CAV 71a] as shown by Buck et al. [BUC 73]. One can see from Table 4.2, however, that it gives systematically too small values for the extrema velocities and that the absolute value of the cross section is too large by 9%.

A recent study of Buck et al. [BUC 73] yielded the Buck-potential, which gives good agreement with differential cross sections, solid properties and spectroscopic data. This potential also yields too small values for the extrema velocities and moreover the absolute value of the cross section is too large by 6%.

Other studies on the krypton potential are given in: FAU 72, DAV 72, HAN 72b, FAR 73a.

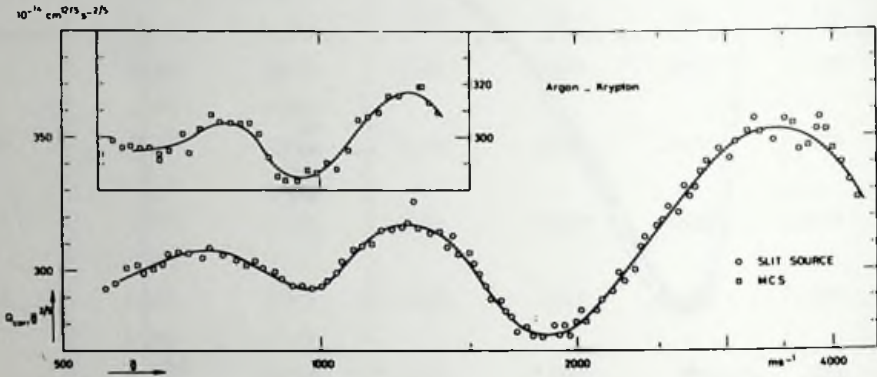


Fig. 4.7 Measured total cross sections  $Q_{\text{CORR}}$  for Ar-Kr presented as  $Q_{\text{CORR}} \bar{g}^{2/5}$  versus the average relative velocity  $\bar{g}$ . The data in the subfigure were obtained with the scattering gas effusing from the multi channel source, the other data in this Figure by using the slit source for the scattering gas.

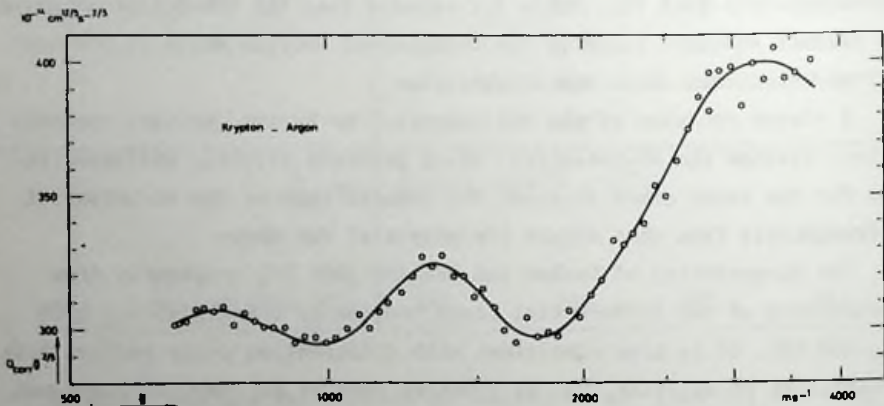


Fig. 4.8 Measured total cross sections  $Q_{\text{CORR}}$  for Kr-Ar presented as  $Q_{\text{CORR}} \bar{g}^{2/5}$  versus the average relative velocity  $\bar{g}$ . For these measurements the multi channel source was used for the scattering gas.

c. Ar-Kr and Kr-Ar

The first measurements of the velocity dependence of the total cross section for Ar-Kr scattering were performed by Winicur et al. [WIN 69], who were unsuccessful in resolving glory extrema. Our measurements on the scattering of an argon beam by krypton gas have been reported before [BRE 71], but only a summary analysis was given at that time. Meanwhile we have applied the improved angular resolution correction of Chapter III par. 3 to these data, which had been measured with the scattering gas effusing from the slit source. The results are given in Fig. 4.7, which also shows new measurements on Ar-Kr performed with the multi-channel source for the scattering gas. As can be seen the resolution of the glory extrema is scarcely improved by using the MCS: at the lowest velocities the relative glory amplitude  $A_{GL}/Q_{LL}$  only increases from 2.5% to 3.2%, while the theoretically expected amplitude amounts to 7% (see Fig. 4.9).

Next we performed a check on the consistency of our data, especially on the reliability of the correction  $\Delta g$  we applied for the shift of the glory extrema. For this purpose we measured the total cross section for scattering of a krypton beam by argon scattering gas (Fig. 4.8). Due to the less favourable kinematics the angular resolution correction for Kr-Ar scattering is much larger than for Ar-Kr scattering. Consequently a much larger extremum shift  $\Delta g$  occurs. After correction for the shift the extrema velocities  $g_{GL}$  for both runs agreed within the estimated uncertainties. This can be seen in Table 4.3. We still note that in this Table the numbers within parentheses are for Ar-Kr scattering with the MCS scattering gas source, and  $\langle g_{GL} \rangle$  is a weighted average of the two or three experimental values.

For the two potentials depicted in Fig. 4.10 total cross sections have been calculated. The results are shown in Fig. 4.9 and are compared with the measured data in Table 4.3.

The BAR-potential was determined by Barker et al. (private communication) using excess thermodynamic functions for liquid Ar-Kr mixtures. For its shape, the average of the reduced argon BFW-potential and the reduced krypton BB-potential was chosen. The values of  $\epsilon$  and  $r_m$  were de-



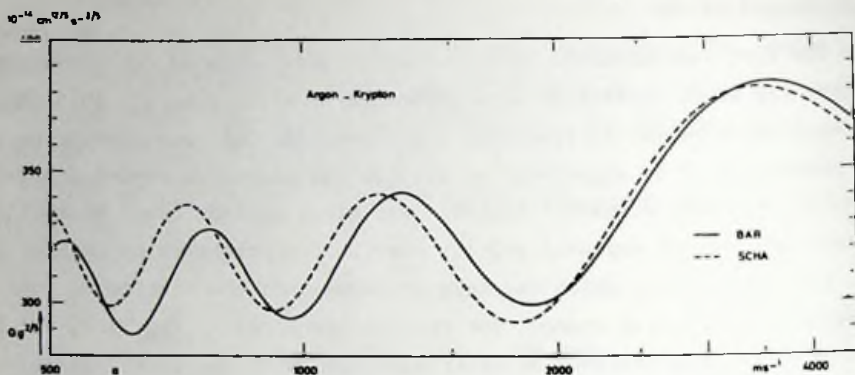


Fig. 4.9 Calculated total cross sections  $Q$  for Ar-Kr presented as  $Q g^{2/5}$  versus the relative velocity  $g$ , for the potentials indicated in the Figure.

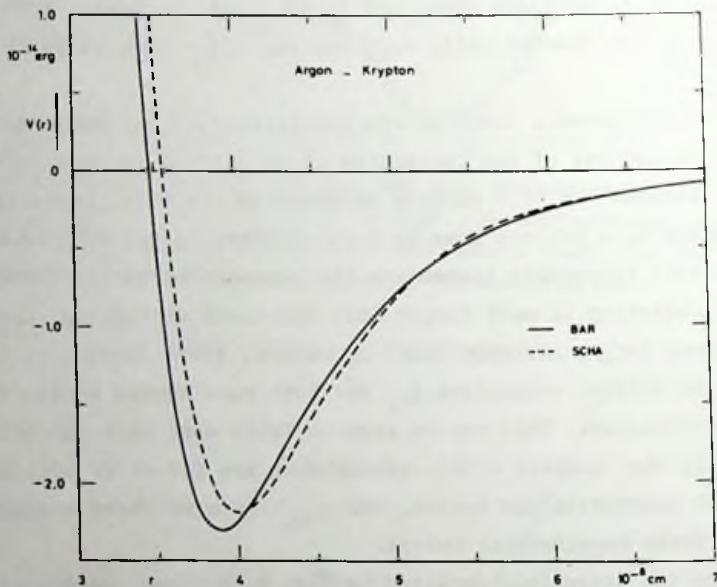


Fig. 4.10 Potentials for Ar-Kr.

terminated with the combination rules  $\epsilon_{12} = (\epsilon_{11} \cdot \epsilon_{22})^{1/2}$  and  $r_{m12} = \frac{1}{2}(r_{m11} + r_{m22})$ . This potential yields extrema velocities which are in excellent agreement with our data, except for the first extremum which is predicted at a slightly too low velocity. Also the absolute value of the cross section is in excellent agreement with the result of SWE 70.

The preliminary SCHA-potential which Schafer (private communication) derived from differential cross section data [PAR 70b] yields extrema velocities which are too low and an absolute value for the total cross section which is too large.

Table 4.3

## RESULTS FOR Ar-Kr AND Kr-Ar

N	Experimental					Calculated	
	Ar-Kr		Kr-Ar		$\langle g_{GL} \rangle$ ( $m s^{-1}$ )	$g_{GL}$ ( $m s^{-1}$ )	
	$g_m$ ( $m s^{-1}$ )	$g_{GL}$ ( $m s^{-1}$ )	$g_m$ ( $m s^{-1}$ )	$g_{GL}$ ( $m s^{-1}$ )			BAR
1	3470 $\pm 100$	3660 $\pm 140$	3170 $\pm 110$	3820 $\pm 200$	3740 $\pm 120$	3560	3450
1.5	1860 $\pm 55$	1878 $\pm 55$	1765 $\pm 50$	1825 $\pm 60$	1860 $\pm 40$	1870	1780
2	1280 (1275) $\pm 35$	1280 (1275) $\pm 35$	1330 $\pm 35$	1355 $\pm 40$	1305 $\pm 30$	1315	1235
2.5	965 (955) $\pm 30$	965 (955) $\pm 30$	980 $\pm 30$	980 $\pm 30$	967 $\pm 20$	967	923
3	740 (775) $\pm 25$	740 (775) $\pm 25$	750 $\pm 25$	750 $\pm 25$	755 $\pm 20$	772	726
3.5						623	590
4						522	
$Q_{LL} g^{2/5} (10^{-14} cm^{12/5} s^{-2/5})$						BAR	SCHA
299 $\pm$ 6 [SWE 70]						305	315

## d. Ar-Xe

The small spread of relative velocities as a result of the low velocities of the heavy Xe-atoms, made it possible for the Ar-Xe system to resolve no less than seven glory extrema. The results are shown in Fig. 4.11. The only potential available to us is from Schafer (private communication). It is derived from differential cross section data and is depicted in Fig. 4.13. The total cross sections calculated with this potential are shown in Fig. 4.12. Experiment and calculations are compared in Table 4.4. The predicted extrema velocities are too low and the calculated absolute value of the cross section too large.

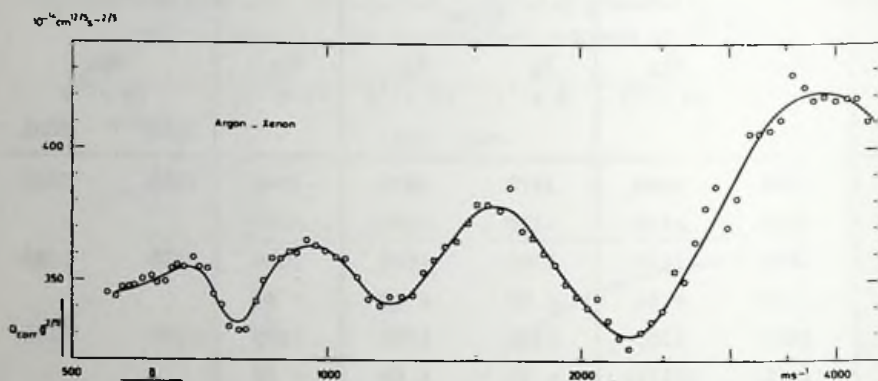


Fig. 4.11 Measured total cross sections  $Q_{\text{CORR}}$  for Ar-Xe presented as  $Q_{\text{CORR}} \bar{g}^{2/5}$  as a function of the average relative velocity  $\bar{g}$ .

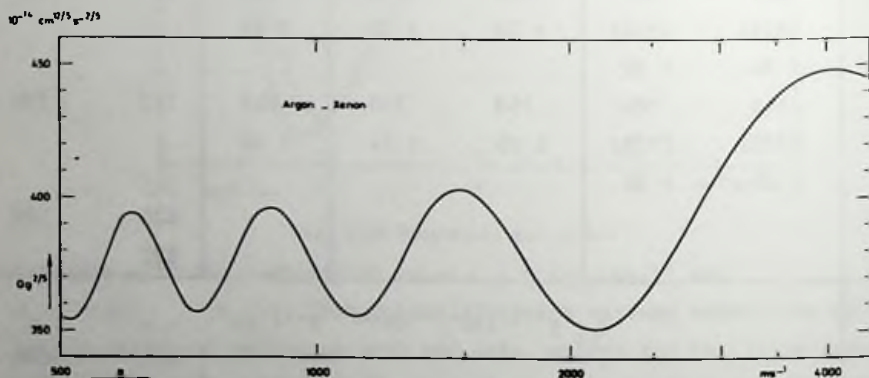


Fig. 4.12 Calculated total cross sections  $Q$  for Ar-Xe presented as  $Q \bar{g}^{2/5}$  versus the relative velocity  $\bar{g}$ , for the potential we obtained from Schafer.

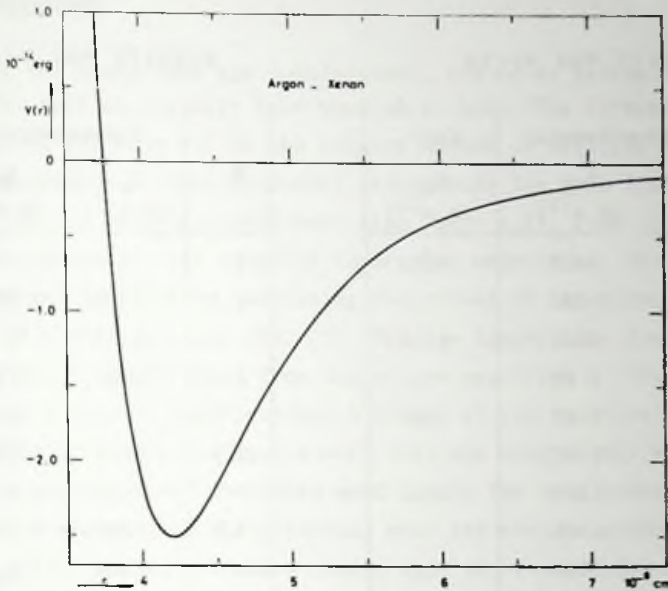


Fig. 4.13 The potential for Ar-Xe, which Schafer obtained from differential cross section data.

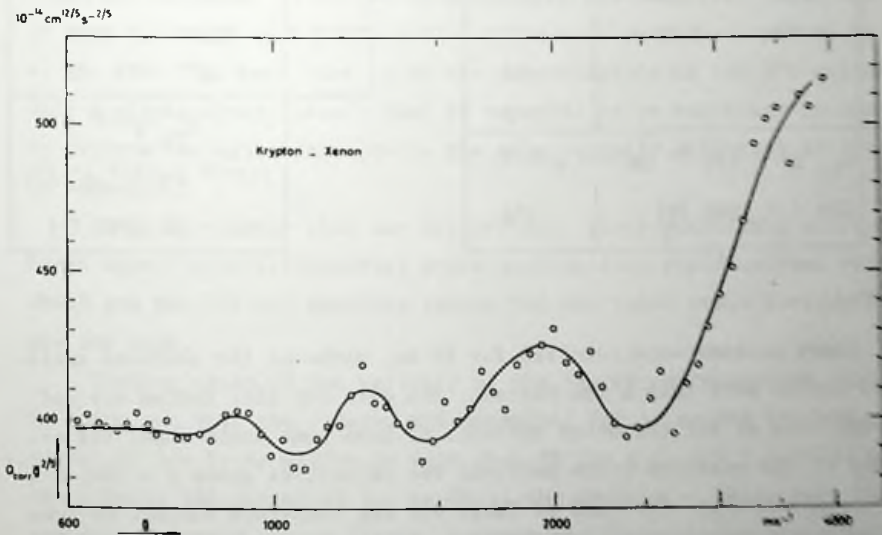


Fig. 4.14 Measured total cross sections  $Q_{\text{corr}}$  for Kr-Xe presented as  $Q_{\text{corr}} g^{-2/5}$  versus the average relative velocity  $\bar{g}$ .



Table 4.4

## RESULTS FOR Ar-Xe

N	Experimental		Calc.
	$g_m$ (m s <sup>-1</sup> )	$g_{GL}$ (m s <sup>-1</sup> )	$g_{GL}$ (m s <sup>-1</sup> )
1	3850 ±130	4160 ±180	4090
1.5	2280 ± 60	2315 ± 65	2130
2	1580 ± 40	1580 ± 40	1480
2.5	1190 ± 25	1190 ± 25	1110
3	960 ± 25	960 ± 25	880
3.5	785 ± 20	785 ± 20	723
4	690 ± 30	690 ± 30	607
4.5			514
5			442
$Q_{LL} g^{2/5} (10^{-14} \text{ cm}^{12/5} \text{ s}^{-2/5})$			
354 ± 7 [SWE 70]			374

Table 4.5

## RESULTS FOR Kr-Xe

N	Experimental	
	$g_m$ (m s <sup>-1</sup> )	$g_{GL}$ (m s <sup>-1</sup> )
1		
1.5	2440 ± ??	2550 ± ??
2	1900 ± ??	1965 ± ??
2.5	1475 ± 45	1505 ± 50
3.0	1260 ± 35	1275 ± 35
3.5	1065 ± 30	1065 ± 30
4	915 ± 30	915 ± 30
4.5	810 ± 40	810 ± 40
$Q_{LL} g^{2/5}$ ( $10^{-14} \text{ cm}^{12/5} \text{ s}^{-2/5}$ )		
397 ± 10 [SWE 70]		

## e. Kr-Xe

Glory extrema were resolved for Kr-Xe, although the observed amplitudes are no more than a few percent. The data for this system are not as reliable as for the other systems. We have some doubt about the accuracy of the measured cross sections for velocities above  $\bar{g} = 1660 \text{ m s}^{-1}$ . The results in Fig. 4.14 and in Table 4.5 are therefore subject to some reserve. No suitable potentials for this system are available so that no comparison can be made.

### 3. CONCLUSIONS

Of the heavy rare gas combinations, the Ar-Ar system is the one that has most extensively been studied to date. The interaction potential that gives the best fit to the largest number of measured properties is the BFW-potential. This potential also yields the best fit to the total cross section data presented here (see Table 4.1). Even so the predicted extrema velocities are slightly lower than experiment. The agreement may be improved by slightly increasing the volume of the potential, cf. the study of Green and Mason [GRE 72]. The low temperature deviation of the second virial coefficient from the values predicted by this potential indicate a similar modification. A change of the potential, however, should be introduced in such a way, that the consistency with all other data is not affected. Therefore most likely the only permissible change will be a widening of the potential near its minimum without changing  $\epsilon$  and  $r_m$ . (The effect of such a change upon the total cross section has been studied by Düren et al. [DUR 68] and by Buck and Pauly [BUC 68].)

Not only for Ar-Ar, but also for Kr-Kr and Ar-Kr the potentials proposed by Barker and coworkers yield the best agreement with the total cross section data. It may be true that the BOB-potential for Kr-Kr is in poor agreement with differential cross section data as proved by Buck et al. [BUC 73], but, just as in the determination of the BFW-potential, only a slight change is all that is expected to be necessary in order to improve the agreement. (Maybe the only slightly different BB-potential is adequate.)

It is noteworthy that for all systems, those potentials which are based mainly upon differential cross section data yield extrema velocities which are too low and absolute values for the total cross section which are too high.

Turning again to the validity of the law of corresponding states, we point out that the reduced BFW-potential for Ar-Ar and the reduced BB-potential for Kr-Kr differ no more than 4% for  $x (= r/r_m) > 0.74$ , while the reduced BAR-potential for Ar-Kr is the average of these two. These are not presented in one figure, because the three curves are graphically indistinguishable. This result is all the more striking since the law

of corresponding states was not a starting point in the determination of these potentials. It would be interesting to perform more extensive tests on the law of corresponding states, including the mixed interactions. The main source of information, apart from scattering data is to be found in the high quality diffusion measurements on the various rare gas combinations performed by Van Heyningen et al. [HEY 68] and by Hogervorst [HOG 71].

In summarizing we conclude that of the recently proposed rare gas potentials none is in full agreement with the total cross section data. The best fit is obtained with the BFW-potential for Ar-Ar, the BOB-potential for Kr-Kr and the BAR-potential for Ar-Kr. Only small changes should be necessary to improve the agreement.

## APPENDIX

Table A

THE ANGULAR RESOLUTION  
FUNCTION  $W(\rho)$  FOR THE  
CIRCULAR COLLIMATOR

$\rho$ (mm)	$W(\rho)$
0.00000	1.00000
0.01700	1.00000
0.03401	0.99999
0.05101	0.99859
0.06802	0.99255
0.08503	0.98001
0.10204	0.96001
0.11904	0.93212
0.13605	0.89672
0.15305	0.85418
0.17006	0.80644
0.18707	0.75604
0.20407	0.70463
0.22108	0.65200
0.23808	0.59918
0.25509	0.54677
0.27210	0.49507
0.28910	0.44432
0.30611	0.39472
0.32311	0.34649
0.34012	0.29985
0.35713	0.25503
0.37413	0.21231
0.39114	0.17206
0.40815	0.13457
0.42515	0.10060
0.44216	0.07087
0.45916	0.04655
0.47617	0.02793
0.49318	0.01477
0.51018	0.00646
0.52719	0.00196
0.54419	0.00025
0.56120	0.00000

Table B

THE ANGULAR RESOLUTION  
FUNCTION  $W(\rho)$  FOR THE  
RECTANGULAR COLLIMATOR

$\rho$ (mm)	$W(\rho)$
0.00000	1.00000
0.02089	0.99998
0.04178	0.99863
0.06268	0.99393
0.08357	0.98478
0.10447	0.97056
0.12536	0.95078
0.14626	0.92524
0.16715	0.89389
0.18805	0.85681
0.20894	0.81436
0.22983	0.76662
0.25073	0.71426
0.27162	0.65802
0.29251	0.59895
0.31341	0.53866
0.33430	0.47851
0.35520	0.41915
0.37609	0.36155
0.39698	0.30621
0.41788	0.25398
0.43877	0.20598
0.45967	0.16313
0.48056	0.12576
0.50145	0.09390
0.52235	0.06745
0.54324	0.04616
0.56414	0.02966
0.58503	0.01747
0.60592	0.00909
0.62682	0.00392
0.64771	0.00117
0.66861	0.00014
0.68950	0.00000



Table C

## REDUCED FORMS OF THE RARE GAS POTENTIALS

$V^*(x) = \epsilon^{-1}V(r)$ with $x = r/r_m$	Ref.
$V_1^*(x) = \exp [\alpha(1-x)] \sum_{i=0}^5 A_i (x-1)^i - \sum_{j=0}^2 c_{2j+6} / (\delta + x^{2j+6})$	BAR 71a
$V_2^*(x) = \{(6+2\gamma)/(m-6)\}x^{-m} - \{[m-\gamma(m-8)]/(m-6)\}x^{-6} - \gamma x^{-8}$	KLE 70
$V_3^*(x) = \exp \{-2\beta(x-1)\} - 2 \exp \{-\beta(x-1)\}$ $0 < x \leq 1$	DOC 73
$= \exp \{-2\beta'(x-1)\} - 2 \exp \{-\beta'(x-1)\}$ $1 \leq x \leq x_1$	
$= b_1 + (x-x_1) [b_2 + (x-x_2) \{b_3 + (x-x_1)b_4\}]$ $x_1 \leq x \leq x_2$	
$= -c_6 x^{-6} - c_8 x^{-8} - c_{10} x^{-10}$ $x_2 \leq x \leq \infty$	
$V_4^*(x) = \exp \{-2\beta(x-1)\} - 2 \exp \{-\beta(x-1)\}$ $0 < x \leq 1$	DOC 73
$= \exp \{-2\beta'(x-1)\} - 2 \exp \{-\beta'(x-1)\}$ $1 \leq x \leq x_1$	
$= a_1 + a_2(x-x_1) + a_3(x-x_1)^2 + a_4(x-x_1)^3$ $x_1 \leq x \leq x_2$	
$= -c_6 x^{-6} - c_8 x^{-8} - c_{10} x^{-10}$ $x_2 \leq x < \infty$	
$V_5^*(x) = V_1^*(x) + \alpha' \exp \{-50(x-1.33)^2\}$	MAI 71
$V_6^*(x) = \exp \{-2\beta(x-1)\} - 2 \exp \{-\beta(x-1)\}$ $0 < x \leq x_1$	BUC 73
$= \sum_{i=0}^3 a_i \{(x-x_1)/(x_2-x_1)\}^i$ $x_1 \leq x \leq x_2$	
$= -c_6 x^{-6} - c_8 x^{-8}$ $x_2 \leq x < \infty$	

Table D

## RARE GAS POTENTIALS

Name, (system), [ref.]	Reduced form	Form parameters		$\epsilon$	$r_m$
				( $10^{-14}$ erg)	( $10^{-8}$ cm)
BFW (Ar-Ar) [BAR 71a]	$V_1^*(x)$	$c_6 = 1.10727$ $c_8 = 0.16971$ $c_{10} = 0$ $\alpha = 12.5$ $\delta = 0.01$	$A_0 = 0.27783$ $A_1 = -4.50431$ $A_2 = -8.33122$ $A_3 = -25.2696$ $A_4 = -102.0195$ $A_5 = -113.25$	1.962	3.7612
10-6-8 (Ar-Ar) [PAR 72]	$V_2^*(x)$	$c_6 = 0.9611$ $\gamma = 4$	$m = 10$	1.933	3.744
MS (Ar-Ar) [MAI 71]	$V_5^*(x)$	$c_6 = 1.11976$ $c_8 = 0.17155$ $c_{10} = 0.01375$ $\alpha = 12.5$ $\delta = 0.01$ $\alpha' = 0.025$	$A_0 = 0.29214$ $A_1 = -4.41458$ $A_2 = -7.0182$ $A_3 = -31.9293$ $A_4 = -136.026$ $A_5 = -151.0$	1.968	3.75
PSL (Ar-Ar) [PAR 72]	$V_3^*(x)$	$c_6 = 1.180$ $c_8 = 0.6118$ $c_{10} = 0$ $x_1 = 1.12636$ $x_2 = 1.400$	$\beta = \beta' = 6.279$ $b_1 = -0.7$ $b_2 = -1.8337$ $b_3 = -4.5740$ $b_4 = 4.3667$	1.943	3.760
DS (Kr-Kr) [DOC 73]	$V_4^*(x)$	$c_6 = 0.9611$ $c_8 = 0.9327$ $c_{10} = 0$ $x_1 = 1.1050$ $x_2 = 1.6000$	$\beta = 6.0$ $\beta' = 6.6$ $a_1 = -0.7500$ $a_2 = 3.300$ $a_3 = -5.7712$ $a_4 = 3.7234$	2.74	4.11
BUCK (Kr-Kr) [BUC 73]	$V_6^*(x)$	$c_6 = 1.0598$ $c_8 = 0.7113$ $\beta = 6.3$ $x_1 = 1.1166$ $x_2 = 1.2407$	$a_0 = -0.7292$ $a_1 = 0.39017$ $a_2 = -0.1204$ $a_3 = -0.041911$	2.762	4.03

BOB (Kr-Kr) [BOB 72]	$V_1^*(x)$	$c_6 = 1.074658$ $A_0 = 0.24795$ $c_8 = 0.171450$ $A_1 = -4.45855$ $c_{10} = 0.014319$ $A_2 = -13.68889$ $\alpha = 13.5$ $A_3 = -57.82403$ $\delta = 0.01$ $A_4 = -242.09192$ $A_5 = -337.0$	2.7255	4.0152
BB (Kr-Kr) [priv.com.]	$V_1^*(x)$	$c_6 = 1.06787$ $A_0 = 0.24036$ $c_8 = 0.170621$ $A_1 = -4.75446$ $c_{10} = 0.014271$ $A_2 = -9.2$ $\alpha = 12.5$ $A_3 = -25.2696$ $\delta = 0.01$ $A_4 = -102.0195$ $A_5 = -113.25$	2.756	4.0107
BAR (Ar-Kr) [priv.com.]	$V_1^*(x)$	$c_6 = 1.08756$ $A_0 = 0.25909$ $c_8 = 0.17017$ $A_1 = -4.62939$ $c_{10} = 0.01394$ $A_2 = -8.7656$ $\alpha = 12.5$ $A_3 = -25.2696$ $\delta = 0.01$ $A_4 = -102.0195$ $A_5 = -113.25$	2.306	3.8859
SCHA (Ar-Kr) [priv.com.]	$V_3^*(x)$	$c_6 = 1.0075$ $\beta = \beta' = 6.3$ $c_8 = 0.5522$ $b_1 = -0.75$ $c_{10} = 0$ $b_2 = 1.996$ $x_1 = 1.110$ $b_3 = -3.908$ $x_2 = 1.400$ $b_4 = -0.6596$	2.188	4.00
(Ar-Xe) [priv.com.]	$V_3(x)$	$c_6 = 1.0474$ $\beta = \beta' = 6.6$ $c_8 = 0.962$ $b_1 = -0.75$ $c_{10} = 0$ $b_2 = 1.960$ $x_1 = 1.105$ $b_3 = -4.445$ $x_2 = 1.400$ $b_4 = 1.801$	2.508	4.20

Table E

## MEASURED TOTAL CROSS SECTIONS FOR Ar-Ar

$v_1$ (m s <sup>-1</sup> )	$Q_{\text{exp}}$ (10 <sup>-16</sup> cm <sup>2</sup> )	$\bar{g}$ (m s <sup>-1</sup> )	$Q_{\text{corr}}$ (10 <sup>-16</sup> cm <sup>2</sup> )	$Q_{\text{corr}} \bar{g}^{2/5}$ (10 <sup>-14</sup> cm <sup>12/5</sup> s <sup>-2/5</sup> )
521	348.9	583	329.0	265.2
530	343.5	591	324.6	263.0
540	343.1	600	325.0	265.0
552	344.2	611	327.0	268.5
565	338.0	623	322.1	266.5
573	336.2	630	320.9	266.8
586	335.3	642	320.9	268.8
600	329.5	655	316.2	267.0
611	324.2	665	311.8	264.8
621	318.1	674	306.4	261.7
634	317.2	686	306.2	263.4
650	312.8	701	302.8	262.7
662	309.7	712	300.4	262.3
675	308.8	724	300.2	263.9
688	307.0	736	299.1	264.6
707	298.7	754	291.7	260.6
720	297.4	766	291.0	261.6
738	288.3	783	282.7	256.4
751	282.5	796	277.4	253.2
768	282.3	812	277.9	255.7
787	280.1	830	276.4	256.6
805	279.1	847	276.0	258.3
820	278.0	861	275.4	259.5
843	278.5	883	276.8	263.4
867	274.8	906	274.8	264.2
888	276.0	926	275.7	267.4
887	273.4	925	273.1	265.7
907	271.8	944	272.1	265.9
936	272.9	972	274.1	271.0
965	270.0	1000	272.0	272.0
996	268.5	1030	271.4	274.7
1028	266.4	1061	270.1	276.6
1055	261.3	1087	265.6	274.6
1089	257.3	1120	262.2	274.4
1122	251.8	1152	257.4	272.4
1159	249.0	1188	255.2	273.5
1194	242.6	1222	249.3	270.2
1231	235.4	1258	242.4	265.8
1269	226.3	1296	234.5	259.8
1302	222.7	1328	230.3	258.0
1341	216.3	1366	224.2	254.1
1381	209.0	1405	217.1	248.8
1421	201.9	1445	210.2	243.5



1461	200.8	1484	209.7	245.6
1501	192.4	1523	201.0	238.0
1544	190.4	1566	199.6	238.8
1587	187.1	1608	196.7	237.9
1635	188.9	1656	199.6	244.2
1679	185.8	1699	196.9	243.4
1732	185.1	1751	197.0	246.5
1786	182.9	1805	195.5	247.6
1834	182.0	1852	195.3	250.0
1888	183.8	1906	198.4	256.9
1951	183.8	1968	199.7	261.8
2011	181.1	2028	197.6	262.2
2075	180.4	2091	198.0	266.0
2143	180.5	2159	201.3	271.5
2206	182.0	2221	203.0	278.9
2275	180.9	2290	203.0	282.8
2347	178.6	2361	201.7	284.6
2417	177.4	2431	201.8	288.0
2490	176.2	2503	202.0	291.5
2568	173.2	2581	200.0	292.3
2636	170.0	2649	197.2	291.2
2716	168.1	2728	196.7	294.5
2790	166.3	2802	196.0	296.5
2876	157.5	2887	192.6	294.4
2964	160.6	2975	192.2	297.3
3055	159.3	3066	192.6	299.5
3149	153.4	3159	186.3	295.3
3242	149.1	3252	182.3	292.3
3330	148.8	3340	183.9	298.0
3425	140.8	3435	174.1	285.2
3529	140.9	3538	176.6	293.0
3632	137.3	3641	173.6	291.1
3736	135.3	3745	172.8	293.1
3851	129.0	3860	165.3	283.7
3968	125.2	3976	161.6	280.8
4087	119.2	4095	154.3	271.3
4196	117.4	4204	153.5	272.7
4361	110.5	4368	145.2	261.9

---

Table F

## MEASURED TOTAL CROSS SECTIONS FOR Kr-Kr

$v_1$ ( $\text{m s}^{-1}$ )	$Q_{\text{exp}}$ ( $10^{-16} \text{ cm}^2$ )	$\bar{g}$ ( $\text{m s}^{-1}$ )	$Q_{\text{corr}}$ ( $10^{-16} \text{ cm}^2$ )	$Q_{\text{corr}} \bar{g}^{2/5}$ ( $10^{-14} \text{ cm}^{12/5} \text{ s}^{-2/5}$ )
607	377.6	632	398.3	331.5
620	382.7	645	406.0	340.7
634	371.5	658	395.0	334.1
649	372.3	673	398.1	339.7
663	369.6	686	396.8	341.4
679	361.4	701	389.4	338.0
697	355.7	719	385.1	337.6
715	350.4	736	381.3	337.4
734	346.3	755	378.8	338.5
751	344.8	771	379.2	341.9
768	341.0	788	376.9	342.8
786	331.7	805	367.8	337.5
807	325.5	826	362.6	336.0
826	320.1	845	358.4	335.1
846	310.4	864	348.5	328.8
870	312.4	888	354.2	337.8
895	305.8	912	348.6	336.0
918	302.6	935	347.6	338.4
945	299.1	961	346.2	340.8
970	294.4	986	343.0	340.9
997	289.9	1012	340.2	342.0
1026	288.1	1041	341.5	347.0
1049	287.0	1064	340.1	348.7
1080	276.7	1094	329.5	342.5
1115	270.7	1129	325.2	341.3
1144	267.1	1157	323.5	343.1
1176	256.2	1189	313.6	333.8
1213	246.5	1226	301.3	326.7
1252	244.5	1264	302.6	332.3
1291	238.3	1303	297.4	330.6
1326	235.5	1337	297.0	333.6
1366	235.2	1377	301.1	342.3
1408	232.4	1419	301.4	346.7
1456	225.6	1466	295.7	344.7
1498	225.8	1508	301.0	354.8
1530	217.8	1540	290.9	345.7
1592	216.2	1601	295.3	356.5
1638	211.7	1647	292.6	357.3
1681	206.4	1690	287.7	355.0
1721	203.0	1730	286.0	356.1
1777	199.8	1785	286.3	361.1
1832	189.5	1840	272.3	347.6
1883	183.9	1891	266.8	344.3

1941	178.1	1949	261.0	340.9
1989	168.3	1996	246.0	324.4
2037	165.9	2044	245.7	327.1
2102	164.5	2109	248.7	335.3
2166	155.4	2173	235.3	321.0
2241	154.0	2248	238.6	330.0
2311	153.3	2317	243.1	340.3
2385	150.3	2391	242.9	344.1
2455	148.7	2461	245.0	351.3
2523	146.7	2529	245.9	356.4
2597	148.1	2603	255.5	374.7
2688	144.6	2693	251.8	374.2
2767	146.9	2773	255.0	383.4
2849	141.4	2854	254.8	387.7
2938	139.1	2943	260.7	401.5
3030	131.7	3035	246.7	384.7
3119	136.6	3124	265.8	419.2
3213	127.8	3217	247.0	394.2
3310	128.1	3314	254.7	411.5
3407	126.0	3411	254.7	416.0
3513	126.7	3517	262.7	434.4
3619	122.5	3623	256.4	429.2
3750	118.6	3754	251.7	427.3
3856	115.5	3860	247.9	425.5
3968	130.9	3972	245.5	426.2
4071	111.3	4074	244.5	428.8
4225	107.0	4228	237.8	423.3

Table G

MEASURED TOTAL CROSS SECTIONS FOR Ar-Kr  
(SCATTERING GAS FROM SLIT SOURCE)

$v_1$ (m s <sup>-1</sup> )	$Q_{\text{exp}}$ (10 <sup>-16</sup> cm <sup>2</sup> )	$\bar{g}$ (m s <sup>-1</sup> )	$Q_{\text{corr}}$ (10 <sup>-16</sup> cm <sup>2</sup> )	$Q_{\text{corr}} \bar{g}^{2/5}$ (10 <sup>-14</sup> cm <sup>12/5</sup> s <sup>-2/5</sup> )
503	382.1	534	373.9	290.9
512	380.7	542	373.3	292.2
522	377.9	552	371.2	292.6
531	376.2	560	370.1	293.5
540	371.4	569	365.9	292.0
548	373.1	576	368.1	295.3
557	369.7	585	365.3	294.8
567	374.8	594	371.1	301.3
577	371.5	604	368.4	301.1
585	370.5	612	367.9	302.2
595	363.5	621	361.4	298.7
603	362.6	629	361.0	299.8

613	360.9	638	359.8	300.7
621	361.9	646	361.4	303.4
630	358.6	655	358.5	302.6
640	360.5	664	361.0	306.5
649	359.2	673	360.0	307.3
658	356.7	682	358.1	307.2
669	354.3	692	356.1	307.4
680	350.8	703	353.1	306.7
695	347.6	718	350.6	307.0
706	343.0	728	346.4	305.1
720	344.4	741	348.4	309.1
735	339.2	756	343.7	307.3
748	335.3	769	340.3	306.2
765	332.2	786	337.8	306.7
778	327.2	798	333.2	304.5
792	323.5	812	329.9	303.5
800	321.0	820	327.6	302.5
810	319.8	829	326.7	303.1
821	318.2	840	325.5	303.6
837	312.5	856	320.1	300.8
853	309.3	871	317.3	300.3
868	306.0	886	314.5	299.6
885	300.3	903	309.0	296.6
899	297.2	917	306.2	295.7
912	293.4	929	302.7	293.9
925	291.7	942	301.2	294.1
939	289.7	956	299.6	294.2
952	287.7	969	298.0	294.2
962	285.3	978	295.7	293.2
974	285.6	990	296.5	295.3
988	282.2	1003	293.3	293.7
1002	282.0	1018	293.6	295.7
1016	279.1	1031	290.9	294.4
1030	281.6	1045	293.5	298.7
1043	283.0	1058	296.2	302.9
1047	281.0	1062	294.2	301.3
1061	283.0	1076	296.8	305.7
1079	282.1	1094	296.5	307.5
1094	282.1	1108	297.1	309.6
1106	279.8	1120	295.0	308.7
1122	275.6	1136	290.8	306.1
1137	276.7	1151	292.7	309.6
1152	276.7	1166	293.3	311.8
1168	277.1	1182	294.4	314.7
1186	276.7	1199	294.6	316.8
1202	273.4	1215	291.5	315.1
1218	271.8	1231	290.2	315.3
1237	270.0	1250	288.9	315.8
1255	269.3	1268	288.7	317.5
1275	273.4	1287	294.3	325.6
1292	263.6	1304	283.6	315.4
1315	261.8	1327	282.3	316.1



1335	257.7	1346	278.4	313.5
1350	261.1	1362	282.9	320.1
1363	254.0	1375	275.1	312.4
1370	254.5	1382	275.9	314.0
1382	252.1	1393	273.5	312.3
1395	247.5	1406	268.6	307.9
1400	247.3	1411	268.5	308.2
1419	248.8	1430	271.0	312.7
1423	249.6	1434	272.1	314.4
1437	242.1	1448	263.7	305.8
1444	241.5	1445	263.2	305.8
1463	240.6	1474	262.8	307.0
1471	232.2	1482	253.1	296.2
1487	238.1	1498	260.7	306.4
1508	233.5	1519	255.9	302.4
1528	229.0	1538	251.2	298.4
1554	223.6	1564	245.5	293.7
1576	218.5	1586	240.1	288.8
1597	216.5	1607	238.3	288.1
1619	215.2	1629	237.4	288.5
1641	210.8	1651	232.7	284.4
1666	207.6	1676	229.6	282.2
1690	202.2	1699	223.7	276.5
1712	202.7	1721	225.0	279.6
1738	200.1	1747	222.6	278.2
1764	196.3	1773	218.6	274.9
1791	194.4	1800	217.1	274.6
1818	192.8	1827	215.8	274.6
1845	191.5	1854	215.0	275.2
1871	192.4	1880	216.9	279.1
1900	188.6	1908	212.9	275.7
1929	189.0	1937	214.3	279.2
1958	185.0	1966	210.0	275.3
1989	186.4	1997	212.8	280.6
2017	187.2	2026	214.7	284.8
2047	183.3	2054	210.4	280.6
2075	184.0	2083	212.2	284.6
2105	182.5	2113	211.2	284.8
2133	183.2	2149	213.0	288.7
2170	190.1	2177	223.6	305.2
2201	181.3	2208	212.6	291.9
2234	183.2	2241	216.3	298.7
2271	179.6	2278	212.6	295.5
2304	178.9	2311	212.7	297.3
2336	178.6	2343	213.4	299.9
2370	181.2	2377	218.3	308.7
2404	181.3	2411	219.7	312.4
2479	179.7	2485	220.1	316.8
2519	178.6	2525	220.0	318.7
2558	179.0	2564	222.2	323.7
2595	176.1	2601	219.2	321.2
2634	174.3	2640	218.0	321.5

2764	175.5	2679	223.5	331.5
2717	173.2	2723	219.4	327.6
2754	173.0	2759	220.6	331.1
2793	173.5	2799	223.1	336.7
2838	173.0	2844	224.3	340.7
2887	171.4	2893	223.6	342.0
2933	170.6	2938	224.3	345.2
2985	168.4	2990	222.8	345.2
3028	165.3	3033	219.3	341.8
3074	165.6	3079	221.9	348.0
3123	163.8	3128	220.8	348.5
3177	162.9	3182	221.6	352.0
3234	162.4	3238	223.1	356.9
3288	158.4	3293	218.2	351.5
3342	155.7	3347	215.6	349.5
3406	153.0	3411	213.3	348.5
3469	151.7	3473	213.6	351.5
3517	151.6	3522	215.3	356.3
3597	148.4	3601	212.7	355.1
3653	144.7	3658	207.8	349.0
3745	140.9	3749	204.2	346.4
3836	139.9	3840	205.8	352.5
3856	140.7	3860	208.2	357.3
3924	137.2	3928	203.9	352.4
4003	132.9	4007	197.9	344.9
4100	128.8	4104	193.1	339.6
4116	129.1	4120	194.3	342.3
4187	124.8	4191	187.8	333.2
4280	120.7	4284	182.5	326.6

Table H  
MEASURED TOTAL CROSS SECTIONS FOR Ar-Kr  
(SCATTERING GAS FROM MCS)

$v_1$ (m s <sup>-1</sup> )	$Q_{\text{exp}}$ (10 <sup>-16</sup> cm <sup>2</sup> )	$\bar{g}$ (m s <sup>-1</sup> )	$Q_{\text{corr}}$ (10 <sup>-16</sup> cm <sup>2</sup> )	$Q_{\text{corr}}^{1/2}/s$ (10 <sup>-14</sup> cm <sup>1/2</sup> /s s <sup>-2/3</sup> )
511	386.6	541	378.6	296.1
524	379.0	553	372.0	295.6
543	379.2	571	373.4	298.5
558	371.0	585	366.3	295.7
572	367.4	599	363.5	296.1
589	361.7	615	358.7	295.4
606	357.0	631	354.9	295.5
623	347.3	648	346.0	290.9
641	347.0	665	346.6	294.4
667	348.0	690	349.0	300.9
681	336.4	703	337.7	295.4

701	342.0	723	344.4	302.5
724	342.8	745	346.3	308.0
744	335.4	765	339.5	305.0
765	331.1	785	335.9	305.0
787	326.4	806	332.0	304.7
808	322.4	827	328.7	304.7
828	315.0	847	321.6	300.9
852	301.8	870	308.6	291.9
875	291.3	893	298.2	285.0
896	286.6	913	294.0	283.5
923	282.6	940	290.6	283.5
950	282.5	966	291.4	287.4
979	277.4	995	286.9	286.4
1001	278.0	1016	288.2	290.1
1031	271.9	1046	282.6	287.8
1065	273.8	1079	285.8	294.7
1096	280.4	1110	294.1	306.7
1127	277.3	1141	291.8	307.6
1161	274.3	1174	289.7	308.9
1194	275.7	1207	292.4	315.3
1231	271.6	1243	289.0	315.4
1301	266.5	1313	285.9	318.8
1306	266.0	1318	285.4	318.8
1333	258.6	1344	277.8	312.8
1367	252.4	1378	271.8	309.0

Table I

## MEASURED TOTAL CROSS SECTIONS FOR Kr-Ar

$v_1$ (m s <sup>-1</sup> )	$Q_{\text{exp}}$ (10 <sup>-16</sup> cm <sup>2</sup> )	$\bar{g}$ (m s <sup>-1</sup> )	$Q_{\text{corr}}$ (10 <sup>-16</sup> cm <sup>2</sup> )	$Q_{\text{corr}} \bar{g}^{2/5}$ (10 <sup>-14</sup> cm <sup>12/5</sup> s <sup>-2/5</sup> )
608	349.2	662	355.4	301.4
617	347.0	670	354.2	301.9
633	342.9	685	351.9	302.5
651	342.4	702	353.7	307.0
669	337.8	718	350.9	307.5
689	331.3	737	346.1	306.4
708	328.0	755	344.8	308.1
732	315.4	777	333.2	301.3
755	314.1	799	334.4	305.8
777	306.1	820	327.6	302.7
801	299.1	843	322.0	300.8
826	293.5	866	318.2	300.5
851	288.4	890	314.6	300.4
876	278.7	914	305.5	294.8
904	275.4	941	304.3	297.0

932	270.1	968	300.5	296.6
960	263.8	995	295.3	294.8
989	260.2	1023	293.7	296.4
1022	257.7	1055	293.7	300.1
1056	256.2	1088	295.2	305.4
1089	247.5	1120	286.8	300.2
1122	246.9	1152	289.4	306.3
1158	244.2	1187	289.3	309.8
1195	241.6	1223	289.4	313.8
1232	240.1	1259	291.2	319.4
1266	240.1	1293	295.0	327.0
1303	233.1	1329	288.5	323.3
1341	230.8	1366	289.2	327.7
1383	221.0	1407	278.4	319.2
1422	216.8	1446	275.7	319.6
1463	208.1	1486	265.9	311.6
1502	205.9	1524	266.2	315.1
1552	197.3	1574	257.0	308.2
1599	188.7	1620	246.8	299.4
1647	182.4	1667	240.4	295.1
1697	182.5	1717	245.2	304.4
1746	175.3	1765	236.8	297.3
1798	172.0	1817	235.3	298.8
1852	167.4	1870	231.5	297.4
1906	167.4	1924	236.0	306.7
1962	162.6	1979	231.7	304.5
2023	161.6	2040	235.1	312.7
2086	159.6	2102	236.4	318.3
2160	160.2	2176	244.1	333.2
2217	156.1	2232	240.5	331.6
2281	153.7	2296	240.8	335.8
2351	150.7	2365	240.2	339.0
2419	151.5	2433	247.7	353.6
2492	146.5	2505	242.3	349.9
2569	146.3	2582	248.2	362.8
2646	145.7	2659	253.3	374.5
2722	145.4	2734	258.6	386.7
2801	140.4	2813	252.1	381.4
2885	140.6	2897	259.2	396.6
2973	137.2	2984	256.9	397.9
3064	130.2	3075	244.6	383.4
3155	130.6	3165	251.6	399.0
3250	125.9	3260	245.0	393.1
3341	125.8	3351	250.0	405.5
3440	120.0	3450	239.7	393.4
3538	117.6	3547	238.2	395.4
3681	114.8	3690	237.6	400.6



Table J

## MEASURED TOTAL CROSS SECTIONS FOR Ar-Xe

$v_1$ (m s <sup>-1</sup> )	$Q_{\text{exp}}$ (10 <sup>-16</sup> cm <sup>2</sup> )	$\bar{g}$ (m s <sup>-1</sup> )	$Q_{\text{corr}}$ (10 <sup>-16</sup> cm <sup>2</sup> )	$Q_{\text{corr}} \bar{g}^{2/5}$ (10 <sup>-14</sup> cm <sup>12/5</sup> s <sup>-2/5</sup> )
528	443.8	550	438.4	345.2
542	436.7	563	432.2	343.7
553	437.5	574	443.8	347.5
564	433.1	585	430.0	347.0
572	431.9	592	429.2	348.2
586	429.9	606	428.0	350.4
600	426.7	619	425.6	351.5
611	420.4	630	419.9	349.1
625	416.8	644	416.9	349.6
637	418.8	655	419.6	354.4
648	417.6	666	419.0	356.2
661	412.8	679	414.7	355.2
676	413.0	693	416.3	359.6
688	405.4	705	408.4	355.1
706	399.9	722	403.6	354.5
714	387.1	730	390.7	344.6
732	376.8	748	380.8	339.1
751	364.8	766	369.1	331.9
768	358.9	783	363.7	329.9
786	355.7	801	361.0	330.4
808	363.4	822	369.8	342.1
827	367.8	841	375.2	350.2
848	371.8	862	380.3	358.4
867	368.0	880	377.0	358.4
889	367.1	902	376.9	361.8
908	362.7	921	373.1	360.9
933	362.6	945	374.0	365.7
959	356.0	971	367.8	363.7
983	349.9	997	362.2	361.5
1013	342.9	1024	355.7	359.2
1040	338.4	1051	351.9	359.0
1075	326.2	1086	339.8	351.2
1107	314.5	1117	328.1	343.1
1144	307.5	1154	321.6	340.6
1178	306.3	1188	321.4	344.3
1216	301.5	1225	317.3	344.2
1253	297.2	1262	313.8	344.5
1290	300.4	1299	318.6	353.8
1332	298.8	1341	318.2	357.9
1374	298.2	1382	319.0	363.2
1419	294.6	1427	316.5	364.9
1463	295.4	1471	319.0	372.3
1504	296.0	1512	321.3	379.1
1547	291.5	1554	317.5	378.8

1598	285.0	1605	311.8	376.8
1646	287.0	1653	316.1	386.5
1696	270.9	1703	298.5	369.3
1748	264.7	1754	292.8	366.6
1801	256.6	1807	284.8	360.9
1856	249.6	1862	278.0	356.6
1910	240.8	1916	268.9	348.8
1969	233.9	1975	262.3	344.3
2027	227.3	2032	255.8	339.7
2088	225.9	2093	255.9	343.9
2152	217.0	2157	246.6	335.4
2216	209.4	2221	238.6	328.4
2281	203.6	2286	233.0	324.3
2346	204.2	2351	235.7	331.8
2414	202.2	2419	235.1	334.7
2492	200.4	2496	235.0	338.9
2566	201.3	2570	242.5	353.8
2643	198.5	2647	237.4	350.5
2725	201.4	2729	244.3	365.1
2804	203.4	2808	250.2	378.2
2887	202.6	2891	252.3	385.8
2976	191.7	2980	239.1	370.0
3064	192.3	3067	243.3	381.0
3161	197.8	3164	256.2	406.0
3250	193.7	3253	253.1	405.8
3352	190.0	3355	251.3	407.7
3452	187.2	3455	250.6	411.6
3555	188.7	3558	257.8	428.5
3659	182.7	3662	251.7	423.0
3764	177.2	3767	245.7	417.7
3881	173.2	3884	243.8	419.5
4000	168.5	4003	239.9	417.7
4128	164.6	4130	237.5	418.8
4243	161.0	4245	235.0	419.2
4368	154.6	4370	227.2	410.0

Table K

## MEASURED TOTAL CROSS SECTIONS FOR Kr-Xe

$v_1$ (m s <sup>-1</sup> )	$Q_{\text{exp}}$ (10 <sup>-16</sup> cm <sup>2</sup> )	$\bar{g}$ (m s <sup>-1</sup> )	$Q_{\text{corr}}$ (10 <sup>-16</sup> cm <sup>2</sup> )	$Q_{\text{corr}} \bar{g}^{2/5}$ (10 <sup>-14</sup> cm <sup>12/5</sup> s <sup>-2/5</sup> )
596	452.7	616	484.4	399.0
611	448.9	630	482.7	401.3
629	438.6	647	473.7	398.2
642	432.2	660	468.4	396.8
660	424.4	678	462.2	395.7
678	420.2	695	460.3	398.1
696	417.9	713	460.6	402.3

715	407.3	731	450.8	397.9
732	398.8	748	443.0	394.5
750	397.4	766	444.3	399.4
772	385.0	787	432.4	393.0
793	379.6	808	428.9	393.9
817	373.5	831	424.9	394.7
842	364.9	856	417.7	392.6
874	363.5	887	421.1	401.5
900	357.8	913	417.6	402.7
927	350.6	939	412.3	402.2
955	338.7	967	400.2	395.0
981	327.5	993	388.7	387.6
1008	325.5	1019	390.0	393.1
1038	312.8	1049	376.3	383.7
1068	306.4	1079	371.5	383.0
1100	306.8	1110	376.9	393.2
1131	303.6	1141	377.0	397.5
1164	297.7	1174	373.0	397.8
1197	297.9	1207	378.6	408.2
1233	297.3	1242	383.5	418.4
1269	283.7	1278	367.3	405.2
1308	276.8	1317	361.9	404.0
1346	268.0	1354	353.0	398.6
1390	261.4	1398	348.4	398.4
1431	249.3	1439	333.3	385.6
1475	246.4	1483	335.3	392.6
1518	247.5	1525	342.7	405.8
1563	239.0	1570	333.4	399.4
1612	234.8	1619	332.6	403.4
1660	234.6	1667	339.2	416.2
1713	225.4	1720	329.3	409.0
1766	217.5	1772	320.7	403.3
1817	218.0	1823	328.9	418.3
1874	213.7	1880	327.8	422.0
1932	209.4	1938	326.4	425.3
1996	205.6	2002	326.7	431.3
2056	196.2	2061	313.4	418.7
2116	190.2	2121	307.2	415.1
2181	188.0	2186	309.8	423.5
2242	178.1	2247	293.9	411.4
2312	170.9	2317	284.2	397.8
2375	165.8	2380	278.6	394.1
2449	162.3	2453	277.2	397.0
2521	160.9	2525	280.9	407.0
2597	159.2	2601	283.8	416.1
2676	149.6	2680	266.5	395.4
2760	149.8	2764	274.1	411.7
2844	147.6	2848	275.3	418.4
2927	146.9	2931	288.0	430.8
3015	145.8	3019	284.0	441.9
3106	144.3	3109	286.8	451.5
3198	144.3	3201	293.4	467.3

3297	146.4	3300	306.1	493.6
3401	144.5	3404	307.6	502.1
3492	141.1	3495	303.4	500.6
3597	134.9	3600	291.5	486.7
3690	137.0	3693	302.6	510.3
3807	132.9	3810	296.5	506.3
3942	131.4	3945	298.4	516.7
4065	131.4	4067	303.8	532.5
4196	130.2	4198	305.7	542.7

Table L

## CALCULATED TOTAL CROSS SECTIONS FOR FOUR Ar-Ar POTENTIALS

g (m s <sup>-1</sup> )	Q (10 <sup>-16</sup> cm <sup>2</sup> )			
	PSL	BFW	MS	10-6-8
500	350.3	329.1	333.8	328.8
515	354.6	332.3	337.6	332.6
530	363.5	340.6	346.2	342.1
546	366.6	346.5	352.1	347.1
562	370.9	353.3	358.9	354.0
579	368.1	355.9	361.1	354.7
597	364.4	355.3	360.4	353.8
614	355.5	351.9	356.7	348.4
633	344.6	342.9	347.5	339.1
652	333.3	334.5	339.1	329.8
671	319.4	321.3	325.9	316.4
692	309.4	310.3	315.0	306.2
712	298.8	299.8	304.6	295.6
734	291.3	289.4	294.3	286.4
756	287.9	283.9	289.0	281.9
778	284.8	279.8	285.1	278.4
802	285.3	277.3	282.6	277.0
826	288.5	279.0	284.2	279.5
851	290.9	282.0	287.1	282.8
876	293.9	284.7	289.5	285.6
903	298.0	288.2	292.8	289.3
930	300.8	292.5	296.7	293.4
958	301.4	295.5	299.4	295.9
986	300.4	296.4	299.9	296.2
1016	298.5	295.6	298.7	294.8
1046	295.4	293.6	296.2	292.2
1078	290.5	290.4	292.7	288.2
1110	284.0	285.8	287.8	283.1
1143	276.4	279.9	281.6	276.8
1178	278.2	272.9	274.4	269.7



1213	259.9	265.3	266.6	262.1
1250	251.9	257.5	258.7	254.2
1287	244.2	249.9	250.9	246.8
1326	237.2	242.7	243.6	239.6
1365	231.1	236.1	236.9	235.1
1406	225.8	230.3	231.1	227.5
1449	221.5	225.5	226.1	222.7
1492	218.3	221.5	221.9	218.9
1537	216.1	218.3	218.7	216.5
1583	214.7	216.0	216.3	215.1
1630	214.0	214.7	215.1	214.4
1679	213.5	214.6	214.9	213.8
1730	213.9	215.1	215.2	214.1
1782	215.0	215.7	215.6	215.5
1835	216.5	216.5	216.3	216.6
1890	217.5	218.0	217.9	217.9
1947	218.9	219.8	219.4	220.0
2005	220.6	221.0	220.4	221.1
2066	221.6	222.6	222.1	223.0
2128	222.8	224.1	223.2	223.9
2191	223.6	224.8	224.1	225.3
2257	223.9	226.0	224.9	225.6
2325	224.3	226.0	225.1	226.4
2395	223.9	226.5	225.4	226.4
2467	223.2	225.9	224.8	225.7
2541	222.4	225.5	224.1	225.1
2617	220.7	224.3	223.1	224.2
2695	219.3	222.7	221.3	222.6
2776	217.2	221.2	219.7	220.6
2859	214.5	218.8	217.5	218.3
2945	211.8	216.2	214.7	215.6
3034	209.0	213.6	212.0	212.8
3125	205.9	210.6	209.1	209.7
3218	202.4	207.2	205.7	206.6
3315	198.7	203.6	202.1	203.0
3414	195.0	199.9	198.4	199.2
3517	191.1	196.1	194.5	195.2
3622	187.1	192.2	190.5	191.5
3731	183.1	188.1	186.6	187.4
3843	178.9	184.0	182.5	183.1
3958	174.7	179.8	178.4	179.3
4077	170.5	175.6	174.2	174.9
4199	166.6	171.5	170.0	170.8
4325	162.5	167.4	166.0	166.7
4455	158.3	163.3	162.0	162.6
4589	154.5	159.3	157.9	158.6
4726	150.5	155.1	153.8	154.5
4868	146.7	151.2	149.9	150.7

Table M

## CALCULATED TOTAL CROSS SECTIONS FOR FOUR Kr-Kr POTENTIALS

g (m s <sup>-1</sup> )	Q (10 <sup>-16</sup> cm <sup>2</sup> )			
	BOB	BB	DS	BUCK
400	518.4	521.5	557.2	543.0
412	512.2	508.4	541.5	525.2
424	494.5	487.2	518.2	502.3
437	472.2	466.4	497.0	483.3
450	454.5	453.8	485.4	474.5
463	447.5	452.6	485.9	476.7
477	451.3	460.1	494.6	485.4
491	460.8	469.7	504.3	493.7
506	468.7	474.2	507.9	495.0
521	468.8	469.7	502.0	486.7
537	459.4	456.3	487.1	470.7
553	443.4	438.7	468.4	452.2
570	426.2	422.6	451.6	436.9
587	413.1	412.7	441.4	428.8
605	406.9	410.4	439.4	428.5
623	408.1	413.9	444.3	433.2
641	414.8	420.5	452.2	439.4
661	422.2	426.4	457.6	443.9
680	424.7	427.5	456.4	443.0
701	421.3	421.2	449.5	434.6
722	412.8	410.2	437.3	421.9
744	399.1	396.8	421.4	407.8
766	385.3	382.4	407.4	393.5
789	373.4	372.5	396.1	384.3
813	365.6	365.9	390.3	378.8
837	363.1	365.5	389.5	379.1
862	364.9	367.7	392.7	381.8
888	369.0	373.0	397.2	386.9
915	374.5	377.1	402.0	390.1
942	377.6	379.6	403.4	391.6
970	378.1	379.1	401.7	389.6
1000	375.3	374.3	396.3	383.2
1030	368.6	366.4	387.1	373.9
1060	359.0	356.6	375.5	362.9
1092	348.1	345.9	363.2	351.3
1125	337.4	335.1	351.7	340.3
1159	328.0	326.0	341.9	330.8
1194	320.5	319.1	334.5	323.9
1229	315.8	315.0	330.1	319.9
1266	313.6	313.5	328.3	318.4
1304	313.8	314.4	328.8	319.1
1343	316.0	316.6	331.0	321.1
1384	319.3	319.6	334.0	323.7
1425	322.8	322.6	337.3	326.3
1468	325.5	325.2	339.8	328.6

1512	327.5	326.7	340.7	329.1
1557	328.2	326.4	340.1	328.2
1604	326.7	324.5	338.0	325.8
1652	324.1	321.2	333.5	321.1
1702	319.2	315.9	328.0	315.5
1753	313.6	309.5	320.8	308.5
1806	306.7	302.1	312.6	300.4
1860	298.9	294.1	304.2	292.4
1916	291.1	286.2	295.2	283.9
1973	283.4	278.2	286.4	275.5
2032	275.9	270.6	278.3	267.8
2093	269.1	263.8	270.8	260.8
2156	263.1	257.8	264.5	254.9
2221	258.1	253.0	259.0	250.0
2287	254.1	249.0	254.8	246.1
2356	251.0	246.0	351.5	243.2
2427	249.1	244.2	249.4	241.1
2500	248.2	243.1	248.3	240.4
2575	247.8	242.9	247.7	240.1
2652	248.4	243.4	248.3	240.6
2731	249.2	244.4	249.0	241.5
2813	250.5	345.6	250.5	243.0
2898	252.2	247.2	251.9	244.5
2985	254.1	248.7	253.7	246.0
3074	255.7	250.3	255.4	247.6
3167	257.3	251.8	256.9	249.1
3262	258.7	253.1	258.2	250.4
3359	259.9	253.9	259.3	251.4
3460	260.7	254.7	259.9	252.1
3564	261.0	254.9	260.3	252.3
3671	261.0	254.7	260.1	252.0
3781	260.5	254.1	259.6	251.5
3895	259.5	253.2	258.7	250.6
4011	258.3	251.6	257.3	248.9
4132	256.3	249.6	255.3	247.3
4256	254.0	247.3	253.0	245.1
4383	251.3	244.7	250.4	242.3
4515	248.5	241.9	247.4	239.4
4650	245.1	238.6	244.0	236.3
4790	241.4	235.0	240.4	232.6
4934	237.6	231.1	236.7	228.8
5082		227.1		224.9
5234		223.1		220.7
5391		218.7		216.5

Table N

## CALCULATED TOTAL CROSS SECTIONS FOR TWO Ar-Kr POTENTIALS

g (m s <sup>-1</sup> )	Q (10 <sup>-16</sup> cm <sup>2</sup> )		g (m s <sup>-1</sup> )	Q (10 <sup>-16</sup> cm <sup>2</sup> )	
	BAR	SCHA		BAR	SCHA
500	419.8	443.0	1679	249.6	240.0
515	420.6	430.3	1730	243.8	235.6
530	415.3	414.1	1782	238.8	232.2
546	403.9	397.3	1835	234.9	229.9
562	389.3	382.8	1890	232.0	228.4
579	373.8	372.5	1947	230.0	227.9
597	360.1	367.5	2005	228.9	228.1
614	350.6	367.5	2066	228.5	228.9
633	346.1	371.3	2128	228.8	230.2
652	346.5	376.9	2191	229.7	231.9
671	350.5	382.3	2257	230.9	233.6
692	356.4	385.5	2325	232.3	235.4
712	361.9	385.4	2395	233.9	237.2
734	365.4	381.4	2467	235.4	238.8
756	365.7	373.7	2541	236.8	240.2
778	362.2	363.1	2617	238.1	241.2
802	355.4	350.8	2695	239.1	242.0
826	345.8	338.3	2776	239.8	242.3
851	334.8	326.6	2859	240.1	242.2
876	323.6	316.9	2945	240.1	241.7
903	313.4	309.8	3034	239.7	240.8
930	305.1	305.6	3125	238.8	239.5
958	299.3	304.1	3218	237.5	237.7
986	296.2	304.8	3315	235.8	235.5
1016	295.6	307.1	3414	233.8	233.1
1046	297.0	310.3	3517	231.3	230.2
1078	299.9	313.4	3622	228.6	227.1
1110	303.3	316.0	3731	225.6	223.8
1143	306.6	317.4	3843	222.3	220.1
1178	309.2	317.3	3958	218.7	216.3
1213	310.6	315.5	4077	214.9	212.4
1250	310.5	311.9	4199	211.0	208.2
1287	308.7	306.7	4325	206.9	204.0
1326	305.3	300.2	4456	202.7	199.7
1365	300.2	292.6	4589	198.4	195.3
1406	294.1	284.4	4727	194.1	191.0
1449	286.9	275.9	4869	189.7	186.6
1492	279.3	267.4	5015	185.3	
1537	271.4	259.4	5165	180.8	
1583	263.6	252.1	5320	176.4	
1630	256.3	245.6	5480	172.1	



Table O

## CALCULATED TOTAL CROSS SECTIONS FOR SCHAFFER'S Ar-Xe POTENTIAL

g (m s <sup>-1</sup> )	Q (10 <sup>-16</sup> cm <sup>2</sup> )	g (m s <sup>-1</sup> )	Q (10 <sup>-16</sup> cm <sup>2</sup> )	g (m s <sup>-1</sup> )	Q (10 <sup>-16</sup> cm <sup>2</sup> )
400	519.9	970	384.7	2356	254.1
412	532.3	1000	371.8	2427	254.4
424	542.9	1030	359.9	2500	255.3
437	545.9	1060	350.1	2575	256.6
450	538.6	1092	343.0	2652	258.1
463	522.1	1125	338.8	2731	259.8
477	500.8	1159	337.4	2813	261.4
491	480.3	1194	338.3	2898	263.1
506	465.7	1229	340.7	2985	266.5
521	459.7	1266	343.7	3074	265.5
537	462.0	1304	346.7	3167	266.2
553	469.4	1343	348.9	3262	266.6
570	377.8	1384	349.7	3359	266.5
587	482.8	1425	348.8	3460	266.0
605	481.7	1468	346.2	3564	265.0
623	473.7	1512	341.7	3671	263.6
641	460.0	1557	335.7	3781	261.7
661	443.3	1604	328.2	3895	259.5
680	427.1	1652	320.0	4011	256.9
701	414.2	1702	311.2	4132	253.9
722	406.2	1753	302.1	4265	250.6
744	403.8	1806	293.3	4383	246.9
766	405.9	1860	285.0	4515	243.0
789	410.7	1916	277.5	4650	239.0
813	415.8	1973	271.0	4790	234.7
837	419.3	2032	265.5	4934	230.3
862	419.5	2093	261.1	5082	225.7
888	415.6	2156	257.9	5234	221.1
915	408.0	2221	255.7	5391	216.3
942	397.3	2287	254.5		

## REFERENCES

- ABU 67 N. Abuaf, J.B. Anderson, R.P. Andres, J.B. Fenn, D.R. Miller, Proc. Rar. Gas Dyn. Conf. V (1967) 1317.
- AND 66a J.B. Anderson, R.P. Andres, J.B. Fenn, G. Maise, Proc. Rar. Gas Dyn. Conf. IV (1966) vol. II p. 106.
- AND 66b J.B. Anderson, J.B. Penn, Proc. Rar. Gas Dyn. Conf. IV (1966) vol. II p. 311.
- ANL 71 K.G. Anlauf, R.W. Bickes Jr., R.B. Bernstein, J.C.P. 54 (1971) 3647.
- BAR 68 J.A. Barker, A. Pompe, Austr. J. Chem. 21 (1968) 1683.
- BAR 70 J.A. Barker, M.L. Klein, M.V. Bobetic, Phys. Rev. B 2 (1970) 4176.
- BAR 70a B. Baratz, R.P. Andres, J.C.P. 52 (1970) 6145.
- BAR 71 J.A. Barker, M.L. Klein, Chem. Phys. Letters 11 (1971) 501.
- BAR 71a J.A. Barker, R.A. Fisher, R.O. Watts, Mol. Phys. 21 (1971) 657.
- BAR 71b J.A. Barker, M.V. Bobetic, M.L. Klein, Phys. Letters 34a (1971) 415.
- BAR 72 J.A. Barker, Chem. Phys. Letters 14 (1972) 242.
- BEC 56 E.W. Becker, W. Henkes, Z. Phys. 146 (1956) 320.
- BEC 66 D. Beck, H.J. Loesch, Z. Phys. 195 (1966) 444.
- BER 61 R.B. Bernstein, J.C.P. 34 (1961) 361.
- BER 62 K. Berkling, R. Helbing, K. Kramer, H. Pauly, Ch. Schlier, P. Toschek, Z. Phys. 166 (1962) 406.
- BER 62a R.B. Bernstein, J.C.P. 36 (1962) 1403.
- BER 62b R.B. Bernstein, J.C.P. 37 (1962) 1880.
- BER 63 R.B. Bernstein, J.C.P. 38 (1963) 2599.
- BER 63a R.B. Bernstein, K.H. Kramer, J.C.P. 38 (1963) 2507.
- BER 65 R.B. Bernstein, T.J.P. O'Brien, Disc. Far. Soc. 40 (1965) 35.
- BER 66 R.B. Bernstein, Adv. in Chem. Phys. X (1966) 75 (Molecular Beams) Editor J. Ross, Interscience Publishers, New York.
- BER 67 R.B. Bernstein, T.J.P. O'Brien, J.C.P. 46 (1967) 1208.
- BIE 66 K. Bier, O. Hagena, Proc. Rar. Gas Dyn. Conf. IV (1966) vol. II p. 260.
- BOB 70 M.V. Bobetic, J.A. Barker, Phys. Rev. B 2 (1970) 4169.
- BOB 71 M.V. Bobetic, Thesis, University of Waterloo (1971).
- BOB 72 M.V. Bobetic, J.A. Barker, M.L. Klein, Phys. Rev. B 5 (1972) 3185.
- BRE 71 J.W. Bredewout, N.J. Bosman, A.G. Visser, J. Korving, C.J.N. van den Meijdenberg, Chem. Phys. Letters 11 (1971) 127.
- BRE 71a J.W. Bredewout, N.J. Bosman, A.G. Visser, J. Korving, C.J.N. van den Meijdenberg, Entropie 42 (1971) 148.
- BRO 72 N.J. Brown, R.J. Munn, J.C.P. 57 (1972) 2216.
- BRU 70 S.G. Brush, Archive for Rational Mechanics and Analysis 39 (1970) 1.
- BUC 68 U. Buck, H. Pauly, Z. Phys. 208 (1968) 390.
- BUC 71 U. Buck, K.A. Köhler, H. Pauly, Z. Phys. 244 (1971) 180.
- BUC 71a U. Buck, J.C.P. 54 (1971) 1923.

- BUC 71b U. Buck, M. Kick, H. Pauly, Book of Abstracts VII ICPEAC, Amsterdam (1971) p. 543.
- BUC 73 U. Buck, M.G. Dondi, U. Valbusa, M.L. Klein, G. Scoles, to be published.
- BUR 70 J.J. Burton, Chem. Phys. Letters 5 (1970) 312.
- BUS 66 F. v. Busch, Z. Phys. 193 (1966) 412.
- BUS 67 F. v. Busch, H.J. Strunck, Ch. Schlier, Z. Phys. 199 (1967) 518.
- CAL 72 R.E. Caligaris, A.E. Rodriguez, J.C.P. 56 (1972) 4715.
- CAN 71 P. Cantini, M.G. Dondi, F. Torello, Z. Naturf. 26A (1971) 1634.
- CAV 70 M. Cavallini, G. Gallinaro, L. Meneghetti, G. Scoles, Chem. Phys. Letters 7 (1970) 303.
- CAV 71 M. Cavallini, L. Meneghetti, G. Scoles, M. Yealland, Rev. Sci. Instr. 42 (1971) 1759.
- CAV 71a M. Cavallini, M.G. Dondi, G. Scoles, U. Valbusa, Entropie 42 (1971) 136.
- CER 71 P.R. Certain, L.W. Bruch, Report WIS-TCI-460, University of Wisconsin, (1971). To be published in MTP Int. Review of Science.
- COL 69 S.O. Colgate, J.E. Jordan, I. Amdur, E.A. Mason, J.C.P. 51 (1969) 968.
- DAS 53 J.G. Dash, H.S. Sommers Jr., Rev. Sci. Instr. 24 (1953) 91
- DAV 72 B.W. Davis, J.C.P. 57 (1972) 5098.
- DEC 63 J. Deckers, J.B. Fenn, Rev. Sci. Instr. 34 I (1963) 96.
- DOC 73 K.K. Docken, T.P. Schafer, to be published in J. Mol. Spectr.
- DUR 63 R. Düren, H. Pauly, Z. Phys. 175 (1963) 227.
- DUR 64 R. Düren, H. Pauly, Z. Phys. 177 (1964) 146.
- DUR 68 R. Düren, G.P. Raabe, Ch. Schlier, Sitzungsberichte der Heidelberger Akademie der Wissenschaften 3 (1968) 55.
- DUS 61 S. Dushman, Scientific Foundations of Vacuum Technique, Second Edition, Editor: J.M. Lafferty, New York, London, John Wiley and Sons, Inc. (1961).
- DYM 69 J.H. Dymond, B.J. Alder, J.C.P. 57 (1969) 309.
- DYM 71 J.H. Dymond, J.C.P. 54 (1971) 3675.
- FAR 73 J.M. Farrar, Y.T. Lee, V.V. Goldman, M.L. Klein, Chem. Phys. Letters 19 (1973) 359.
- FAR 73a J.M. Farrar, T.P. Schafer, Y.T. Lee, to be published.
- FAU 72 F.M. Faubert, G.S. Springer, J.C.P. 57 (1972) 2333.
- FEL 70 R. Felten, Thesis, University of Göttingen (1970).
- FEN 63 J.B. Fenn, J. Deckers, Proc. Rar. Gas Dyn. Conf. II (1963) vol. I, p. 497.
- FIS 67 S.S. Fisher, Report no. 67-5 (1967) University of California, Department of Engineering.
- FIS 72 R.A. Fisher, R.O. Watts, Mol. Phys. 23 (1972) 1051.
- FIT 73 D.D. Fitts, M.L. Law, Disc. Far. Soc. 55 (1973) 327.
- FOR 59 K.W. Ford, J.A. Wheeler, Ann. Physics 7 (1959) 259.
- FRE 65 J.B. French AIAA Journal, (June 1965) 993.
- GRE 72 E.F. Greene, E.A. Mason, J.C.P. 57 (1972) 2065.
- GRE 73 E.F. Greene, E.A. Mason, to be published in J.C.P.
- HAN 72a J.M. Hanley, J.A. Barker, J.M. Parson, Y.T. Lee, M. Klein, Mol. Phys. 24 (1972) 11.
- HAN 72b J.M. Hanley, M. Klein, J. Phys. Chem. 76 (1972) 1743.
- HEL 64 R. Helbing, H. Pauly, Z. Phys. 179 (1964) 16.
- HEL 66 R. Helbing, Thesis, University of Bonn (1966).

- HEL 68 R. Helbing, W. Gaide, H. Pauly, Z. Phys. 208 (1968) 215.  
 HEY 68 R.J.J. van Heijningen, J.P. Harpe, J.J.M. Beenakker, Physica 38 (1968) 1.  
 HIR 67 J.O. Hirschfelder, C.F. Curtiss, R. Byron Bird, Molecular Theory of Gases and Liquids, John Wiley Sons, Inc. New York (1967).  
 HOG 71 W. Hogervorst, Physica 51 (1971) 59.  
 HOS 60 H.U. Hostettler, R.B. Bernstein, Rev. Sci. Instr. 31 (1960) 872.  
 HOW 61 W.M. Howard, Phys. Fluids 4 (1961) 521.  
 JOH 66 J.C. Johnson, A.T. Stair, Jr., J.L. Pritchard, J. Appl. Phys. 37 (1966) 1551.  
 JOH 72 C.H.J. Johnson, T.H. Spurling, J.C.P. 57 (1972) 1804.  
 KAL 72 F. Kalos, A.E. Grosser, Can. J. Chem. 50 (1972) 892.  
 KAN 51 A. Kantrowitz, J. Grey, Rev. Sci. Instr. 22 (1951) 328.  
 KES 72 J. Kestin, S.T. Ro, W. Wakeham, Physica 58 (1972) 165.  
 KLE 70 M. Klein, H.J.M. Hanley, J.C.P. 53 (1970) 4722.  
 KLE 73 M.L. Klein, T.R. Koehler, R.L. Gray, Phys. Rev. B 7 (1973) 1571.  
 KLI 64 R. Klingelhöfer, P. Lohse, Phys. Fluids 7 (1964) 379.  
 KNU 64 E.L. Knuth, Appl. Mech. vol. 17 no. 10 (1964) 751.  
 KON 65 D.D. Konowalow, S. Carra, Phys. Fluids 8 (1965) 1585.  
 KON 70 P. Kong, E.A. Mason, R.J. Munn, Am. J. Phys. 38 (1970) 294.  
 KON 72 G.P. Können, N.T.N. 38 (1972) 265.  
 LAN 59 L.D. Landau, E.M. Lifshitz, Quantum Mechanics (Pergamon Press Ltd., London 1959) p. 416.  
 LAN 66 R.W. Landorf, C.R. Mueller, J.C.P. 45 (1966) 240.  
 LAN 71 N.C. Lang, H.V. Lilienfeld, J.L. Kinsey, J.C.P. 55 (1971) 3114.  
 LEM 71 G.D. Lempert, S.J.B. Corrigan, J.F. Wilson, Chem. Phys. Letters 8 (1971) 67.  
 MAI 71 G.C. Maitland, E.B. Smith, Mol. Phys. 22 (1971) 861.  
 MAR 38 H. Margenau, J.C.P. 9 (1938) 896.  
 MAS 34 H.S.W. Massey, C.B.O. Mohr, Proc. Roy. Soc. A 144 (1934) 188.  
 MAS 64 E.A. Mason, J.T. Vanderslice, C.J.G. Raw, J.C.P. 40 (1964) 2153.  
 MAS 71 E.A. Mason, R.J. Munn, F.J. Smith, Endeavour XXX (1971) 91.  
 MIL 67 T.A. Milne, F.T. Greene, J.C.P. 47 (1967) 4095.  
 MUL 67 G. Müller, Diplomarbeit, Bonn (1967).  
 MUN 65 R.J. Munn, F.J. Smith, J.C.P. 43 (1965) 3998.  
 NEN 71 T. Nenner, Entropie 42 (1971) 142.  
 NEU 70 W. Neumann, H. Pauly, J.C.P. 52 (1970) 2548.  
 NEU 73 P.D. Neufeld, R.A. Aziz, J.C.P. 58 (1973) 1877.  
 OKE 71 J.G.R. Okel, J. van de Ree, J.C.P. 54 (1971) 4259.  
 OWE 48 P.L. Owen, C.K. Thornhill, Aeron. Research Council, U.K., R+M (1948) 2616.  
 PAR 61 H.M. Parker, A.R. Kuhlman, R. Zapata, Proc. Rar. Gas Dyn. Conf. I (1961) 69.  
 PAR 70a J.M. Parson, T.P. Schafer, F.P. Tully, P.E. Siska, Y.C. Wong, Y.T. Lee, J.C.P. 53 (1970) 2123.  
 PAR 70b J.M. Parson, T.P. Schafer, P.E. Siska, F.P. Tully, Y.C. Wong, Y.T. Lee, J.C.P. 53 (1970) 3755.  
 PAR 71 J.M. Parson, Y.T. Lee, Entropie 42 (1971) 146.  
 PAR 72 J.M. Parson, P.E. Siska, Y.T. Lee, J.C.P. 56 (1972) 1511.  
 PAU 61 H. Pauly, Fortsch. Phys. 9 (1961) 613.



- PAU 65 H. Pauly, J.P. Toennies, Adv. in atomic and Mol. Phys. vol. I (1965) p. 195.
- PEN 67 J. Penta, C.R. Mueller, W. Williams, R. Olson, P. Chakraborti, Phys. Letters 25A (1967) 658.
- PHI 71 J.A. Phipps, J.E. Scott Jr., J.L. Shinn, Book of Abstracts VII ICPEAC, Amsterdam (1971) 559.
- POL 68 J. Politiek, P.K. Rol, P.G. Ikelaar, Rev. Sci. Instr. 39 (1968) 1147.
- POL 70a J. Politiek, J.J.M. Schipper, J. Los, Physica 49 (1970) 165.
- POL 70b J. Politiek, Thesis, University of Amsterdam (1970).
- RAG 72 J.A.A. Ragas, Internal Report, Physics Department, University of Nijmegen (1972).
- RAM 63 N.F. Ramsey, Molecular Beams, Clarendon Press, Oxford.
- ROT 62 E.W. Rothe, L.L. Marino, R.H. Neynaber, P.K. Rol, S.M. Trujillo, Phys. Rev. 126 (1962) 598.
- ROT 63 E.W. Rothe, P.K. Rol, R.B. Bernstein, Phys. Rev. 130 (1963) 2333.
- ROT 65 E.W. Rothe, R.H. Neynaber, J.C.P. 43 (1965) 4177.
- SCH 71 B. Schramm, Ber. Bunsen Ges. Phys. Chemie 75 (1971) 588.
- SCH 71a T.P. Schafer, P.E. Siska, Y.T. Lee, Book of Abstracts VII ICPEAC, Amsterdam (1971) 546.
- SCH 73 T.P. Schafer, J.M. Farrar, Y.T. Lee, to be published.
- SCO 63 J.E. Scott, J.E. Drewy, Proc. Rar. Gas Dyn. Conf. II (1963) vol. I p. 516.
- SCO 65 G. Scoles, C.J.N. van den Meijdenberg, J.W. Bredewout, J.J.M. Beenakker, Physica 31 (1965) 233.
- SCO 67 J.E. Scott, J.A. Phipps, Proc. Rar. Gas Dyn. Conf. V (1967) 1337.
- SCO 68 G. Scoles, F. Torello, Meccanica (Italy) 3 (1968) 20.
- SEA 71 J. Searcy, K. Wendell, C.R. Mueller, S. Sheen, Chem. Phys. Letters 8 (1971) 123.
- SHA 53 A.H. Shapiro, Compressible Fluid Flow Vol. I, The Ronald Press Company - New York (1953).
- SIS 70 P.E. Siska, J.M. Parson, T.P. Schafer, F.P. Tully, Y.C. Wong, Y.T. Lee, Phys. Rev. Letters 25 (1970) 271.
- SIS 71 P.E. Siska, J.M. Parson, T.P. Schafer, Y.T. Lee, J.C.P. 55 (1971) 5762.
- SMI 65 F.J. Smith, E.A. Mason, J.T. Vanderslice, J.C.P. 42 (1965) 3257.
- SMI 72 V.H. Smith Jr., A.J. Thakkar, Chem. Phys. Letters 17 (1972) 274.
- STA 71 G. Starkschall, R.G. Gordon, J.C.P. 54 (1971) 663.
- SWE 70 R.L. Swedenburg, J.A. Phipps, J.E. Scott, Report AEEP-3442-102-70 U, University of Virginia (1970).
- TAN 70 Y. Tanaka, K. Yoshino, J.C.P. 53 (1970) 2012.
- TRU 62 S.M. Trujillo, P.K. Rol, E.W. Rothe, Rev. Sci. Instr. 33 (1962) 841.
- VAL 64 J.P. Vallau, J.M. Deckers, Can. J. Chem. 43 (1965) 6.
- WEI 61 R. Weiss, Rev. Sci. Instr. 32 (1961) 397.
- WIL 69 W. Williams, C.R. Mueller, P. McGuire, B. Smith, Phys. Rev. Letters 22 (1969) 121.
- WIN 69 D.H. Winicur, E.L. Knuth, W.E. Rodgers, Entropie 30 (1969) 154.
- ZUG 66 P. Zugenmaier, Z. Ang. Phys. 20 (1966) 184.

## SAMENVATTING

De bestudering van de paar-potentiaal van edelgasatomen heeft de laatste jaren van verschillende zijden hernieuwde aandacht gekregen. Door een toename van computerfaciliteiten werd het mogelijk om de vele gegevens betreffende de vaste stof, de vloeistof en het verdunde gas uitvoeriger en in onderlinge samenhang te analyseren. Verder kwamen spectroscopische waarnemingen van Van der Waals dimeren ter beschikking. Tenslotte maakten technische ontwikkelingen het mogelijk om verstrooiingsexperimenten met bundels van edelgasatomen uit te voeren. Metingen van differentiële elastische botsingsdoorsneden zijn intussen door verschillende experimentatoren verricht. In dit proefschrift worden de eerste nauwkeurige metingen van de snelheidsafhankelijkheid van de totale botsingsdoorsneden van combinaties van edelgassen beschreven. De verkregen meetresultaten bevatten informatie, die onmisbaar is voor een nauwkeurige bepaling van de edelgaspotentialen.

Wanneer een atoombundel een strooikamer doorloopt waarin zich gas bevindt kan uit de verzwakking van de bundel de totale botsingsdoorsnede bepaald worden. Bij het verstrooiingsproces treden interferentieverschijnselen op, ten gevolge waarvan de totale botsingsdoorsnede als functie van de snelheid ondulaties vertoont. Deze worden naar analogie van soortgelijke optische verschijnselen glorie-ondulaties genoemd. De glorie-ondulaties verschaffen waardevolle informatie betreffende de interactiepotentiaal. Een samenvatting van de theorie en een uiteenzetting van de meetmethode wordt gegeven in hoofdstuk I.

Hoofdstuk II bevat een beschrijving van de ontwikkelde apparatuur. Zeer veel aandacht moest worden besteed aan de constructie van de bron, met als uiteindelijk resultaat, dat intensieve op snelheid geselecteerde Ar en Kr bundels gemaakt konden worden met snelheden van 550 tot 4300 m s<sup>-1</sup>. Aan de strenge vacuumeisen kon worden voldaan door toepassing van speciaal ontworpen cryopompen, waarmee een partiële druk van Ar en Kr beneden  $2 \times 10^{-9}$  torr werd verkregen. Van vitaal belang in een verstrooiingsexperiment met edelgassen is de detector. Langdurig experimenteren

leverde tenslotte een ionisatiedetector op met een extreem hoge efficiëncy en een zeer gunstige signaal-ruis verhouding.

Met de ontwikkelde apparatuur was het mogelijk de totale botsingsdoorsnede van de systemen Ar-Ar, Ar-Kr, Kr-Ar, Kr-Kr, Ar-Xe en Kr-Xe te meten in het eerder genoemde snelheidsgebied. Voor ieder van deze systemen werden de posities van verscheidene glorie-extremen nauwkeurig bepaald. In hoofdstuk III wordt beschreven hoe uit de meetgegevens de uiteindelijke resultaten werden verkregen. Deze worden weergegeven in hoofdstuk IV, waar tevens wordt nagegaan in hoeverre recent voorgestelde potentialen in overeenstemming zijn met de meetresultaten. Voor Ar-Ar blijkt de Barker-Fisher-Watts-potentiaal, die reeds een uitstekende beschrijving geeft van een zeer groot aantal macroscopische en microscopische eigenschappen van argon, het beste met de gemeten glorie-ondulaties overeen te komen. Voor een volledige overeenstemming zal deze potentiaal echter toch nog iets gewijzigd moeten worden. Ook voor de andere gemeten systemen zijn nog geen potentialen voorhanden die de metingen optimaal beschrijven. Een gelijktijdige aanpassing van de potentialen aan alle beschikbare experimentele gegevens is derhalve nodig om tot een zo nauwkeurig mogelijke bepaling van de edelgaspotentialen te komen. Dit zal in de toekomst verwerkelijkt moeten worden door een hechte internationale samenwerking.

## CURRICULUM VITAE

Op verzoek van de faculteit der wiskunde en natuurwetenschappen volgt hier een kort overzicht van mijn studie.

In 1956 behaalde ik het diploma gymnasium  $\beta$  aan het Christelijk Lyceum Zandvliet te 's-Gravenhage en begon ik mijn studie aan de Rijksuniversiteit te Leiden. Na een onderbreking van twee jaar voor de vervulling van mijn militaire dienstplicht legde ik in februari 1964 het candidaatsexamen natuurkunde en wiskunde met bijvak scheikunde af. In de maand mei van dat jaar begon ik mijn werkzaamheden op het Kamerlingh Onnes Laboratorium in de werkgroep voor moleculfysica, die onder leiding staat van Prof. Dr. J.J.M. Beenakker. In juni 1967 legde ik het doctoraalexamen experimentele natuurkunde af.

Direct na het candidaatsexamen begon ik in 1964 onder leiding van Dr. C.J.N. van den Meijdenberg aan het ontwerpen en bouwen van moleculbundelapparatuur, bestemd voor het bestuderen van de invloed van een magneetveld op de verzwakking van een bundel twee-atomige moleculen bij verstrooiing aan argon gas. Bij de eerste metingen in 1968 bleek deze invloed zo klein te zijn, dat ondanks de grote gevoeligheid van de apparatuur geen effect aantoonbaar was. In oktober 1968 werd daarna een begin gemaakt met het in dit proefschrift beschreven onderzoek, waarvoor de laatste metingen in mei 1972 werden verricht.

In 1968 nam ik deel aan een drie-weekse zomerschool te Varenna, in 1969 bracht ik gedurende drie weken een werkbezoek aan laboratoria in Freiburg en Bonn. Op verschillende internationale congressen heb ik reeds voorlopige resultaten van mijn onderzoek gerapporteerd.

Van 1965 tot en met 1971 heb ik achtereenvolgens geassisteerd bij het natuurkundig practicum voor medische studenten en voor studenten met hoofdvak natuurkunde. Na mijn doctoraalexamen werd ik in 1967 aangesteld als doctoraalassistent en in 1968 als wetenschappelijk medewerker. Sinds oktober 1972 ben ik in dienst bij de afdeling Geofysica van de Rijksuniversiteit te Utrecht.



Aan de tot stand koming van dit proefschrift hebben velen een bijdrage geleverd.

Mijn dank gaat uit naar de heren Drs. A.U. Wilkens, Drs. A.W. van Barneveld, Drs. N.J. Bosman, Drs. A.G. Visser, B. Trietsch en L. Groeneweg, die mij in de afgelopen jaren bij de experimenten en bij het rekenwerk terzijde hebben gestaan. Met waardering vermeld ik verder de discussies met Dr. J. Korving en Dr. S.E. Johnson. Prof. Dr. G. Scoles ben ik erkentelijk voor zijn waardevolle suggesties.

Ook aan de technische staf van het Kamerlingh Onnes Laboratorium ben ik veel dank verschuldigd. Bij het ontwerp en de bouw van de bundelapparatuur stond aanvankelijk de heer E.S. Prins ons met zijn deskundigheid terzijde, terwijl later de heer J. Post de verschillende onderdelen ontwierp en vervaardigde. Een groot deel van de electronische apparatuur is te danken aan de inventiviteit van de heer H.A. Brunia. De heer C. le Pair stond dag en nacht klaar om ons de benodigde honderden liters vloeibare waterstoff te leveren.

Mejuffrouw A.M. Aschoff dank ik voor het typen van het manuscript. Het tekenwerk werd verricht door de heer J. Bij, terwijl de heer W.F. Tegelaar voor de foto's zorgde. Dr. B.C. Sanctuary ben ik erkentelijk voor het corrigeren van de Engelse tekst.

## STELLINGEN

### I

Het mechanisme dat Griffiths en Hawkins voorstellen voor de nucleofiele fotosubstitutie van 2-methoxy-anthrachinon is in strijd met hun experimentele resultaten.

J. Griffiths, C. Hawkins, J.C.S. Chem. Commun. (1973) 111.

### II

De tripelpuntsdrukken van neon, zuurstof en waterstof, en waarschijnlijk ook van krypton en stikstof, kunnen gerealiseerd worden met een relatieve nauwkeurigheid tussen  $1 \times 10^{-4}$  en  $1 \times 10^{-5}$  en zijn derhalve goed te gebruiken als secundaire standaarden voor drukmeting.

W.A. van Hook, Metrologia 7 (1971) 30.

### III

Het verlenen van vrijstelling van invoerrecht en omzetbelasting aan overheidsinstellingen bij de aankoop van wetenschappelijke apparatuur in het buitenland is een vestzak-broekzak financiering, die zo snel mogelijk afgeschaft dient te worden, aangezien ze niemand voordeel en velen ergernis en overbodig werk bezorgt.

### IV

Gezien de toepassing van verfijnde methoden van numerieke dataverwerking in de exploratieseismologie is het meer dan ooit noodzakelijk bijzondere aandacht te besteden aan de veldtechniek en zich te realiseren dat de benadering van de fysische werkelijkheid met theoretische modellen een grens stelt aan het oplossend vermogen.

### V

Teneinde de nauwkeurigheid te kunnen testen van de wisselwerkingspotentialen, die voor alkali-edelgas combinaties zijn bepaald uit metingen van de totale en de differentiële botsingsdoorsnede, is het gewenst dat voor deze systemen diffusiecoëfficiënten worden gemeten.

## VI

Het verdient aanbeveling de door Neufeld en Aziz voor enige argon-argon potentialen uitgevoerde berekeningen van botsingsintegralen uit te breiden met berekeningen voor de door Barker voorgestelde argon-krypton potentiaal en vervolgens deze potentialen te toetsen aan de gemeten diffusiecoëfficiënten.

R.J.J. van Heyningen, J.P. Harpe, J.J.M. Beenakker, *Physica* 38 (1968) 1.

W. Hogervorst, *Physica* 51 (1971) 59.

Dit proefschrift, pagina 91.

## VII

In de absolute metingen van de totale botsingsdoorsnede van Swedenburg e.a. zijn de glorie-ondulaties tot binnen de meetnauwkeurigheid gedempt, hetgeen blijkt uit een vergelijking van de resultaten voor de systemen argon-krypton en krypton-argon.

R.L. Swedenburg, J.A. Phipps, J.E. Scott, Report AEEP-3442-102-70 U, University of Virginia (1970).

Dit proefschrift, pagina 77 en 91.

## VIII

Het opmerkelijke verschil in de waargenomen mate van botsingspolarisatie in supersonische bundels van jodiummoleculen en van natriumdimeren kan voor een belangrijk deel eenvoudig worden verklaard.

## IX

De gebruikelijke hoogte van spiegels boven wastafels doet vermoeden dat bouwkundigen óf kleiner dan 1,70 m zijn óf hun haar nooit kammen.

Leiden, 12 september 1973

J.W. Bredewout